COMPUTATIONAL STUDY OF CO_2 CAPTURE AND GAS ADSORPTION ON SURFACES

by

Bo Zhang

Bachelor of Applied Chemistry, East China University of Science and Technology, 2004

Master in Industrial Catalysis, East China University of Science and Technology, 2007

Submitted to the Graduate Faculty of

Swanson School of Engineering in partial fulfillment

of the requirements for the degree of

Doctor of Philosophy

University of Pittsburgh

2012

UNIVERSITY OF PITTSBURGH

SWANSON SCHOOL OF ENGINEERING

This dissertation was presented

by

Bo Zhang

It was defended on

Octoter 26, 2012

and approved by

Kenneth D. Jordan, Ph.D., Distinguished Professor, Department of Chemistry

Robert M. Enick, Ph.D., Bayer Professor, Department of Chemical and Petroleum Engineering

Wei Shi, Ph.D., Adjunct Professor, Department of Chemical and Petroleum Engineering

Dissertation Director: J. Karl Johnson, Ph.D., W.K. Whiteford Professor, Department of Chemical and Petroleum Engineering

COMPUTATIONAL STUDY OF CO_2 CAPTURE AND GAS ADSORPTION ON SURFACES

Bo Zhang, PhD

University of Pittsburgh, 2012

The structural and thermodynamic properties of $MHCO_3$ (M = Li, Na, K) were investigated with density functional theory (DFT). The most probable crystal structure for $LiHCO_3$, which has not been observed experimentally, was predicted from first principles. The stability of $LiHCO_3$ has also been predicted as a function of temperature and the partial pressures of CO_2 and H_2O. The phase diagrams and possible CO_2 capture reactions as a function of temperature and the partial pressures of CO_2 and H_2O were calculated from total energies from DFT and free energies from lattice dynamics for the M-C-O-H systems.

Different exchange-correlation functionals (PW91, PBE, PBEsol, TPSS, and revTPSS) were used to compute van't Hoff plots, which describe the reaction equilibrium as a function of the partial pressures of CO_2 and H_2O as well as temperature, for TMO and $TM(OH)_2$, where TM = Mn, Ni, Zn, and Cd. The PBEsol functional gives better equilibrium properties due to a partial cancellation of errors in the enthalpies of formation. We have identified all CO_2 capture reactions that lie on the Gibbs free energy convex hull as a function of temperature and the partial pressures of CO_2 and H_2O for TMO and $TM(OH)_2$ systems.

We have constructed a reaction pathway for tetrabutylphosphonium glycinate ($[P(C_4)_4][Gly]$) reacting with CO_2. The reaction has two barriers, as computed from nudged elastic band calculations. A ReaxFF force field was developed based on the reaction pathway and other relevant bond stretch, bond angle, and torsion angle energies as well as the equation of

state of $[P(C_4)_4][Gly]$. The force field has been validated and used for large-scale molecular dynamics simulations to study the thermophysical properties of the $[P(C_4)_4][Gly]/CO_2$ system.

Weakly bound molecular O_2 on the $TiO_2(110)$ surface has been studied using DFT with van der Waals (vdW) corrections. The potential energy surface of O_2 on $TiO_2(110)$ was constructed and the adsorption energy was found to be dominated by vdW contributions in most situations. The calculated vibrational frequency of the adsorbed O_2 molecule was found to be close to recent experimental IR measurements. The calculated IR intensities were found to be in qualitative agreement with experiments. Our calculations show that the appearance of IR modes for O_2 adsorbed on $TiO_2(110)$ is due to charge transfer within the O_2 molecule caused by the electric field of the TiO_2 surface.

TABLE OF COTNENTS

LIST OF TABLES

LIST OF FIGURES

PREFACE

I would like to thank my advisor, Dr. J. Karl Johnson, for his guidance and insight. I would also like to thank the National Energy and Technology Laboratory for supporting my career as a graduate student. Finally I really appreciate all other my PhD committee members, Dr. Kenneth D. Jordan, Dr. Robert M. Enick, and Dr. Wei Shi to participate in my proposal and thesis defense.

1.0 INTRODUCTION

1.1 CO_2 CAPTURE

Carbon dioxide is widely accepted as the one of the primary greenhouse gases implicated in global climate change.[1, 2] There are studies showing that annual global emissions of CO_2 have increased sharply (about 80% more than 1970 in 2004).[3] It is projected as energy usage will double in the next 50 years and that this increasing trend will be even stronger, since most energy sources nowadays are coming from carbon and its derived products, such as coal, natural gas, petroleum and biomass. Alternative energy sources that make no contribution to CO_2 emission are still in the development phase and not likely to replace a significant fraction of current carbon-based energy sources in the near future. Therefore capture, compression, transport, and permanent storage of CO_2 are of critical importance to maintain or even reduce the CO_2 level in the atmosphere. Large-scale CO_2 emission processes, such as coal-fired power plants, require not only highly efficient CO_2 capture materials to adsorb/separate CO_2 from flue/fuel gas but also CO_2 capture materials with large capacity to handle high CO_2 throughput. This is a great challenge for current adsorption/separation materials; thus, new materials should be explored to find suitable candidates for CO_2 capture. There are almost infinite number of potential materials that can be synthesized with the ability to capture CO_2. However, it is inefficient and impractical to synthesize all the potential candidate materials and verify their abilities to capture CO_2

effectively. Theoretical computation could possibly make a big contribution to facilitate the discovery of new materials for CO_2 capture by providing a method for screening a large number of potential candidate materials, providing thermodynamic data for materials before they are synthesized, thereby identifying the best candidates for experimental study.

Material properties calculations with quantum mechanics-based computational methods have undergoing remarkable progress in last twenty years.[4, 5] One of the most successful quantum mechanical methods is density functional theory (DFT). It is based on the postulate that the many-body electron-electron interactions can be described by an effective one-electron potential that is only dependent on the electron density. This is manifested in the Kohn-Sham equation.[6] Numerous studies have shown that DFT can predict accurate structures, energetics and other properties of various materials.[4, 7] However, DFT with commonly used functionals is also known for not properly describing the van der Waals (vdW) interaction[8] nor the band gap for insulators and semiconductors.[9]

Molecular simulation is a useful tool to predict thermodynamic and transport properties of physically/chemically interacting systems.[10] The key to successful simulations is the development of a force field that can accurately describe the interaction between the atoms or the molecules in the system. Classical force fields are normally comprised of a set of parameters in various functional forms describing different potential energy components, such as bond, angle, torsion, Coulomb, and van der Waals terms.[11] There are also reactive type force fields that include more parameters to better describe chemical interactions and reactions.[12-14] The main advantage of molecular simulation methods is that they are much faster compared to quantum mechanical calculations, especially for large system scale (thousands of atoms) and long time scale (several nanoseconds) simulations. One of the problems with molecular simulations is that

unlike the quantum mechanical methods, the accuracy of the force fields is hard to improve systematically.

There are already many experimental efforts for using alkali metal (Li, Na, K) compounds as effective CO_2 capture materials. Mosqueda and coworkers[15] found that Li_2O is a better sorbent than other lithium ceramics and that CO_2 adsorption is limited by the diffusion of CO_2 through the formed shell of Li_2CO_3. NaOH has also been used for high temperature CO_2 capture in conjunction with CaO.[16] 90% of the CO_2 from simulated flue gas can be captured by dry Na_2CO_3 sorbents at temperatures as low as 60 °C.[17] Lee *et al*. have studied a number of different K based sorbents, such as K_2CO_3/Al_2O_3[18], K_2CO_3/MgO[19] and K_2CO_3/ZrO_2[20]. All those CO_2 capture processes require that CO_2 reacts with those aforementioned materials and then the products decompose to release CO_2. There are, however, little theoretical studies on those reactions. Duan *et al.* studied CO_2 capture through the reaction of $Li_2O + CO_2 \rightleftharpoons Li_2CO_3$ with DFT methods from a thermodynamic perspective.[21] Therefore, it is necessary to examine the reaction thermodynamics of CO_2 with various possible alkali metal compounds with the help of computational tools. In Chapter 2, we focus on the thermodynamics of alkali metal oxides and hydroxides reactions with CO_2 to form alkali metal carbonates or bicarbonates, as computed from DFT methods. Akbarzadeh *et al.* have developed a linear programming algorithm to explore the phase diagrams of multicomponent hydride systems with the energies calculated from DFT.[22] Alapati *et al.* applied this methodology to screen metal hydride mixtures for reversible hydrogen storage with high capacity and favorable thermodynamics. In this scheme, only one gas species, H_2, has been considered.[23] In Chapter 2 and 3, we extend this method to CO_2 capture reactions by explicitly considering two gas species, *i.e*., CO_2 and H_2O, because hydroxides reacting with CO_2 will generate water. This adds one more dimension of complexity

to the problem. With the phase diagrams obtained from this method, we can calculate the temperature and partial pressures of gas phase species for the reactions relevant to CO_2 capture. Finally, we can conclude if the material is suitable for CO_2 capture by comparing the reaction thermodynamics and conditions with the set criteria.

One of the advantages of DFT methods is that the accuracy can, in principle, be improved by utilizing higher level functionals in a "Jacob's ladder" approach to density functional approximations. Perdew *et al.* suggest there are five rungs in the DFT "Jacob's ladder" to achieve chemical accuracy.[24] They are local spin-density approximation (LSD)[6], generalized gradient approximation (GGA)[25-29], meta-GGA[30-32], hyper-GGA or hybrid functionals[33, 34], and the generalized random phase approximation (RPA)[35]. Currently, the first three rungs functional have been successfully constructed by satisfying fundamental constraints instead of fitting to any training sets.[24] Theoretically, as the functional form to describe the exchange-correlation becomes more complex when climbing the "ladder", the energy will be more accurate. At the same time, the computational cost will also increase. For example, one may expect going from the LSD level to the GGA level, or going from the GGA level to the meta-GGA level, that the accuracy of the calculation in terms of the geometry, energetics and many other properties of chemical substances will be improved. However, it turns out that this is not always the case. We will illustrate this point in Chapter 3 by comparing the performance of different functionals at the GGA and the meta-GGA levels for transition metal oxides, hydroxides and carbonates. We also evaluated the CO_2 capture capability of these materials at pre-combustion and post-combustion conditions using the same approach described in Chapter 2.

In addition to solid sorbents, ionic liquids (ILs) are also extensively studied by numerous groups because of their ability to absorb CO_2.[36-38] ILs consist exclusively of ionic species and

have melting points or glass-transition temperatures lower than 100 °C.[39] They generally are comprised of organic cations, which have cyclic or non-cyclic centers containing several linear alkyl chains attached to one or more nitrogen, phosphorous or sulfur groups and various anions. Figure 1.1 and Figure 1.2 illustrate some common cations and anions.

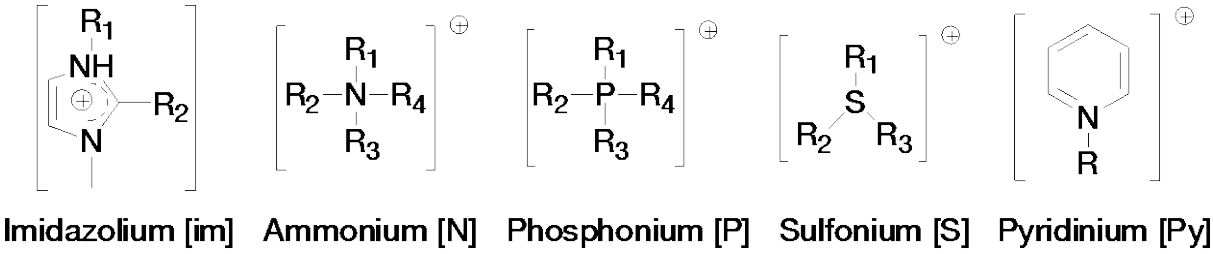

Figure 1.1. Some common ionic liquid cations. R can be methyl, ethyl, butyl, hexyl, octyl etc.

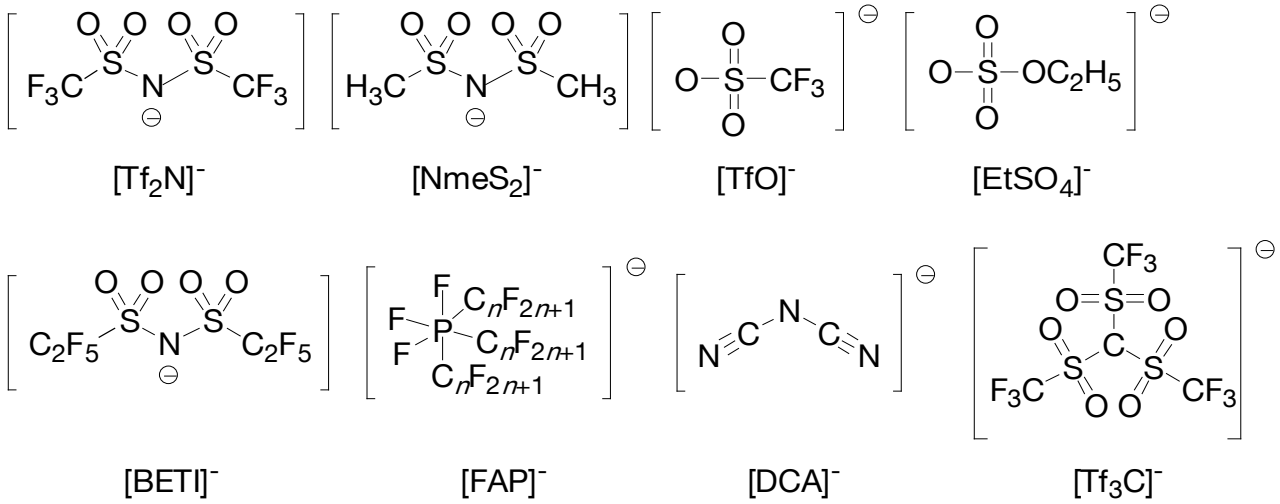

Figure 1.2. Some common ionic liquid anions.

Conventional ILs often do not have any functional groups that react with CO_2. Imidazolilium based ionic liquids comprise many in this category. They can physically absorb CO_2 through a space-filling mechanism.[40, 41] In order to increase the solubility of CO_2 in ILs,

functionalization with CO_2-philic functional groups to prepare task-specific ILs[42-44], polymerization of ILs[45-47], and confinement of ILs into some support materials[48] have been used. Task-specific ILs have drawn much attention because their CO_2 uptake capacity is increased significantly due to strong interactions between CO_2 and CO_2-philic functional groups. However, they suffer from slow dynamics of CO_2 diffusion due to high viscosity upon reaction.[42] This could be a major concern if these ILs would be used in practice. Therefore, it is important to find new task-specific ILs that have high CO_2 solubility and low viscosity. To study the transport properties as well as the adsorption of ILs with CO_2 systems, molecular simulations will be more suitable than quantum mechanical molecular dynamics since they are much less expensive. Classical force field-based methods have already used extensively to study the CO_2 physical adsorption in ILs.[36, 37] Classical force fields are often fitted to training sets including bond lengths, angles that are not far away from their equilibrium values. Thus, classical force fields can only be accurate when describing similar systems since they normally use harmonic or similar potentials to model bond lengths, angles, and torsions. These features make them inadequate for describing the systems with bond breaking and bond forming events, *i.e.*, chemical reactions. Therefore, modeling ILs that can strongly interact with CO_2 and even react with CO_2, such as tetrabutylphosphonium glycinate ($[P(C_4)_4][Gly]$), requires force fields that can adequately describe bond order/bond energy relationships. ReaxFF is designed to bridge the gap between classical force field and quantum mechanical methods.[14, 49] It will calculate bond order at every molecular dynamics or energy minimization step based on the interatomic distances. The main features of ReaxFF are that the energy/forces description is continuous even when the bond is breaking; one element only has one force field description even in different chemical environments; *a priori* reaction site information is not needed to predict where a reaction will

occur. Those features make it suitable to describe systems where chemical reactions could occur at much less computational expense compared with quantum mechanical methods, which could also describe chemical reactions properly. The development and validation of a ReaxFF force field that can describe the interaction/reaction between $[P(C_4)_4][Gly]$ with CO_2 will be discussed in Chapter 4.

1.2 O_2 ADSORPTION ON THE TiO_2(110) SURFACE

There has been tremendous progress on understanding the surface chemistry on TiO_2 surfaces since the first discovery of photolysis of water on TiO_2 electrodes.[50, 51] TiO_2 has been used extensively for photooxidation catalysts and catalysts supports.[51-53] The first step in oxidation catalysis is often the O_2 adsorption onto the TiO_2 surfaces. Rutile TiO_2(110) is the most studied single crystal TiO_2 surface[54] because it is the most stable surface of the most stable phase of TiO_2. Besides numerous experimental studies on O_2 adsorption on the TiO_2(110) surface[55-57], there are also many theoretical studies on this material, most of which utilize the DFT methods under periodic conditions.[58, 59] Many of them are limited to O_2 adsorption on defect TiO_2(110) surfaces where O_2 can chemically interact with the defect sites because current DFT lacks proper description of long range vdW interactions[8] due to the local or semi-local nature of LDA or GGA functionals. There have been several different methods proposed to account for vdW interaction within DFT, such as DFT-D,[60-62] van der Waals functional (vdW-DF),[63] dispersion-corrected atom-centered potentials (DCACPs),[64] symmetry-adapted perturbation theory (SAPT).[65, 66] One of simplest corrections, although empirical, is DFT-D.[61, 62] It adds an empirical dispersion energy term in addition to the usual self consistent Kohn Sham energy. In Chapter 5, we will use this

vdW augmented DFT (DFT-D2) method to study weakly bound molecular O_2 on the TiO_2(110) surface in order to compare with recent experimental findings[67] of non-zero infrared intensity for the weakly adsorbed O_2. The potential energy surface, vibrational frequency and infrared intensity of O_2 on TiO_2(110) have been calculated. The results from the calculations are used to interpret the experimental observations, as presented in Chapter 5.

2.0 DENSITY FUNCTIONAL THEORY STUDIES ON THE ELECTRONIC, STRUCTURAL, LATTICE DYNAMICAL, THERMOSTABILITY AND CO_2 CAPTURE PROPERTIES OF ALKALI METAL BICARBONATES

The Content of this chapter is taken from Yuhua Duan, Bo Zhang, Dan C. Sorescu and J. Karl Johnson, "CO_2 capture properties of M-C-O-H (M=Li, Na, K) systems: a combined density functional theory and lattice phonon dynamics study", Journal of Solid State Chemistry, 184, 304-311 (2011) and Yuhua Duan, Bo Zhang, Dan C. Sorsecu, J. Karl Johnson, Eric H. Majzoub, David R. Luebke, "Density functional theory studies on the electronic, structural, phonon dynamical and thermo-stability properties of bicarbonates $MHCO_3$, M=Li, Na, K" Journal of Physics: Condensed Matter, 24, 325501 (2012).

Yuhua Duan did all the geometry relaxation calculations for all compounds. The author did phonon calculations for all bicarbonates and Yuhua Duan did the calculations for all the other compounds. All the calculations, figures and tables in section 2.3.1 and 2.3.2 were produced by the author. All the other sections are written by Yuhua Duan with contributions from the author.

2.1 INTRODUCTION

Carbon dioxide from large stationary sources such as power plants has been identified as one of the leading causes of global warming.[68-70] Carbon-free renewable energy sources are not likely to completely replace fossil fuel power plants for many years to come.[71] Hence, there is a need to reduce CO_2 emission by carbon capture and sequestration so that fossil fuel power plants may be operated without releasing enormous quantities of CO_2 into the atmosphere.[72-74] Current technologies for capturing CO_2 include solvent-based systems (such as MEA, Selexol, Rectisol), and alkanolamine-based materials (such as ethanolamine). It is generally accepted that operation or regeneration of these materials is too energy intensive.[68, 69] Hence, there is critical need for development of new materials that can capture and release CO_2 reversibly with acceptable energy and operating costs. Accordingly, solid sorbent materials have been proposed for capture of CO_2 through a reversible chemical transformation. Among them, regenerable solid sorbents play an important role for CO_2 capture, especially above room temperature (~100°C for post-combustion, ~300°C for pre-combustion).[18, 19, 69, 75-80]

There are multiple opportunities to capture carbon in conjunction with power generation. Two of these are post- and pre-combustion capture. In post-combustion capture CO_2 is separated from the flue gas from a power plant. The flue gas is typically at low pressure (just over atmospheric) and moderate temperature (<100°C). The concentration of CO_2 in flue gas is 10-15% by volume. The second option is to capture CO_2 at the pre-combustion stage, as in gasification-type power generation such as in the integrated gasification combined cycle (IGCC). In this scenario, a fossil fuel such as coal or biomass is converted to synthesis gas, from which CO_2 can be captured before being mixed with air in a combustion turbine. The concentration of

CO_2 in the pre-combustion stream is typically at a pressure of 15~20 bar and temperatures 250°C ~300°C.

In this chapter we assess the suitability of solid sorbents containing alkali metals for capturing CO_2 from both post- and pre-combustion streams using a theoretical approach. These materials have previously been investigated.[20, 21, 69, 79, 81-83] Alkali metal oxides and hydroxides have attracted interest because of their ability to absorb high weight percentages of CO_2 at moderate working temperatures[84]. Moreover, experimental studies indicate that mixtures of hydroxides with oxides can improve the CO_2 absorption performance.[79, 82]

There have been very few theoretical studies of CO_2 reactions with alkali oxides and hydroxides up to this point. In contrast, there are many experimental studies on this topic.[84, 85] Based on thermodynamic data, Feng *et al.*[86] analyzed 11 simple metal oxides and concluded that CaO is thermodynamically the best candidate among them for CO_2 capture in zero emission power generation systems. Based on density functional theory (DFT), Jensen *et al.*[87] investigated the CO_2 adsorption on CaO and MgO surfaces. Their results showed that CO_2 adsorbs as monodenate on edge sites and bidentate on corner sites of MgO. In contrast, CO_2 adsorbes as monodenate on both edge and corner sites of CaO.

Recently, Duan and Sorescu proposed a methodology to identify promising solid sorbent candidates for CO_2 capture by combining DFT total energy calculations with lattice phonon dynamics.[21, 83] For Li_2O solid, it was concluded that although pure Li_2O can absorb CO_2 efficiently, it is not a good solid sorbent for CO_2 capture because the reverse reaction, corresponding to Li_2CO_3 releasing CO_2, can only occur at very low CO_2 pressure or at very high temperature when Li_2CO_3 is in the liquid phase.[21] These predicted results are in very good agreement with experimental measurements.[15] In this study, we apply our previously developed

computational methodology to systems containing alkali metal oxides, hydroxides, and carbonates to explore their CO_2 capture properties systematically. We present a linear programming approach to identify the families of reactions that lie on the convex hull of the Gibbs free energy for the M-C-O-H systems for M=Li, Na, and K. In this work we consider solid phases consisting of only the oxides, hydroxides, carbonates, and bicarbonates. We compare our predictions with available thermodynamic data to assess the accuracy of our approach.

2.2 COMPUTATIONAL DETAILS AND METHODOLOGY

2.2.1 Computational details

The crystal structures of solid compounds studied in this work were selected from the inorganic crystal structure database (ICSD).[88] We have chosen to use the structure with the lowest energy, as computed from DFT at zero temperature, when more than one structure is reported for a given compound. Since no experimental crystal structure of $LiHCO_3$ is available to use, two methods were employed to identify the most possible structure of $LiHCO_3$. One method is the ICSD database search which is based on known ABC_3 structures and A or B site atom are substituted with Li. In addition to the ICSD structure search, the PEGS (Prototype Electrostatic Ground States) method[89] was used to produce prototype structures for $LiHCO_3$. The PEGS method uses a simplified Hamiltonian consisting of electrostatic interactions and soft-sphere repulsion, combined with Metropolis Monte Carlo global optimization and potential energy smoothing to produce prototype structures for evaluation using DFT. Details of the method can be found

elsewhere.[89] Surprisingly, the database search yielded a lower energy structure than the PEGS approach. We will use the ground state structure obtained by crystallographic database search.

Many calculations in this work were performed with the Vienna *ab-initio* simulation package (VASP),[90-93] which is a periodic plane-wave DFT code. Core-electron interactions were described by projector augmented-wave (PAW) potentials.[94, 95] We used generalized gradient approximation (GGA) with PW91 exchange-correlation functional of Perdew and Wang.[96, 97] A plane-wave basis cutoff energy of 520 eV was used for all calculations. The k-point meshes were generated using the Monkhorst-Pack method[98] with a spacing of around 0.027 $Å^{-1}$ between k-points along the axes of the reciprocal unit cells.[21] The conjugate gradient algorithm was used to perform geometry relaxation of all atomic positions, cell shape, and cell volume using a stopping criterion of energy less than 0.01 meV.

Phonon dispersion calculations and their contribution to the free energy were obtained using the formalism derived by Parlinski *et al*.[99] These calculations were done in VASP with the PW91 exchange-correlation functional.[96, 97] The energy cutoff is the same as listed above for our total energy calculations except the structures were relaxed until the forces were less than 0.1 meV/Å. Each symmetry-nonequivalent atom was displaced along all symmetry nonequivalent directions by 0.01 ~ 0.05 Å and forces on all atoms were calculated to construct the dynamical matrix. It is necessary to use a relatively large supercell to avoid interactions between images of the displaced atom.

2.2.2 Methodology

To determine phase diagrams of multi-component systems, we assume that all possible solid phases are in contact with a gas-phase reservoir having specified partial pressures of CO_2 and H_2O. The grand-canonical Gibbs free energy of such system can be written as[22]

$$G(T,\mu_{\text{gas}}) = \sum_{j=1}^{S} x^j F^j(T) - \sum_{k}\sum_{j=1}^{S} \mu_k^{\text{gas}}(T,p) x_k^{j,\text{gas}}, \tag{2.1}$$

where $F^j(T)$ is the free energy of solid phase "j" (ignoring the pV term contribution), S is the number of solid substances, $\mu_k^{\text{gas}}(T,p)$ is the chemical potential of gas species k, x^j is the unknown mole fraction of phase j coexisting at a given composition, temperature, and pressure. The mol fraction x^j is based on elements appearing only as solids (in this case only the metals). $x_k^{j,\text{gas}}$ is the theoretical mol fraction of gas species k contained in phase j.

The x^j mole fractions are determined by minimizing the grand-canonical Gibbs free energy, subject to the following mass-conservation constraints for the solid phase species

$$\sum_{i=\text{metal}}^{M} f_i = \sum_{i=\text{metal}}^{M}\sum_{j=1}^{S} x^{j,\text{solid}} b_i^{j,\text{solid}} = 1, \tag{2.2}$$

where f_i is the molar ratios of solid element i, $b_i^{j,\text{solid}}$ represents the number of atoms of type i in one formula unit of phase j, and M is the number of elements. These two equations form a linear programming problem that can be solved using existing techniques. The conditions at which a chemical reaction occurs can be identified by comparing the mole fractions x^j at two consecutive temperature or pressure steps. If x^j values change then a reaction occurred between the temperature or pressure interval. We can choose sufficiently small intervals of temperature and pressure to ensure adequately small chemical potential changes between two steps in order to

guarantee single step reactions. The change in the Gibbs free energy of the system due to a reaction is zero at thermodynamic equilibrium and can be calculated by

$$\Delta G = 0 = \Delta F_{\text{solid}} + \sum n_g \mu_g, \tag{2.3}$$

where n_g is the number of moles of gas molecules g consumed or released as a result of the reaction. The locus of points that satisfy Eq. (2.3) as a function of temperature and pressure define the equilibrium phase diagram.

The chemical potentials of CO_2 (μ_{CO_2}) and H_2O (μ_{H_2O}) required in Eqs. (2.1) and (2.3) can be obtained from standard statistical mechanics (assuming ideal gas behavior):

$$\mu_{CO_2}(T,p) \approx E_{CO_2}^{DFT} + \frac{7}{2}RT + \sum_{i=1}^{4} \frac{N_a h\nu_i}{e^{-\frac{h\nu_i}{kT}} - 1} - TS_{CO_2}(T) - n_{CO_2} RT \ln\left(\frac{p_{CO_2}}{P_0}\right), \tag{2.4}$$

$$\mu_{H_2O}(T,p) \approx E_{H_2O}^{DFT} + 4RT + \sum_{i=1}^{3} \frac{N_a h\nu_i}{e^{-\frac{h\nu_i}{kT}} - 1} - TS_{H_2O}(T) - n_{H_2O} RT \ln\left(\frac{p_{H_2O}}{P_0}\right), \tag{2.5}$$

where N_a is Avogadro's constant. The entropy of CO_2 (S_{CO_2}) and H_2O (S_{H_2O}) can be accurately calculated from the Shomate equation.[100]

The free energy of each solid phase ($F_j(T)$ in Eq. (2.1)) can be computed from

$$F(T) = E^{DFT} + F_{harm}(T), \tag{2.6}$$

where E^{DFT} is the total energy of each solid calculated from DFT.

2.3 RESULTS AND DISCUSSION

2.3.1 Equation of state of bicarbonates

The equations of state for $MHCO_3$ with M=Li, Na, and K are plotted in Figure 2.1, where it can be seen that the unit-cell energy and the cohesive energy (shown in Table 2.1) for $MHCO_3$ increase from Li to K. For $KHCO_3$, the high-pressure phase (form III, #2) has a cohesive energy that is smaller in magnitude than the corresponding low-temperature (form I, #14) and high-temperature (form II, #12) phases. We have fitted the DFT data in Figure 2.1 to the Birch-Murnaghan equation of state[101, 102], given by

$$E(V) = E_0 + \frac{9V_0B_0}{16}\left\{\left[\left(\frac{V_0}{V}\right)^{\frac{2}{3}} - 1\right]^3 B_0^{'} + \left[\left(\frac{V_0}{V}\right)^{\frac{2}{3}} - 1\right]^2 \left[6 - 4\left(\frac{V_0}{V}\right)^{\frac{2}{3}}\right]\right\}. \quad (2.7)$$

The fitted parameters (E_0, V_0, B_0, $B_0^{'}$) for $MHCO_3$ are listed in Table 2.1. The bulk modulus B is defined as $B = B_0 + B_0^{'}P$ in this scheme, where P is the pressure and set to 1atm for ambient conditions and 5.5 GPa for the high pressure phase of $KHCO_3$. We constrained $B_0^{'}$ to lie in the range [2, 6] in the fitting routine, since most values of $B_0^{'}$ fall in this range. The fitted equations of state curves are also plotted in Figure 2.1.

Table 2.1. The calculated bulk modulus, cohesive energy (E_{coh}), and the fitted parameters of Birch-Murnaghan equation of state for bicarbonates $MHCO_3$, M=Li, Na, K.

Crystal		E_0 (eV/cell)	B_0 (eV/Å^3)	B_0'	V_0 (Å^3)	Bulk Modulus (GPa)	E_{coh} (eV)
$LiHCO_3$		-155.36 (-155.28)[a]	0.062	3.466	288.8 (285.5)[a]	9.90	-31.74
$NaHCO_3$		-152.21 (-152.20)	0.185	3.487	261.9 254.7[b]	29.59	-29.78 (-28.40)[f]
$KHCO_3$	$P12_1/a1$ (#14)	-151.79 (-151.75)[a]	0.113	3.484	328.0 306.6[c]	18.10	-29.67 (-28.34)[f]
	C12/m1 (#12)	-151.80 (-151.75)[a]	0.127	3.502	336.5 307.6[d]	20.42	-29.67
	Pī (#2)	-70.84 (-70.84)[a]	0.199	3.500	136.0 125.8[e]	60.84	-27.15

[a] Obtained from full optimization.
[b] From Ref. 103.
[c] From Ref. 104.
[d] From Ref. 105.
[e] From Ref. 106.
[f] Obtained by subtracting the atom formation energy from the experimental formation energy of the bicarbonates at 298.15 K.[100, 107]

The cohesive energy (E_{coh}) is calculated by subtracting the total bulk energy (E_0 in Table 2.1) from the sum of total energies of the isolated spin-polarized atoms (Li, Na, K, O, C, H) using the same level calculations. These isolated atom energies are E_{Li}= -0.27065 eV/atom, E_{Na}= -0.20469 eV/atom, E_K= -0.15544 eV/atom, E_H= -1.11573 eV/atom, E_C= -1.21255 eV/atom, and E_O= -1.49139 eV/atom.

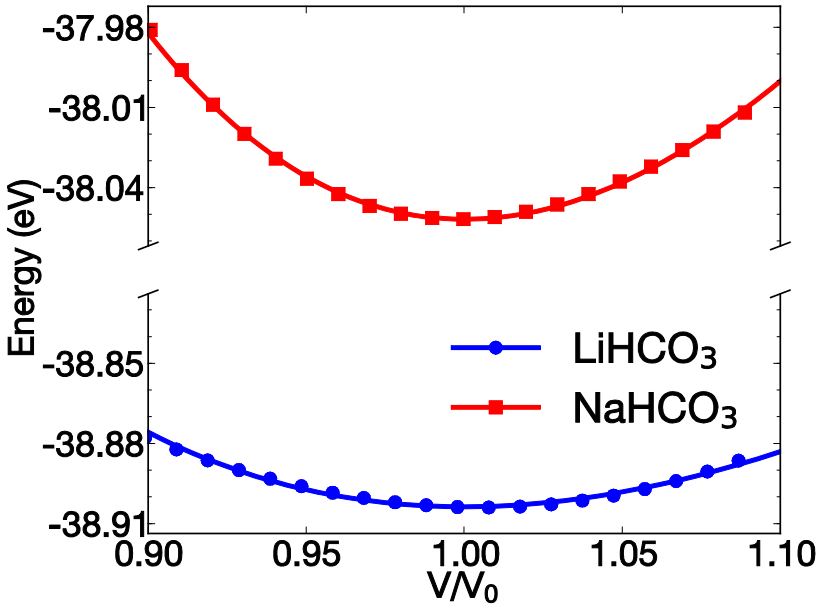

(a)

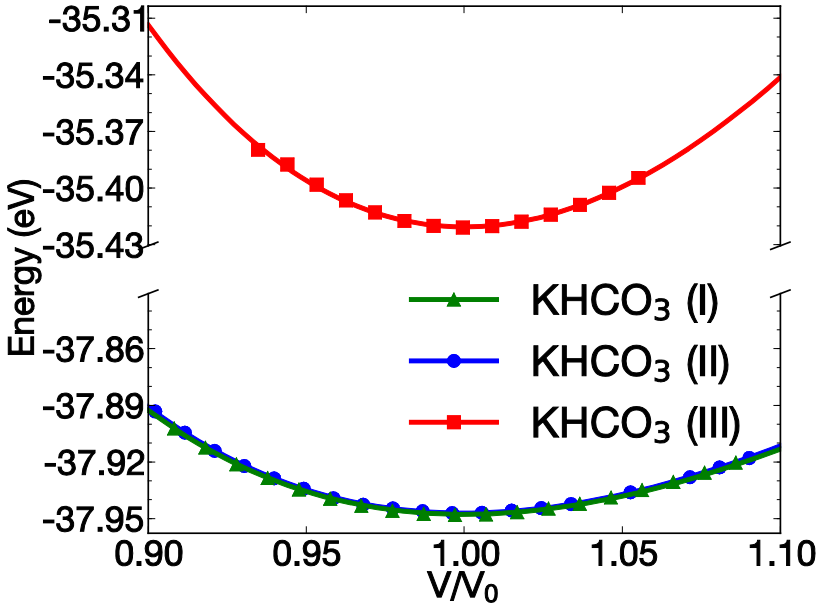

(b)

Figure 2.1. The calculated total energy versus the relative cell volume. (a) $LiHCO_3$ (circles) and $NaHCO_3$ (squares) (b) $KHCO_3$, form I, #14 (triangles), form II, #12 (circiles), form III, #2 (squares).

2.3.2 Phase diagrams of M-C-O-H systems

The calculated phase diagrams of M-C-O-H for M=Li, Na, and K are shown in Figure 2.2(a), Figure 2.3(a), and Figure 2.4(a) respectively. The three independent variables in the phase diagram are the temperature, the partial pressure of CO_2 and the partial pressure of H_2O. The surfaces shown in the figures correspond to chemical reactions (phase transitions), which are identified in the legends of the graphs. The following general features can be seen from Figure 2.2(a), Figure 2.3(a), and Figure 2.4(a): at low temperature and high CO_2 pressure, the most stable phase is $MHCO_3$. When the temperature is increased, $MHCO_3$ is converted to carbonate, M_2CO_3, which is stable over quite wide ranges of temperature and pressure. The MOH phase is stable at low CO_2 partial pressure, high H_2O partial pressure, and lower temperatures. At very high temperatures and low CO_2 partial pressure, the M_2O phase is stable.

The calculated heats of reaction and free energies of reaction for nine reactions involving capture of CO_2 are given in Table 2.2, along with the corresponding data from the HSC Chemistry package[108]. The partial pressures of CO_2 and H_2O are set to 1 bar in the finite temperature calculations. The calculated heats of reaction (ΔH) for the carbonate to bicarbonate reactions are plotted in Figure 2.6 as a function of temperature along with data from the HSC chemistry package. The calculated heats of reactions and Gibbs free energy changes (ΔG) at 300K are given in Table 2.2. The DFT data deviate by about 15 to 25 kJ/mol from the HSC data for the CO_2 capture reactions involving alkali metal oxides and hydroxides. However, reactions involving $M_2CO_3/MHCO_3$ (M=Na, K) show much better agreement with the HSC data, deviating by a few kJ/mol.

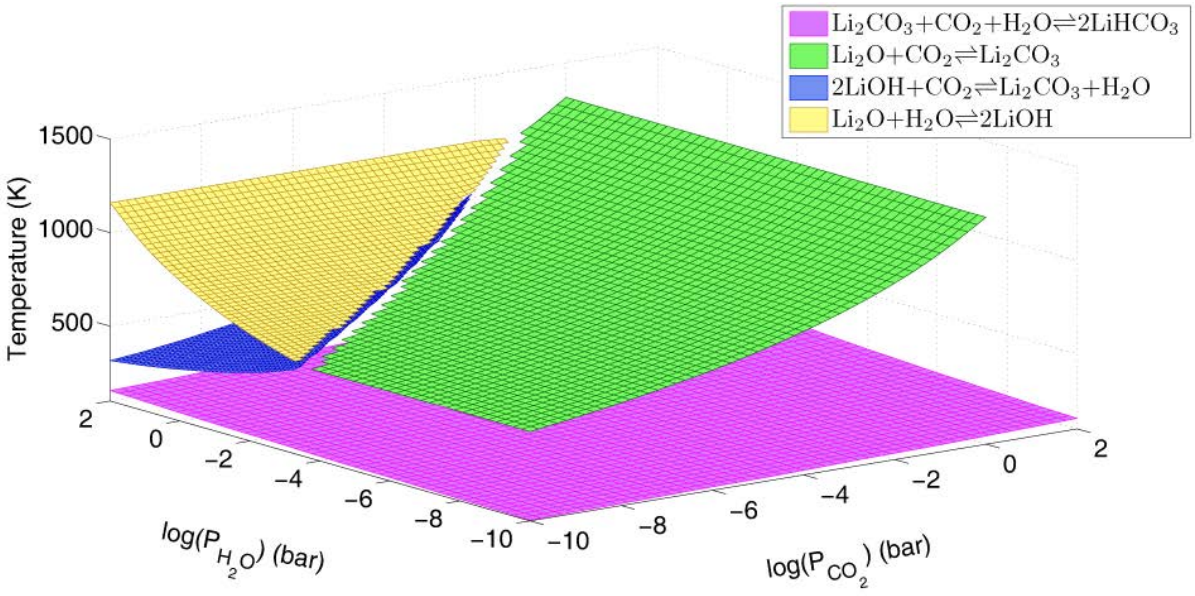

(a)

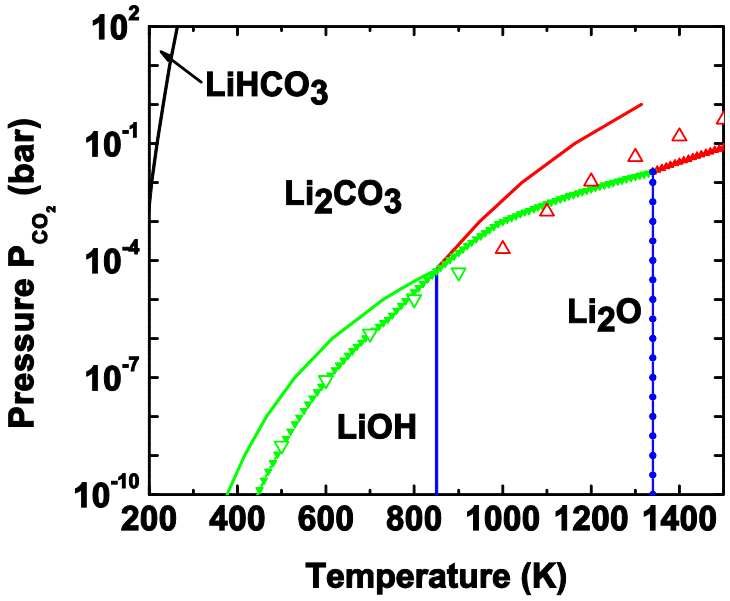

(b)

Figure 2.2. The calculated phase diagram of Li-O-C-H systems with the relationships of *T*, P_{CO_2} and P_{H_2O}. (a) Three dimensional plot; (b) Two dimensional plot at fixed P_{H_2O} =1bar. Solid lines represent the phase boundary calculated from DFT. For comparison, the available experimental data from the HSC Chemistry package (solid lines, filled symbols) and JANAF tables (open symbols) are also potted. Phases are labeled according to our DFT results, boundaries are colored. Black: $Li_2CO_3 + CO_2 \rightleftharpoons 2LiHCO_3$; Red: $Li_2O + CO_2 \rightleftharpoons Li_2CO_3$; Green: $2LiOH + CO_2 \rightleftharpoons Li_2CO_3 + H_2O$; Blue: $Li_2O + H_2O \rightleftharpoons 2LiOH$.

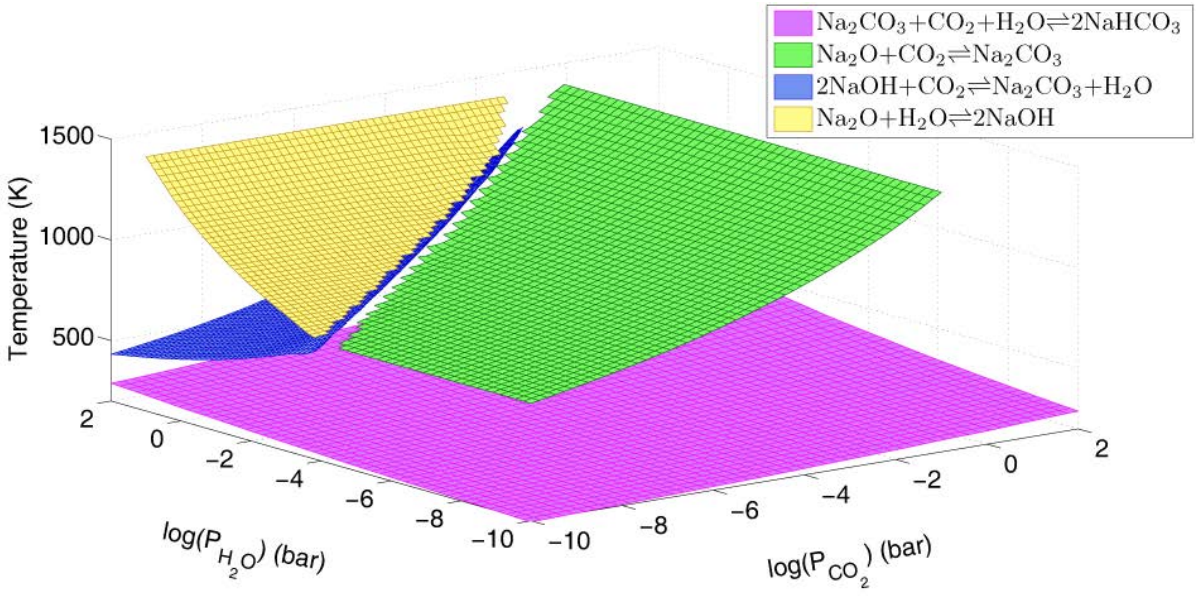

(a)

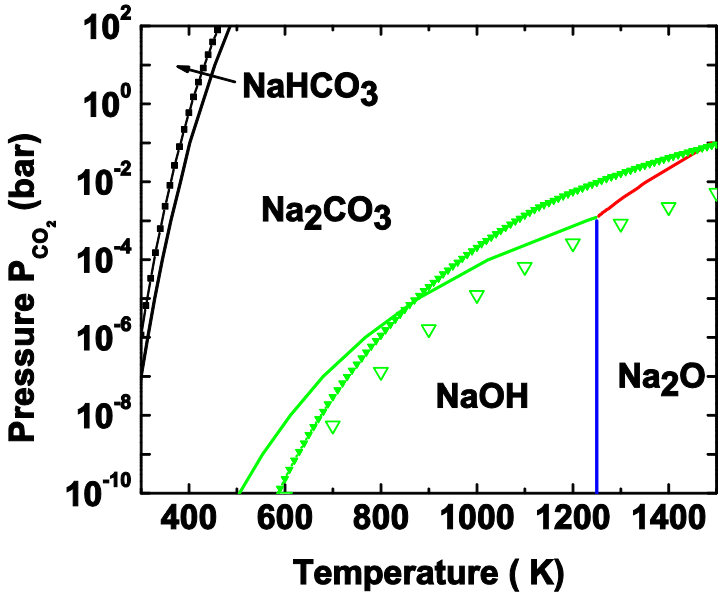

(b)

Figure 2.3. The calculated phase diagram of Na-O-C-H systems with the relationships of T, P_{CO_2} and P_{H_2O}. (a) Three dimensional plot; (b) Two dimensional plot at fixed P_{H_2O} =1bar. Solid lines represent the phase boundary calculated from DFT. For comparison, the available experimental data from the HSC Chemistry package (solid lines, filled symbols) and JANAF tables (open symbols) are also potted. Phases are labeled according to our DFT results, boundaries are colored. Black: $Na_2CO_3 + CO_2 \rightleftharpoons 2NaHCO_3$; Red: $Na_2O + CO_2 \rightleftharpoons Na_2CO_3$; Green: $2NaOH + CO_2 \rightleftharpoons Na_2CO_3 + H_2O$; Blue: $Na_2O + H_2O \rightleftharpoons 2NaOH$.

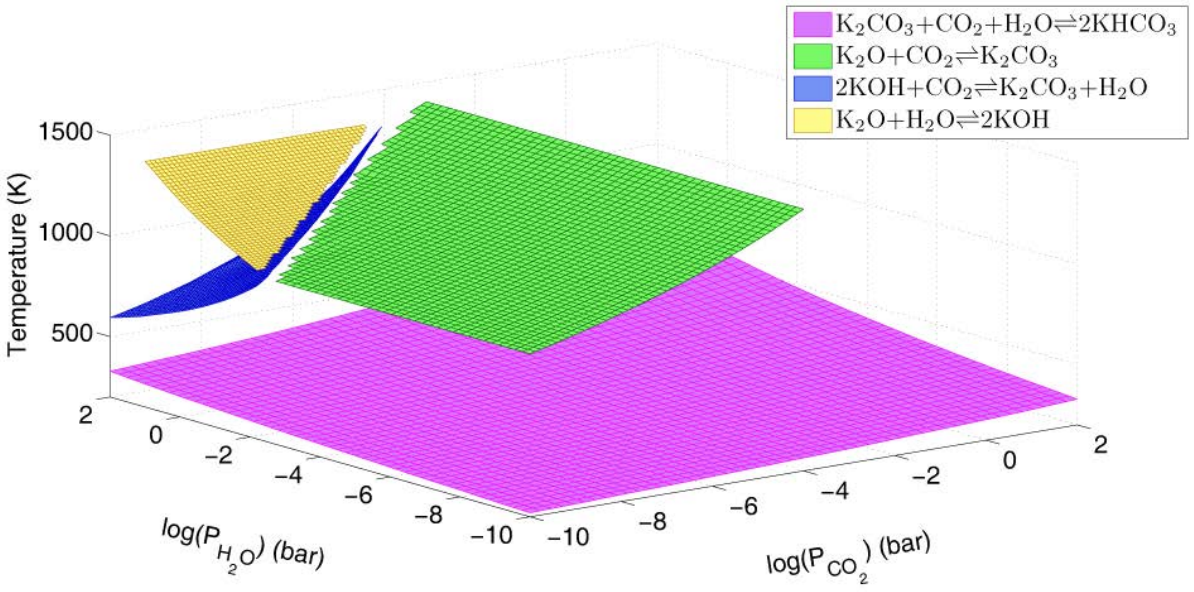

(a)

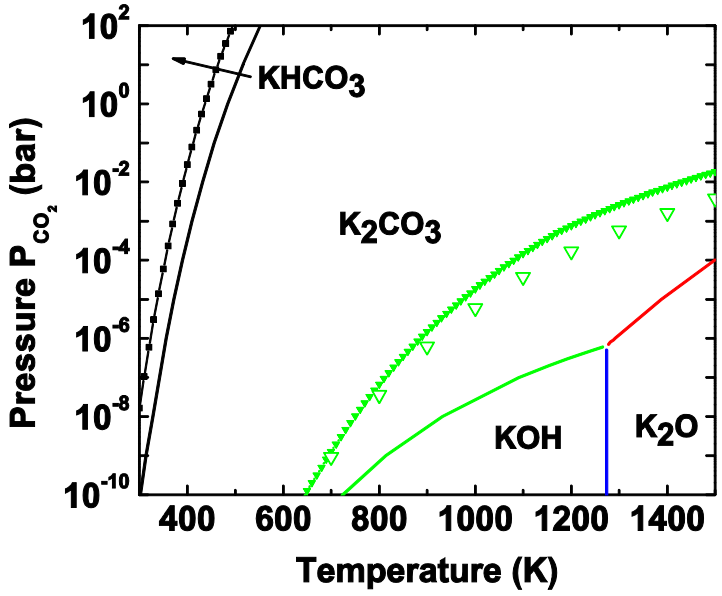

(b)

Figure 2.4. The calculated phase diagram of K-O-C-H systems with the relationships of T, P_{CO_2} and P_{H_2O}. (a) Three dimensional plot; (b) Two dimensional plot at fixed P_{H_2O} =1bar. Solid lines represent the phase boundary calculated from DFT. For comparison, the available experimental data from the HSC Chemistry package (solid lines, filled symbols) and JANAF tables (open symbols) are also potted. Phases are labeled according to our DFT results, boundaries are colored. Black: $K_2CO_3 + CO_2 \rightleftharpoons 2KHCO_3$; Red: $K_2O + CO_2 \rightleftharpoons K_2CO_3$; Green: $2KOH + CO_2 \rightleftharpoons K_2CO_3 + H_2O$; Blue: $K_2O + H_2O \rightleftharpoons 2KOH$.

In order more easily visualize the effect of CO_2 partial pressure, we fixed P_{H_2O} =1 bar and have plotted the corresponding two-dimensional slices from Figure 2.2(a), Figure 2.3(a), and Figure 2.4(a) in Figure 2.2(b), Figure 2.3(b), and Figure 2.4(b). We have also plotted the reactions from the HSC Chemistry database[108] and the JANAF tables[100] in Figure 2.2(b), Figure 2.3(b), and Figure 2.4(b) in order to compare our DFT calculations with the pseudo-experimental data. Since there are no experimental data for $LiHCO_3$, only the DFT calculated curve for the $LiHCO_3/Li_2CO_3$ reaction is shown in Figure 2.2(b). We see from our calculations that $LiHCO_3$ is predicted to exist only at low temperatures and at high CO_2 pressure, e.g. at T=273 K and $P_{CO_2} > 10^2$ bar. This may explain why solid $LiHCO_3$ has not been observed experimentally at ambient conditions. It would be interesting to carry out high pressure experiments to see if $LiHCO_3$ could be observed.

Given that crystalline $LiHCO_3$ has not been experimentally observed[109], we have examined in more detail the conditions of temperature and partial pressures of CO_2 and H_2O under which one might expect to observe crystalline $LiHCO_3$ based on our DFT and phonon free energy calculations. In Figure 2.5 we have plotted three stability curves for $LiHCO_3$ and Li_2CO_3 as a function of temperature and P_{CO_2}, each at different fixed values of P_{H_2O}. The values of P_{H_2O} are (from left to right) 10^{-4}, 10^{-3}, and 10^{-2} bar, while the vertical lines are the ice sublimation or boiling temperatures at each of those values of pressure. Hence, the required partial pressure of water will likely only be available above these temperatures on each of the curves.

Table 2.2. The calculated reaction thermodynamics of CO_2 capture by alkali metal oxides, hydroxides and carbonates. Enthalpies and Gibbs free energies correspond to partial pressures of CO_2 and H_2O of 1 bar.

Reactions	CO_2 wt%	Calculated thermodynamic properties (kJ/mol)				HSC data[a] at T=300K	
		ΔE^{DFT}	ΔE^{ZP}	ΔH^{cal} (T=300K)	ΔG^{cal} (T=300K)	ΔH (kJ/mol)	ΔG (kJ/mol)
$Li_2O + CO_2 = Li_2CO_3$	142.52	-204.786	4.521	-200.531	-153.061	-224.643	-176.290
$Na_2O + CO_2 = Na_2CO_3$	71.01	-284.707	4.586	-282.372	-231.900	-322.153	-277.155
$K_2O + CO_2 = K_2CO_3$	46.72	-363.424	5.873	-359.308	-309.498	-394.785	-349.084
$2LiOH + CO_2 = Li_2CO_3 + H_2O(g)$	91.88	-76.659	0.348	-72.423	-70.934	-94.567	-88.442
$2NaOH + CO_2 = Na_2CO_3 + H_2O(g)$	55.02	-108.606	-0.437	-108.216	-101.113	-127.510	-122.984
$2KOH + CO_2 = K_2CO_3 + H_2O(g)$	39.22	-136.699	3.151	-127.910	-130.836	-150.711	-141.079
$Li_2CO_3 + CO_2 + H_2O(g) = 2LiHCO_3$	59.56	-74.513	14.918	-65.508	30.287	-86.40[b]	-13.64[b]
$Na_2CO_3 + CO_2 + H_2O(g) = 2NaHCO_3$	41.52	-141.855	19.034	-127.683	-32.415	-135.341	-34.126
$K_2CO_3 + CO_2 + H_2O(g) = 2KHCO_3$	31.84	-154.428	18.293	-141.728	-46.281	-142.854	-44.716

[a] Calculated by the HSC Chemistry package[108].
[b] From Ref. 110.

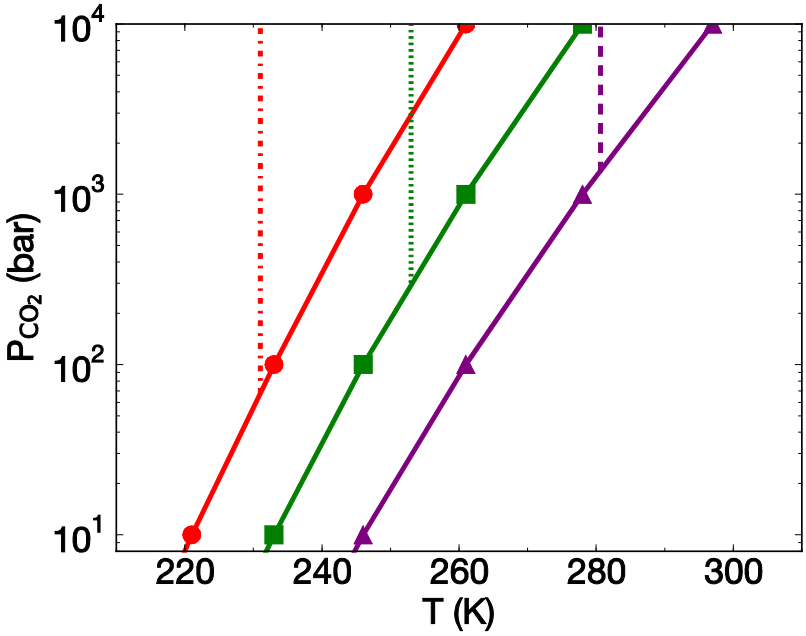

Figure 2.5. The $LiHCO_3$-Li_2CO_3 phase diagram at different partial pressures of H_2O. The bicarbonate phase is thermodynamically favored above the curves (at higher partial pressures of CO_2). The values of P_{H_2O} are 10^{-4}, 10^{-3}, and 10^{-2} bar for the circles, squares, and triangles, respectively. The red dashed dotted vertical line is the ice sublimation temperature at 10^{-4} bar. The green dotted vertical line is the ice sublimation temperature at 10^{-3} bar. The purple dashed vertical line is the water saturation temperature at 10^{-2} bar.

Thus, our calculations predict that $LiHCO_3$ should be observable at a temperature of 280 K when the pressure of CO_2 is above about 1000 bar and the pressure of water is at least 0.01 bar. The $LiHCO_3$ phase should also be stable at lower pressures of CO_2, but only at lower temperatures. Figure 2.5 provides guidance on the experimental conditions to explore in order to synthesize and characterize $LiHCO_3$.

Overall, from Figure 2.2-2.4 one can see that the $MHCO_3/M_2CO_3$ reactions for M=Na, K are in reasonably good agreement with the HSC data. However, we note that for other reactions our predictions are not always in good agreement with the HSC data. For the Li system (Figure 2.2) we note that the phase boundary from LiOH to Li_2O is predicted to occur at 850 K from the DFT calculations and 1340 K from HSC data. Note, however, that the JANAF tables indicate that the phase transition occurs somewhere between 900 and 1000 K. For the Na system (Figure 2.3) our DFT calculations overestimate the pressure for the $NaOH/Na_2CO_3$ reaction at low temperatures and underestimate the pressure for T > 850 K. Our DFT data predict that the Na_2O/Na_2CO_3 reaction will occur for T > 1250 K, whereas both HSC and JANAF data indicate that NaOH is still the lowest energy phase up to temperatures of 1500 K. Overall, our DFT calculations are in better agreement with the JANAF data than the HSC data for both Li and Na. Note that the HSC and JANAF data are generally in good agreement for T < 800 K for both Li and K systems. However, for the Na system there is disagreement between HSC and JANAF data, even at T = 700 K. One possible reason for this discrepancy may be due to differences in the melting points of the materials. We give the experimentally reported melting temperatures of the compounds of interest in this work in Table 2.3. We note from this table that the discrepancy between the HSC and JANAF data roughly correlates with the melting points of the hydroxides. Agreement between HSC and JANAF data for Li and K systems are best below or near the

melting points of the hydroxides. NaOH has a very low melting point and gives largest deviation between the JANAF and HSC data. The JANAF data are based on an extrapolation of the solid phase data, since we exclusively used the tables labeled “crystal” in the JANAF tables. This explains the better agreement between our DFT and the JANAF data, since our calculations are based on the assumption that all materials are perfect crystalline solids, except for CO_2 and H_2O. We note that the good agreement between our DFT calculations and HSC data seen for the $MHCO_3/M_2CO_3$ reactions may be fortuitous. We see from Table 2.3 that the melting points for the bicarbonates are both below 400 K, so that the bicarbonates would be in the liquid phase for almost the entire range covered in Figure 2.2(b), Figure 2.3(b), and Figure 2.4(b).

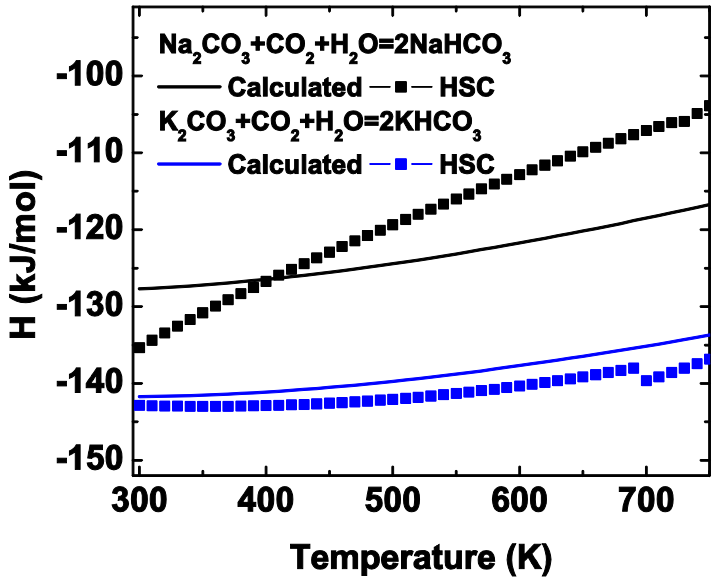

Figure 2.6. The calculated heats of reaction as a function of temperature for the carbonate/bicarbonate reactions computed from density functional theory compared with data from the HSC Chemistry package.

We have explored the origin of the error in our calculations and have found that the heats of formation for many of the compounds we have studied in this work are not in good agreement with experimental data. Figure 2.7 presents a comparison of our calculated heats of formation

with available experimental data. We see that the error in the DFT calculated heats of formation are very large for the carbonates, being greater than 90 kJ/mol. Note that the bicarbonates also have large errors of about 70 kJ/mol. One reason that the carbonate/bicarbonate reactions are in good agreement with the HSC data is that the total error for the carbonate/bicarbonate reactions are small due to a cancellation of errors. Hence the total errors in the net heats of formation for the $MHCO_3/M_2CO_3$ reactions are about -7 and 3 kJ/mol, for M=Na, K, respectively. In contrast, the errors in the heats of formation for the hydroxide/carbonate reactions are on the order of -20 kJ/mol for all three systems.

Table 2.3. Experimental melting points[107] (m. p.) of all available oxides, hydroxides, carbonates and bicarbonates studied in this work.

Compound	m. p. (K)
Li_2O	1843
Na_2O	1405.2
K_2O	623
LiOH	744.3
NaOH	596
KOH	679
Li_2CO_3	993.15
Na_2CO_3	1123.15
K_2CO_3	1174
$NaHCO_3$	~323
$KHCO_3$	~373

We have used the experimental heats of formation along with the DFT calculated finite temperature thermodynamics (zero point energies, entropies, heat capacities) in order to construct the convex hull reaction plots shown in Figure 2.2-2.4. The results for the Li-C-O-H system are shown in Figure 2.8 along with the HSC and JANAF data. The other two systems are not shown for brevity. The carbonate/bicarbonate reactions for the Na and K systems (not shown) were only marginally affected by using the experimental heats of reaction, in agreement with the cancellation of errors noted previously. The agreement between the DFT predicted

values and the HSC/JANAF data for the Li system is improved when using the experimental heats of formation, as can be seen from Figure 2.8. Similar results are seen for the Na system. However, the K-C-O-H system (not shown) is not substantially improved by using the experimental heats of formation.

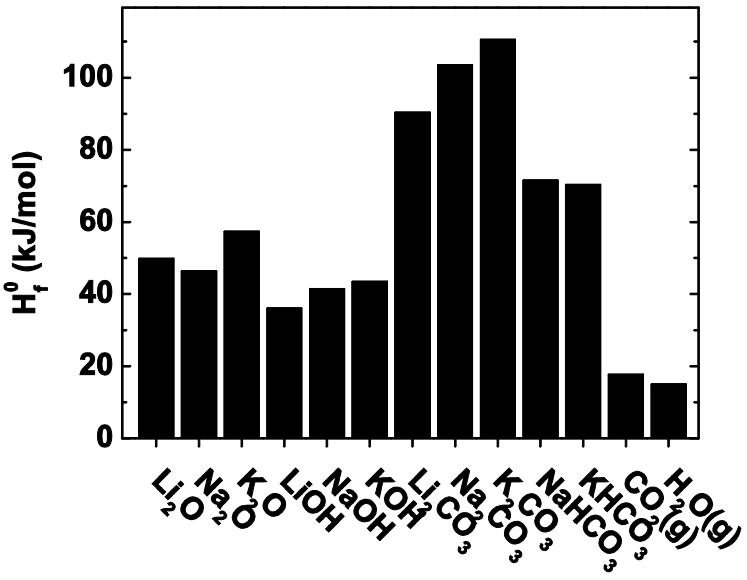

Figure 2.7. The relative errors in the calculated heats of formation for compounds studied in this work. We define the relative errors as $\Delta\Delta H_f^0 = \Delta H_f^0(\text{Experimental})\text{-}\Delta H_f^0(\text{DFT})$.

The problem with the K-C-O-H system appears to stem from two issues with the KOH solid phase. Firstly, the crystal structure reported is lacking positions for the H atoms, so we used reasonable guesses for the positions and relaxed the structure to a local ground state. Thus, the structure we used in our calculations may not be the correct ground state structure, although we believe it to be close to the ideal ground state structure. Secondly, and related to the first point, the reason for the lack of H atom positions in the structure is that KOH does not have well defined H atom positions at room temperature because of excessive librational motion of the OH

groups in the solid.[111] This means that our ideal solid calculations, which has all H atoms fixed at crystallographic positions, significantly underestimates the entropy of KOH. We notice the entropy for KOH is underestimated by about 20 J/mol/K at 300 K. At higher temperatures we expect the discrepancy to be even larger. In order to investigate the entropic effects due to disorder of the hydrogen atoms we have performed first principles molecular dynamics calculations using the VASP program within a constant temperature ensemble with a set-point temperature of 300 K. We observed a great deal of motion of the H atoms in the system over a time span on the order of 5 ps. This is in qualitative agreement with the experimental claim of OH librational motion at room temperature. We also noted a fair amount of motion of the K cation in the simulation, leading to additional disorder that exacerbates the error in computing the entropy of KOH using a perfect crystal. The underestimation of the KOH entropy appears to be the greatest source of error in the K-C-O-H system, because a comparison of the calculated entropy with tabulated entropy for all MOH (M=Li, Na, K) as a function of temperature shows that the KOH system has much larger errors than either of the other two systems.

In general, errors between the HSC and DFT values persist even when using the experimental heats of formation due to the following assumptions made in our calculations: (1) We assume perfect crystals, whereas at high temperatures the experimental systems may consist of defective crystals or even liquids. (2) We assume that each of the solid compounds remains in its low temperature crystal structure. *i.e.,* we do not account for solid-solid phase transitions for the pure compounds and for lattice expansions with increasing temperature. (3) We use the harmonic approximation to compute the phonon dispersion relations. At high temperatures anharmonic effects will be increasingly important. For liquids the phonon dispersion relations are not valid. Hence, our DFT calculations should be best at lower temperatures, and this is

confirmed by the generally good agreement between the pseudoexperimental data and our calculations at low temperatures.

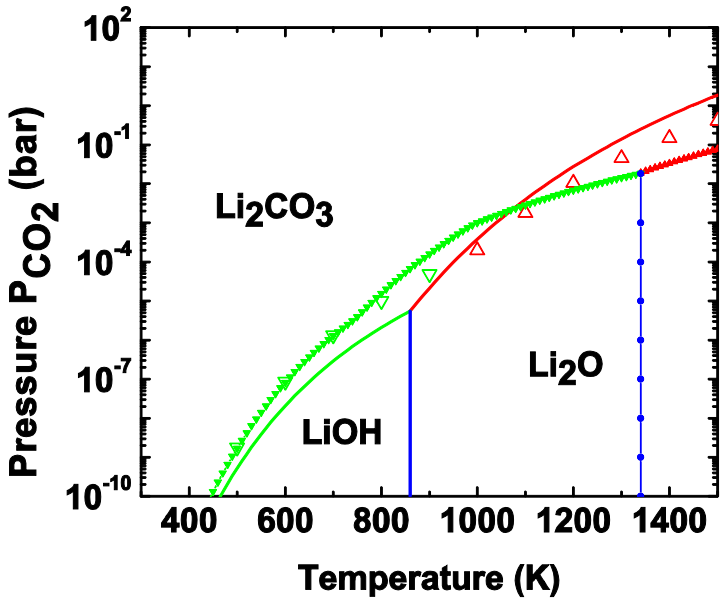

Figure 2.8. Phase diagrams computed from DFT but using the experimental heats of formations (solid lines) compared with data from HSC database (solid lines, filled symbols) and JANAF tables (open symbols). Phases are labeled according to our DFT results, boundaries are colored. Red: $Li_2O + CO_2 \rightleftharpoons Li_2CO_3$; Green: $2LiOH + CO_2 \rightleftharpoons Li_2CO_3 + H_2O$; Blue: $Li_2O + H_2O \rightleftharpoons 2LiOH$.

2.3.3 Application to pre- and post-combustion CO_2 capture technologies

In this section we consider how our predictions can be used to identify reactions appropriate for capturing CO_2 from pre- and post-combustion streams. Under pre-combustion conditions, after application of the water-gas shift reaction, a fuel gas stream mainly contains CO_2, H_2O and H_2. The partial CO_2 pressure is around 20~25 bar and the temperature is around 573~623K. To minimize the energy consumption, an ideal sorbent should work at these pressure and temperature ranges to separate CO_2 from H_2. We define a turnover temperature as the

temperature above which the computed pressure of CO_2 exceeds that in the gas phase from which CO_2 is to be captured. For example, for a gas containing 20 bar pressure of CO_2 the turnover temperature would be the temperature at which the reactants and products are in equilibrium with a gas having a CO_2 partial pressure of 20 bar. We have estimated the turnover temperatures for pre-combustion conditions of these nine reactions from Figure 2.2-2.4. These temperatures, denoted as T1, are listed in Table 2.4. For post-combustion conditions, the gas stream mainly contains CO_2 and N_2, the partial pressure of CO_2 is around 0.1~0.2 bar, and the temperature range is quite bit lower (<473K). From Figure 2.2-2.4, we have also obtained the turnover temperatures for post-combustion capture and the corresponding values, denoted as T2, are also presented in Table 2.4. Note that the partial pressure of H_2O in Figure 2.4 is too high to be appropriate for post-combustion conditions. However, the effect of the partial pressure of water in going from 0.1 to 1 bar on the phase diagram is relatively small.

Table 2.4. The highest temperatures for sorbents capturing CO_2 at pre-combustion (T_1) (P_{CO_2} =20 bar) and post-combustion (T_2) (P_{CO_2} =0.1 bar) conditions. For reactions involving H_2O, P_{H_2O} =1 bar.

Reactions	Pre-combustion T_1 (K)	Post-combustion T_2 (K)
$Li_2O + CO_2 = Li_2CO_3$	hT[a]	1290
$Na_2O + CO_2 = Na_2CO_3$	hT	hT
$K_2O + CO_2 = K_2CO_3$	hT	hT
$2LiOH + CO_2 = Li_2CO_3 + H_2O(g)$	hT	hT
$2NaOH + CO_2 = Na_2CO_3 + H_2O(g)$	hT	hT
$2KOH + CO_2 = K_2CO_3 + H_2O(g)$	hT	hT
$Li_2CO_3 + CO_2 + H_2O(g) = 2LiHCO_3$	<300	<300
$Na_2CO_3 + CO_2 + H_2O(g) = 2NaHCO_3$	440	380
$K_2CO_3 + CO_2 + H_2O(g) = 2KHCO_3$	490	420

[a] hT means the maximum temperature exceeds our temperature range (1500K).

From Figure 2.2-2.4 and Table 2.4, we see that all of the alkali oxides and hydroxides only can absorb CO_2 at very low CO_2 pressure and high temperature ranges which are far away

from the pre- and post-combustion conditions. Therefore, none of these materials are good candidates for CO_2 sorbents. As one can see, the turnover temperature of the $Li_2CO_3/LiHCO_3$ system is lower than room temperature; therefore, it cannot be used in practical CO_2 capture technologies. However, the $Na_2CO_3/NaHCO_3$and $K_2CO_3/KHCO_3$ reaction systems are very good candidates for CO_2 sorbents because these materials have favorable turnover temperatures for both of pre- and post-combustion conditions. In fact, alkali carbonates are widely used for CO_2 capture either in aqueous or dry conditions.[112, 113] The major advantage of carbonates/bicarbonates sorbents over amine-based sorbents is the significantly lower energy required for regeneration.[2, 82]

2.4 CONCLUSION

We have used first-principles density functional theory combined with phonon density of states calculations to obtain the phase diagrams of multi-component alkali metal M-C-O-H (M=Li, Na, K) systems. We have applied a linear programming method to compute the convex hull reactions for these systems and used the resulting data to estimate the thermodynamics of CO_2 capture reactions involving alkali metal oxides, hydroxides and carbonates/bicarbonates. We have compared our calculations with pseudoexperimental data from both the HSC chemistry package and the JANAF tables. Our calculated data are seen to be in qualitative, and in some cases quantitative agreement with the HSC/JANAF data. Hence, in a purely predictive mode, DFT calculations may be used as a rough screening step to identify materials for CO_2 capture. The discrepancies between the DFT and pseudoexperimental data are likely due to four factors: (1) Errors in the calculated heats of formation of the compounds. (2) The assumption that the solids

consist of perfect crystals throughout the temperature range. (3) The assumption that no solid-solid phase transitions take place for the pure solids (*i.e.*, we use only one crystal structure for each of the distinct compounds). (4) The use of the harmonic approximation to compute the phonon dispersion relations for the crystals.

The calculated bulk properties of M-C-O-H systems, including the bulk moduli, cohesive energies and optimized lattice constants, are in good agreement with the available experimental measurements and other theoretical findings. We have also identified the thermodynamic conditions (partial pressures of CO_2 and H_2O and temperatures) where $LiHCO_3$ is expected to be thermodynamically favored relative to Li_2CO_3, and could therefore be observed experimentally for the first time.

From the calculated phase diagrams of M-C-O-H (M=Li, Na, K) systems, we found that their oxides and hydroxides are not good candidates for CO_2 sorbents because the regenerating cycles only can occur at very low pressure or very high temperature. We predict that Na_2CO_3 and K_2CO_3 have turnover temperatures for CO_2 capture through bicarbonate formation that are suitable for operation under both pre- and post-combustion conditions.

3.0 DENSITY FUNCTIONAL THEORY STUDY OF CO_2 CAPTURE WITH TRANSITION METAL OXIDES AND HYDROXIDES

The Content of this chapter is taken from Bo Zhang, Yuhua Duan, and Karl Johnson, "Density functional theory study of CO_2 capture with transition metal oxides and hydroxides", Journal Chemical Physics, 136, 064516 (2012).

The author did all the calculations excluding all HSC calculations, which were performed by Yuahu Duan. The author wrote the major portion of the manuscript.

3.1 INTRODUCTION

The current interest in CO_2 capture and sequestration stems from it being one of the primary greenhouse gases and the evidence indicating that CO_2 plays a major role in global climate change. Annual anthropogenic CO_2 emissions are dominated by fossil energy use (approximate 85%).[1] Coal is responsible for about 25% of the energy production, primarily in power plants.[1] Moreover, many more coal-fired power plants are expected to be constructed over the next few decades in order to meet the increasing demand for electricity.[1] It is therefore critical to be able to capture and sequester CO_2 from existing and future coal-fired power plants in order to mitigate climate change. The U.S. Department of Energy has established targets for carbon capture and sequestration of removing 90% of the CO_2 with a concomitant increase in the cost of

electricity of no more than 35% in post-combustion and oxy-combustion capture technologies and less than 10% in pre-combustion capture technology.[2] In general, there are three classes of CO_2 capture technologies: pre-combustion capture, post-combustion capture, and oxy-fuel combustion. The concentration of CO_2 in flue gas (post-combustion) is 10–15 vol. % at atmospheric pressure for a typical coal fired power plant.[2] In post-combustion capture, CO_2 is extracted from the flue gas by various sorbents, either physically or chemically. Chemisorption (scrubbing) with aqueous monoethanolamine (MEA) is an example of a commercially available technique that is able to capture 90% of the CO_2 from flue gas.[2, 114] However, this technology suffers from solvent degradation[115, 116] and high energy costs[117] to regenerate the solvent. For pre-combustion, CO_2 is mixed with syngas, which is produced from the reaction between pure oxygen mixed with recycled flue gas or steam with fuel.[2] In this situation, the partial pressure of CO_2 is very high (about 20~25 bar) at relatively high temperature before coming into the turbine. Oxy-fuel combustion utilizes pure oxygen as oxidant instead of traditional air to avoid NO_x and to concentrate CO_2 for ready capture.[2]

In addition to the commercially available MEA scrubbing technology, various solid sorbents have been developed to capture CO_2 at potentially lower cost. There are basically two types of solid sorbents being considered, physical adsorbents and chemical absorbents. The physical adsorbent mainly utilizes its physical adsorption ability to capture CO_2 at relatively low temperature. Zeolites, metal organic frameworks, and activated carbon are the most widely studied physical sorbents for CO_2 capture.[118-122] These materials have some attractive properties such as high specific area, low cost, low regeneration energy, etc. However, water vapor in the gas feed often has a negative impact[123, 124] due to competitive adsorption between water vapor and CO_2. Chemical absorbents consist of metal oxides, hydroxides, carbonates and hydrotalcites.

Li_2O,[15, 21] Rb_2O,[125] Cs_2O,[126] CaO,[86, 127] MgO,[19, 86] BaO,[128, 129] CuO,[130] Al_2O_3,[131-133] Fe_2O_3,[133] Cr_2O_3,[134, 135] NaOH,[16, 136] Li_2ZrO_3,[137-139] Na_2ZrO_3,[140] $Mg(OH)_2$,[141] Na_2CO_3,[17] and K_2CO_3[18, 82, 142] are currently the most studied solid sorbents for CO_2 capture. However, those sorbents are still in the developmental phase and not yet commercialized on a large-scale.[2] The general formula of hydrotalcites can be expressed as $\left[M_{1-x}^{2+}M_x^{3+}\left(OH\right)_2\right]^{x+}\left(A_{x/m}^{m-}\cdot nH_2O\right)^{x-}$, where M^{2+} = Mg^{2+}, Ni^{2+}, Zn^{2+}, Cu^{2+}, Mn^{2+} etc., M^{3+} = Al^{3+}, Fe^{3+}, Cr^{3+} etc., A^{m-} = CO_3^{2-}, SO_4^{2-}, NO_3^-, Cl^-, OH^- etc., x is normally between 0.17 and 0.33.[143] Although these hydrotalcites have favorable specific surface area, they are not very stable at high temperature[144] due to structure evolution and generally have lower CO_2 capture capacity[143] compared with other metal compounds. On the other hand, transition metal compounds have drawn little attention either experimentally or theoretically in direct CO_2 capture. Manganese[145, 146] and nickel[79, 146] oxides are usually used as oxygen carriers in chemical looping combustion to generate pure CO_2 because they have high oxygen capacity and high thermal stability. Feng *et al.* studied the thermodynamics of MnO, ZnO reacting with CO_2 by using FactSage, which is a commercial thermodynamic modeling software package.[86] They also conducted thermogravimetric analysis experiments of absorption of CO_2. They concluded that MnO had a high regeneration temperature, which is desirable for fuel gas applications.

Use of computational thermodynamics modeling, as typified by the CALPHAD approach, is a powerful tool for screening possible sorbents for CO_2 capture. The drawback of this method is that thermodynamic data for all components must be available as a function of the state variables. In cases where thermodynamic data are missing it is possible to generate data from first-principles electronic structure methods to fill in missing data for use in CALPHAD calculations.[147, 148] Alternately, one may also screen materials based entirely upon first-principles

density functional theory (DFT) calculations, as has been demonstrated for complex hydride systems.[22, 149] A similar approach has been taken by Duan and coworkers for screening CO_2 capture with group 1 and 2 metal oxides and hydroxides.[21, 83] However, the accuracy of first-principles thermodynamics calculations for these materials appears to be significantly worse (about 20 kJ/mol difference[150]) than for similar calculations on complex metal hydrides (about 10 kJ/mol difference[149]). The reason for the observed decrease in accuracy has been traced primarily to inaccuracies in the DFT predictions of the reaction enthalpies.[150] The aim of this chapter is to assess the accuracy of five different DFT generalized gradient functionals for the prediction of the reaction thermodynamics of various transition metal oxides and hydroxides. In the process, we also screen these materials for suitability in pre-combustion and post-combustion CO_2 capture. Finally, we will test the capture suitability of studied sorbents through a theoretically rigorous linear programming method, to identify all the CO_2 thermodynamically favorable (convex hull) capture reactions as a function of temperature and partial pressures of CO_2 and H_2O.

3.2 COMPUTATIONAL DETAILS AND METHODOLOGY

3.2.1 Computational details

The crystal structures of solid compounds studied in this work were selected from the inorganic crystal structure database (ICSD).[88] We have chosen to use the structure with the lowest energy, as computed from DFT at zero temperature, when more than one structure is reported for a given compound.

Many calculations in this work were performed with the Vienna *ab-initio* simulation package (VASP),[90-93] which is a periodic plane-wave DFT code. Core-electron interactions were described by projector augmented-wave (PAW) potentials.[94, 95] We used two different generalized gradient approximation (GGA) exchange-correlation functional in our VASP calculations, particularly, PW91 of Perdew and Wang[96, 97] and PBEsol of Perdew *et al.*[151, 152] A plane-wave basis cutoff energy of 520 eV was used for all calculations. The k-point meshes were generated using the Monkhorst-Pack method[98] with a spacing of around 0.027 $Å^{-1}$ between k-points along the axes of the reciprocal unit cells.[21] We performed geometry relaxation of all atomic positions, cell shape, and cell volume using a stopping criterion of energy less than 0.01 meV. The conjugate gradient algorithm was used in conjunction with the PW91 functional, whereas the quasi-Newton algorithm was with the PBEsol functional because of numerical difficulties with the conjugate gradient method. Spin polarized calculations were performed for systems containing Mn and Ni.

We also performed calculations with the Grid-Based Projector-Augmented Wave (GPAW) code[153] using the following fucntionals: PBE of Perdew, Burke and Ernzerhof,[28, 29] TPSS of Tao, Perdew, Staroverov and Scuseria,[154] and revTPSS of Perdew *et al.*[155] The latter two functionals are meta-GGA functionals, which utilize non-local kinetic energy density for the occupied Kohn-Sham orbitals to better describe the exchange-correlation energy. In contrast, the PW91, PBE, and PBEsol functionals do not include the kinetic energy density. Thus, it might be expected that the TPSS and revTPSS functionals would be more accurate than the standard GGA functionals.[154, 155] For comparison purposes, we used the experimental lattice constants in our calculations. The meta-GGA calculations were performed using standard GPAW PBE pseudopotentials. The energies were converged to less than 10^{-6} eV/atom using a grid spacing of

0.15 Å. For some systems that are hard to converge with TPSS or revTPSS functionals, we have increased the threshold for the integrated value of the square of the residuals of the Kohn-Sham equations to 10^{-6}, where the default was 10^{-9}. The k-point meshes were the same as used in the VASP calculations. Spin polarized calculations were also performed for systems containing Mn and Ni. We used all five functionals to calculate the ground state energies of all the solid phase and gas phase compounds.

Phonon dispersion calculations and their contribution to the free energy were obtained using the frozen-phonon technique.[156] These calculations were done in VASP with the PW91 exchange-correlation functional. The energy cutoff is the same as listed above for our total energy calculations except the structures were relaxed until the forces were less than 0.1 meV/Å. Each symmetry-nonequivalent atom was displaced along all symmetry nonequivalent directions by 0.01 ~ 0.05 Å and forces on all atoms were calculated to construct the dynamical matrix. It is necessary to use a relatively large supercell to avoid interactions between images of the displaced atom. We have also calculated the phonon related thermodynamic properties using the PBEsol functional at the identical conditions to those calculations with the PW91 functional via frozen-phonon in VASP for Zn system and found little difference between these two functionals. Since phonon calculations are very expensive, we will use the thermal properties calculated via the frozen-phonon approach with the PW91 functional throughout the remainder of this chapter.

3.2.2 Methodology

The temperature-dependent free energy of the solids can be expressed as

$$G = U + PV - TS \approx U_{\mathrm{DFT}} + F_{\mathrm{phonon}}, \tag{3.1}$$

where U_{DFT} is the electronic total energy of the material as computed by DFT (either using the PW91, PBE, PBEsol, TPSS, or the revTPSS functional), F_{phonon} is the temperature-dependent phonon free energy contribution obtained from the frozen phonon technique through DFT calculations with the PW91 functional.

We assume that the gas phase species can be treated as ideal gas, therefore, the temperature-related free energy of gas species can be written as

$$G^0 = U + PV - TS \approx U_{\mathrm{DFT}} + U_{\mathrm{ZPE}} + U_{\mathrm{trans+rot}}(T) + U_{\mathrm{vib}}(T) + PV - TS(T), \tag{3.2}$$

where U_{DFT} is the electronic total energy of the material as computed using DFT (either PW91 or PBEsol functional), U_{ZPE} is the zero point energy (ZPE) of the gas. We use the statistical mechanical ideal gas expressions for the translational and internal energies of gas phase species. The translational and rotational contributions are

$$U_{\mathrm{trans+rot}} \cong \frac{5}{2}RT, \tag{3.3}$$

for linear molecules and non-linear molecule we use

$$U_{\mathrm{trans+rot}} \cong \frac{6}{2}RT. \tag{3.4}$$

The vibrational contributions to the energy are given by

$$U_{\mathrm{vib}} = \sum \frac{N_a h\nu}{\exp(h\nu / T) - 1} = \sum \frac{R\Theta}{\exp(\Theta / T) - 1}. \tag{3.5}$$

The temperature-dependent entropy is calculated from the Shomate equation from NIST chemistry webbook[100]

$$S = A\ln(t) + Bt + \frac{Ct^2}{2} + \frac{Dt^3}{3} - \frac{E}{2t^2} + F, \tag{3.6}$$

where

$$t = \frac{T}{1000}, \tag{3.7}$$

and *A*–*F* are system dependent constants. We use the ideal gas identity

$$PV = RT, \tag{3.8}$$

where *V* is the molar volume, in Eq. (3.8). Finally, we obtain the free energy expression for gas phase species for linear molecules as:

$$\begin{aligned} G \approx U_{\mathrm{DFT}} + U_{\mathrm{ZPE}} + \frac{7}{2}RT - T\left[A\ln(t) + Bt + \frac{Ct^2}{2} + \frac{Dt^3}{3} - \frac{E}{2t^2} + F \right] \\ + \sum \frac{R\Theta}{\exp(\Theta/T) - 1} + RT\ln\left(\frac{P}{P_0}\right), \end{aligned} \tag{3.9}$$

and for non-linear molecules:

$$\begin{aligned} G \approx U_{\mathrm{DFT}} + U_{\mathrm{ZPE}} + \frac{8}{2}RT - T\left[A\ln(t) + Bt + \frac{Ct^2}{2} + \frac{Dt^3}{3} - \frac{E}{2t^2} + F \right] \\ + \sum \frac{R\Theta}{\exp(\Theta/T) - 1} + RT\ln\left(\frac{P}{P_0}\right). \end{aligned} \tag{3.10}$$

Combining the free energies of solid and gas species according to the following reactions,

$$[\text{oxide}] + [CO_2] \rightleftharpoons [\text{carbonate}],$$

$$[\text{hydroxide}] + [CO_2] \rightleftharpoons [\text{carbonate}] + [H_2O].$$

We can obtain the free energy change of reaction as

$$\Delta G = \Delta G_{\mathrm{solid}} + \Delta G_{\mathrm{CO_2}}, \tag{3.11}$$

or

$$\Delta G = \Delta G_{\mathrm{solid}} + \Delta G_{\mathrm{CO_2}} - \Delta G_{\mathrm{H_2O}}, \tag{3.12}$$

where

$$\Delta G_{\mathrm{solid}} = G_{\mathrm{carbonate}} - G_{\mathrm{oxide}}, \tag{3.13}$$

or

$$\Delta G_{\text{solid}} = G_{\text{carbonate}} - G_{\text{hydroxide}} \tag{3.14}$$

for reactions without and with water, respectively.

Since the volume change due to gas generation is very large relative to the volume change of solid materials, we can neglect the volume change of solid phases without significant loss of accuracy. If the activities of all solid components are taken to be 1, the equilibrium pressure of the overall reaction can then be written as

$$\frac{P_{\text{CO}_2}}{P_0} = \exp\left(-\frac{\Delta G}{RT}\right), \tag{3.15}$$

where P_0 is the standard state pressure (1 bar), or

$$\frac{P_{\text{CO}_2}}{P_{\text{H}_2\text{O}}} = \exp\left(-\frac{\Delta G}{RT}\right), \tag{3.16}$$

for reactions without and with H_2O, respectively. Note that for reactions including both CO_2 and H_2O in the gas phase, the pressure term is actually the ratio of the partial pressure of CO_2 and H_2O. The van't Hoff plots are obtained by plotting the equilibrium pressures from Eqs. (3.15) or (3.16) as a function of the inverse absolute temperature.[149]

We used a linear programming method that has been described elsewhere[22] to determine the phase diagram. In brief, the grand-canonical Gibbs free energy of a system where all possible solid phases are in contact with a gas-phase reservoir having specified partial pressures of CO_2 and H_2O can be written as

$$G(T, \mu_{\text{gas}}) = \sum_{j=1}^{S} x^j F^j(T) - \sum_k \sum_{j=1}^{S} \mu_k^{\text{gas}}(T, p) x_k^{j,\text{gas}}, \tag{3.17}$$

where $F^j(T)$ is the free energy of solid phase j (ignoring the pV term contribution), S is the number of solid substances, $\mu_k^{\text{gas}}(T, p)$ is the chemical potential of gas species k (CO_2 and H_2O), x^j is the unknown mole fraction of phase j coexisting at a given composition, temperature, and

pressure. The mol fraction x^j is based on elements appearing only as solids (in this case only the metals). $x_k^{j,\text{gas}}$ is the theoretical mol fraction of gas species k contained in phase j. We scanned the temperature and pressure range of interest and computed the resulting chemical potentials of each gas species, using the values in Eq. (3.17) to map out the convex hull. We assume ideal mixing in order to compute the thermodynamic properties of all species.

The x^j mole fractions are determined by minimizing the grand-canonical Gibbs free energy, subject to the following mass-conservation constraints for the solid phase species

$$\sum_{i=\text{metal}}^{M} f_i = \sum_{i=\text{metal}}^{M} \sum_{j=1}^{S} x^{j,\text{solid}} b_i^{j,\text{solid}} = 1, \tag{3.18}$$

where f_i is the molar ratio of solid element i in all solids, represents the number of atoms of type i in one formula unit of phase j, and M is the number of elements. We can choose sufficiently small intervals of temperature and pressure to ensure adequately small chemical potential changes between two steps in order to guarantee single step reactions.

3.3 RESULTS AND DISCUSSTION

3.3.1 Lattice parameters from DFT calculations and Entropies from frozen-phonon calculations

The experimental and DFT (PW91 and PBEsol functional only) optimized lattice parameters for all solids included in this study are listed in Table 3.1, along with the enthalpies of formation and entropies from both experiments and DFT calculations. We also list experimental and calculated data for gas phase CO_2 and H_2O in Table 3.1. Generally good agreement can be observed

between DFT calculated and experimental lattice parameters; the overall errors are within 2% for both functionals tested. We note that the predicted lattice constants from the PBEsol functional are in better agreement with experiments than predictions from PW91 for compounds containing Zn and Cd, except for $Zn(OH)_2$. The average error is less than 0.5% from PBEsol, compared with about 1.7% using PW91. However, for compounds containing Mn and Ni, the average error is 2.9% using PBESol, compared with an average error of 1.1% using PW91. The lattice parameters of hydroxides show the biggest divergence among oxides, hydroxides, and carbonates when comparing both functionals, and the average errors are 1.4% and 3.9% for PW91 and PBEsol, respectively. For compounds that have multiple reported phases, the structures for the compounds listed in Table 3.1 were chosen because they have the lowest total energies from DFT calculation at 0 K. The exception is $Zn(OH)_2$, for which we have chosen the β phase, which is known to be the stable phase in experiments, although it has a slightly higher total energy than the γ phase. These structures may not be the most stable experimentally at the operating temperatures (450-600 K), and this could lead to some discrepancy between calculated and experimental thermodynamics. Identification of solid phase boundaries for multiple structures of the same compound is possible, but computationally prohibitive when the goal is to screen many different compounds.

Table 3.1. Summary of lattice parameters, enthalpies of formation, and entropies from experiments and DFT calculations with different functionals.

Compound	Space group	Lattice Parameters[a]			Enthalpy of Formation[b] (kJ/mol)			Entropy[c] (J/mol K)	
		Expt.	PW91	PBEsol	Expt.	PW91	PBEsol	Expt.	PW91
MnO	$Fm\bar{3}m$	a=4.446	a=4.3281	a=4.3367	-385.2	-246.1	-231.4	59.71	49.98
NiO	$Fm\bar{3}m$	a=4.1944	a=4.1809	a=4.1056	-239.7	-103.7	-108.2	37.99	53.75
ZnO	$P6_3mc$	a=3.2525 c=5.2111 γ=120	a=3.2806 c=5.2978 γ=120	a=3.2389 c=5.2276 γ=120	-350.5	-289.7	-288.4	43.64	45.31
CdO	$Fm\bar{3}m$	a=4.6948	a= 4.7758	a=4.7083	-258.4	-207.8	-211.4	54.81	60.21
$Mn(OH)_2$	$P\bar{3}m1$	a=3.322 c=4.734 γ=120	a=3.3496 c=4.7417 γ=120	a=3.2991 c=4.5419 γ=120	-695.4	-529.2	-522.7	99.2	86.15
$Ni(OH)_2$	$P\bar{3}m1$	a=3.13 c=4.63 γ=120	a=3.1665 c=4.5814 γ =120	a=3.1203 c=4.3581 γ=120	-529.7	-381.9	-397. 8	88	70.42
$Zn(OH)_2$	$P\bar{3}m1$	a=3.194 c=4.714 γ=120	a=3.2389 c=4.6598 γ=120	a=3.1901 c=4.4824 γ=120	-641.9	-540.6	-561.3	81.2	82.59
$Cd(OH)_2$	$I1m1$	a=5.688 b=10.28 c=3.42 β=91.4	a=5.7868 b=10.2725 c=3.4943 β=88.889	a=5.6959 b=10.0532 c=3.4321 β=88.548	-560.7	-497.4	-513.6	96	93.45
$MnCO_3$	$R\bar{3}cH$	a=4.772 c=15.637 γ =120	a=4.8098 c=15.7615 γ=120	a=4.7625 c=15.4107 γ=120	-894.1	-699.9	-694.0	85.8	87.71
$NiCO_3$	$R\bar{3}cH$	a=4.6117 c=14.735 γ=120	a=4.6338 c=14.8239 γ=120	a=4.6344 c=14.8197 γ=120	-703.4	-532.4	-551.2	85.4	72.99
$ZnCO_3$	$R\bar{3}cH$	a=4.6526 c=15.0257 γ=120	a=4.7144 c=15.1962 γ=120	a=4.6663 c=14.8792 γ=120	-812.8	-695.5	-717.9	82.4	85.32
$CdCO_3$	$R\bar{3}cH$	a=4.9207 c=16.2968 γ=120	a=5.0071 c=16.5684 γ=120	a=4.9614 c=16.1785 γ=120	-750.6	-665.5	-678.6	92.5	100.46
CO_2	$P1$		a=10 (fixed)		-393.5	-376.	-361.7	213.8	214.02
H_2O (g)	$P1$		a=10 (fixed)		-241.8	-227.2	-236.1	188.8	189.04

[a] All distances are in Å, and angles are in degrees. Experimental values are taken from ICSD database.[88]

[b] Enthalpy of formation is in kJ/mol. Experimental values are measured at 298.15 K. Most of the experimental values of solid compound are taken from Ref [107]. Experimental values for NiO and $Mn(OH)_2$ are taken from Ref [157]. Experimental values for $NiCO_3$ are taken from Ref [158]. Experimental entropies of CO_2 and gas H_2O are taken from Ref [100]. Entropies of CO_2 and gas H_2O are calculated from Shomate equation at 300K.

[c] Entropies are in J/(mol K). Experimental values are measured at 298.15 K, entropies from frozen phonon are calculated at 300 K. Most of the experimental values of solid compound are taken from Ref [107]. Experimental values for NiO and $Mn(OH)_2$ are taken from Ref [157]. Experimental values for $NiCO_3$ are taken from Ref [158]. Experimental entropies of CO_2 and gas H_2O are taken from Ref [100]. Entropies of CO_2 and gas H_2O are calculated from Shomate equation at 300K.

We note from Table 3.1 that entropies calculated from the frozen-phonon approach with the PW91 functional are generally in good agreement with the experimental data. Discrepancies are within 10 J/(mol K), except for NiO, $Ni(OH)_2$, $NiCO_3$, and $MnCO_3$. This indicates our frozen-phonon approach is capable of predicting reasonable thermodynamics associated with phonons for solid materials. With all the energy and entropy terms from Eqs. (3.1) and (3.2) in hand, we can apply Eqs. (3.15) and (3.16) to construct the van't Hoff plots, as discussed in the next section.

3.3.2 Thermodynamic properties for CO_2 capture reactions

Table 3.2 lists the room temperature reaction enthalpies computed from the five different DFT functionals and the entropies computed from the PW91 frozen phonon calculations for the reactions we studied. We also report data from experiments and from the HSC Chemistry[108] (HSC) approach. HSC Chemistry is a chemical reaction and equilibrium software package that can be used to calculate reaction equilibrium based on correlation of experimental data. The HSC chemistry package uses an equation to fit experimental heat capacity data for a very wide range of species. The resulting correlation is used along with experimental enthalpy and entropy data at 298.15 K to perform thermodynamic calculations. The HSC correlations are based on data collected from many different sources. Hence, the results from HSC chemistry calculations are not expected to agree exactly specific experimental data. We note generally good agreement between experiments and HSC in Table 3.2. Most of the differences between experiments and HSC are less than 2 kJ/mol, although the differences are a little larger for NiO, $Ni(OH)_2$, MnO, and $Mn(OH)_2$ carbonate reactions. The largest discrepancy of about 13 kJ/mol is observed for the $Mn(OH)_2$ carbonate reaction. We conclude that the data taken from HSC are generally reliable,

although discrepancies of about 10 kJ/mol may exist. On the other hand, there are relatively large differences between the calculated enthalpies of reaction at 298.15 K from all DFT methods and the experimentally measured values. The absolute mean relative errors are 49.7%, 31.8%, 16.3%, 111.5%, 171.6% for the PW91, PBE, PBEsol, TPSS, and revTPSS functional, respectively. The PBEsol functional performs much better on average than any of the other functionals tested for the enthalpy of reaction. We also note that the enthalpies of reaction computed from lattice dynamics are only weakly dependent on temperature in the range 0 to 298 K (not shown). The changes in the reaction enthalpies are less than 6 kJ/mol for oxides, and less than 2 kJ/mol for hydroxides over the temperature range from 0 to 298.15 K. This implies that one can reasonably use the zero Kelvin DFT enthalpies for fast screening of candidate materials, which gives a substantial savings in computer time, because the phonon calculations are very computationally expensive. The entropy changes of reactions from frozen phonon calculation are generally in good agreements with experimentally measured data for every reaction studied. The differences are usually less than 10 J/(mol K), except for those reactions involving compounds containing Mn or Ni, for which the errors are above 15 J/(mol K). However, our calculated reaction entropies lie in between the HSC values listed in Table 3.2 (in the parenthesis) and the experimental data for the Mn-containing reactions, indicating that the entropies from the phonon calculations are certainly reasonable, even for these reactions. The reaction entropies for oxide carbonate reactions are all very similar, being about 170±6 J/(mol K) on average, based on experimental values. In contrast, the reaction entropies for hydroxide carbonate reactions are about one order of magnitude smaller than for oxides, or about 20±2 J/(mol K) on average, based on experimental values. This is partly due to the hydroxides having significantly larger entropies than the oxides, as can be seen from Table 3.1.

Table 3.2. Summary of reaction thermodynamics. Enthalpies are in kJ/mol, entropies in J/(mol K).

Reaction	ΔH^0	ΔH_{PW91}	ΔH_{PBE}	ΔH_{PBEsol}	ΔH_{TPSS}	$\Delta H_{revTPSS}$	ΔH	ΔS^0	ΔS
	Expt.[a]	Calculated By DFT[b]					HSC[c]	Expt.[d]	Calc.[e]
$MnO+CO_2 \rightleftharpoons MnCO_3$	-115.4	-77.71	-70.27	-100.85	-95.35	-117.65	-102.77	-187.71 (-167.83)	-176.29
$NiO+CO_2 \rightleftharpoons NiCO_3$	-70.18	-52.57	-65.89	-81.27	-112.80	-141.90	-63.05	-166.39	-194.78
$ZnO+CO_2 \rightleftharpoons ZnCO_3$	-68.8	-29.63	-36.33	-67.83	-108.59	-147.30	-68.76	-175.04	-174.01
$CdO+CO_2 \rightleftharpoons CdCO_3$	-98.73	-81.5	-78.91	-105.47	-117.64	-138.89	-99.36	-176.11	-173.77
$Mn(OH)_2+CO_2 \rightleftharpoons MnCO_3+H_2O$	-47	-21.74	-16.98	-45.57	-55.70	-75.52	-33.88	-38.4 (-18.53)	-23.41
$Ni(OH)_2+CO_2 \rightleftharpoons NiCO_3+H_2O$	-21.98	-1.53	-22.26	-27.72	-91.57	-121.63	-14.92	-27.6	-22.4
$Zn(OH)_2+CO_2 \rightleftharpoons ZnCO_3+H_2O$	-19.2	-5.96	-17.88	-30.98	-90.23	-121.25	-19.18	-23.8	-22.24
$Cd(OH)_2+CO_2 \rightleftharpoons CdCO_3+H_2O$	-38.2	-19.11	-11.29	-39.36	-50.29	-64.39	-38.69	-28.5	-17.97

[a] All the experimental values are computed from data in Table 3.1 at 298.15 K.
[b] Enthalpies calculated with different functionals at 298.15 K including finite temperature phonon contributions.
[c] Values taken from HSC database, at 303.15 K.
[d] Experimental values are computed from data in Table 3.1, at 298.15 K; values in the parenthesis are taken from HSC database at 303.15K.
[e] Calculated with the PW91 functional via the frozen-phonon method at 300K.

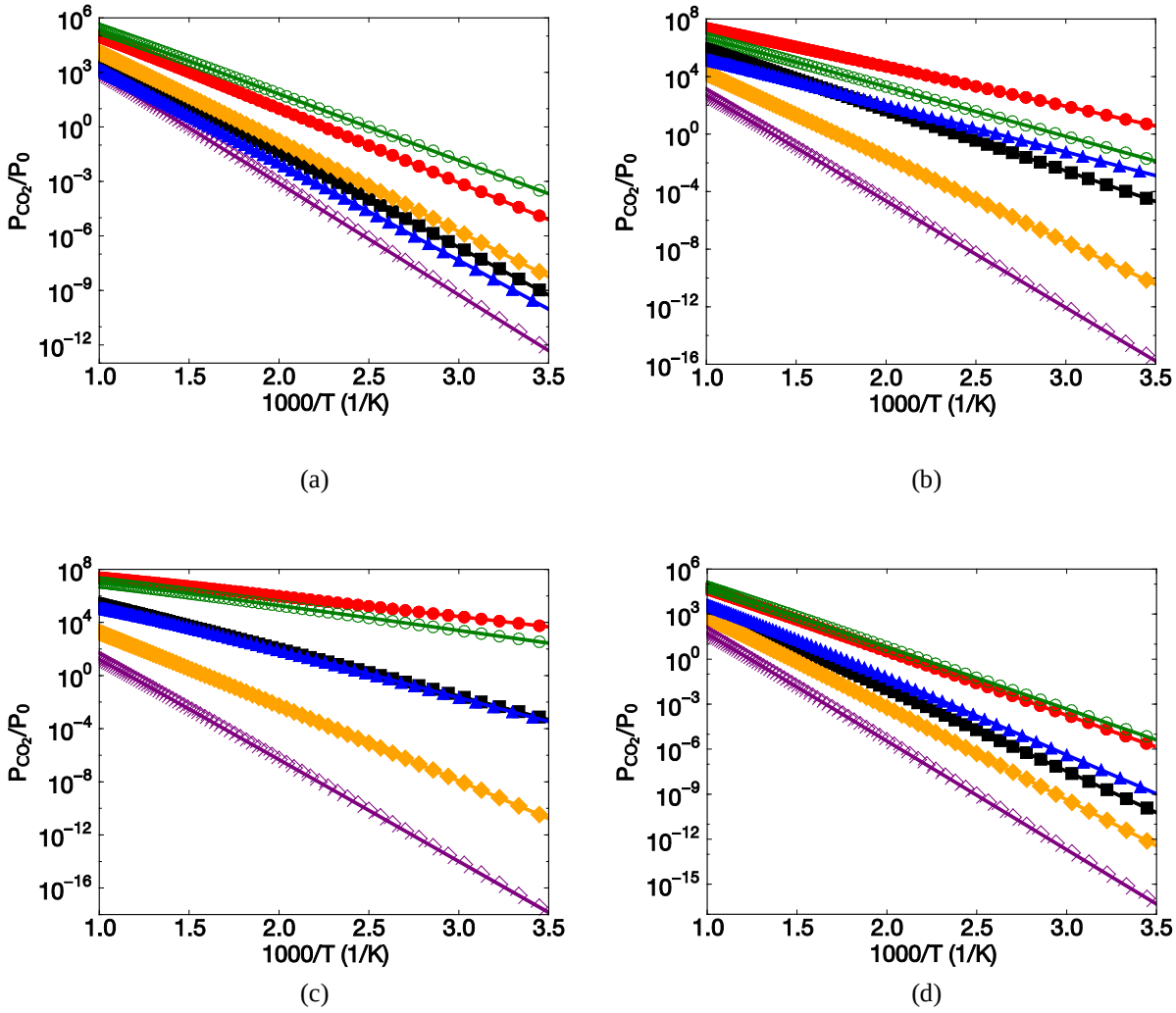

Figure 3.1. The calculated van't Hoff plots for reactions of oxides with CO_2. (a) MnO + CO_2 ⇌ $MnCO_3$; (b) NiO + CO_2 ⇌ $NiCO_3$; (c) ZnO + CO_2 ⇌ $ZnCO_3$; (d) CdO + CO_2 ⇌ $CdCO_3$. The HSC data are denoted by blue triangles, PW91 by the filled red circles, PBE by the open green circles, PBEsol by the filled black squares, TPSS by the filled yellow diamonds, and revTPSS by the open purple diamonds.

The van't Hoff plots for systems containing MnO, NiO, ZnO, and CdO computed from six different methods are given in Figure 3.1(a)-(d). The first method uses PW91 DFT total energies with inclusion of finite-temperature effects, which are due to phonon contribution of solids plus the free energy of gas phase species, CO_2 in this case. The next four methods are identical to the first method, except that the PW91 DFT energies are replaced by total energies computed using the PBE, PBEsol, TPSS, and the revTPSS functionals. The last method uses the

HSC package[108] to compute the van't Hoff plots. We consider the HSC calculations to be pseudo-experimental data based on agreement between experiments and HSC data reported in Table 3.2. As can be seen from Figure 3.1, the slopes from the van't Hoff plots constructed with the PW91 and PBE functional agree with those from HSC, however, the CO_2 pressure is dramatically overestimated. There is very little difference between the plots constructed by these two functionals. In contrast, the curves computed using the TPSS and revTPSS functionals tend to underestimate the partial pressure of CO_2, with the exception of MnO, and CdO, where curves based on the TPSS functional are much closer to the HSC curves than for the other two systems. Overall, the curves computed from the PBEsol functional are in much better agreement with the HSC curves than data from the other functionals. This is especially true for ZnO, where excellent agreement can be observed.

The van't Hoff plots for reactions involving $Mn(OH)_2$, $Ni(OH)_2$, $Zn(OH)_2$, and $Cd(OH)_2$ computed from the six different methods are plotted in Figure 3.2. The *y*-axis is the ratio of the partial pressures of CO_2 and H_2O as given in Eq. (3.16). The methods used here are the same as for the oxides. The PW91 and PBE functional calculations give slopes in agreement with those from the HSC calculations, but the pressure ratios are substantially overestimated, except for $Zn(OH)_2$ where the curve using the PBE functional is closer to the HSC data than any other functionals, as is the case for the oxides. Similarly, the curves based on the energies computed from TPSS and revTPSS functionals underestimate the pressure ratio drastically. However, contrary to the oxides, the PBEsol functional significantly underestimates the pressure ratios for all systems except $Cd(OH)_2$, where good agreement between PBEsol and HSC calculations is observed.

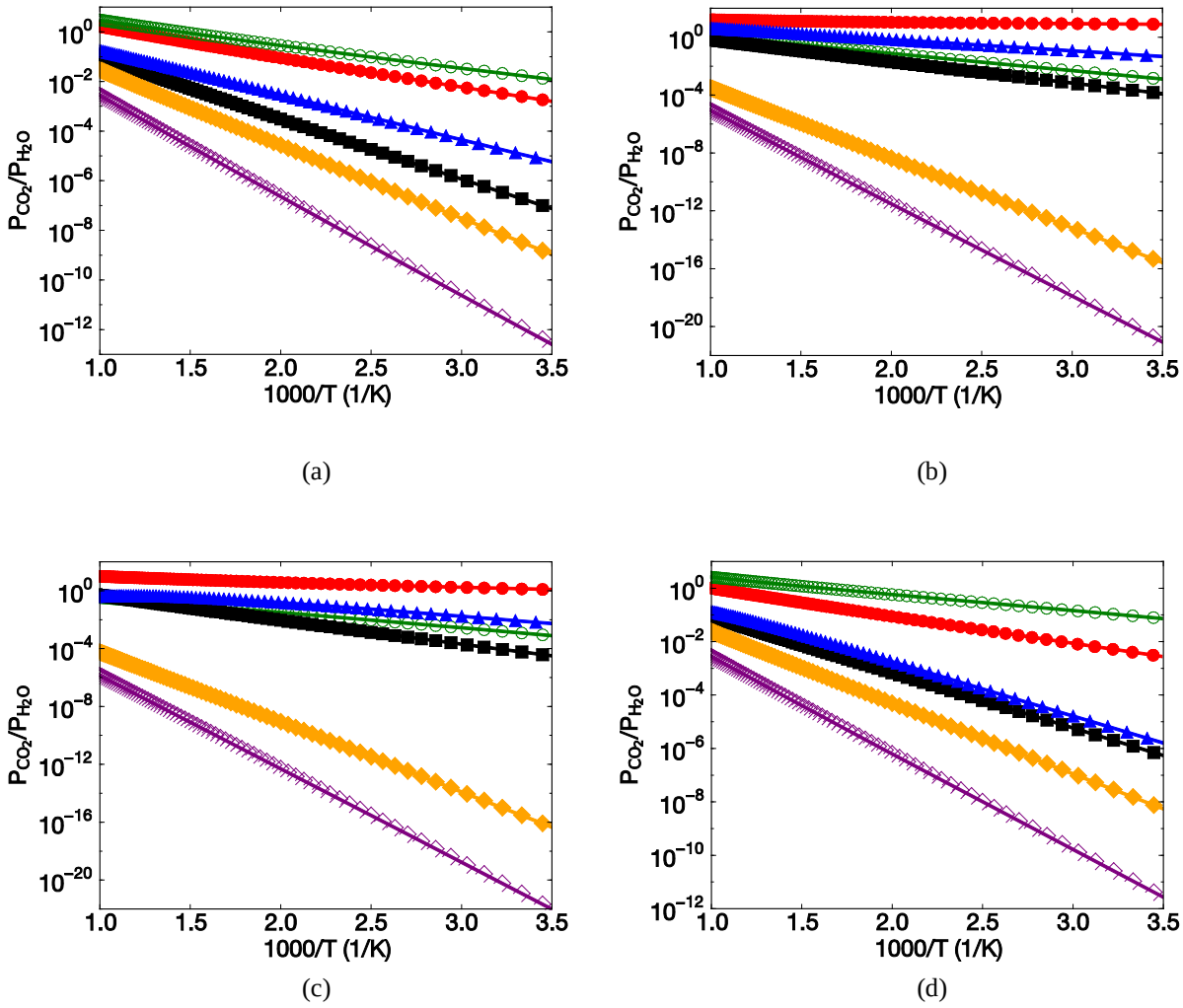

Figure 3.2. The calculated van't Hoff plots for reactions of the hydroxides with CO_2. (a) $Mn(OH)_2 + CO_2 \rightleftharpoons MnCO_3 + H_2O$; (b) $Ni(OH)_2 + CO_2 \rightleftharpoons NiCO_3 + H_2O$; (c) $Zn(OH)_2 + CO_2 \rightleftharpoons ZnCO_3 + H_2O$; (d) $Cd(OH)_2 + CO_2 \rightleftharpoons CdCO_3 + H_2O$. The HSC data are denoted by blue triangles, PW91 by the filled red circles, PBE by the open green circles, PBEsol by the filled black squares, TPSS by the filled yellow diamonds, and revTPSS by the open purple diamonds.

3.3.3 Errors in computed thermodynamics

As noted previously, the reaction thermodynamics computed from DFT methods are not always in good agreement with HSC data.[150] In this section we examine errors in the enthalpies of formation and the reaction enthalpies computed from different functionals. The differences

between the formation enthalpies ($\Delta\Delta H$) from DFT and experiments for all species of interest in this work are presented in Figure 3.3. It is striking that the DFT calculations result in very large errors in the formation enthalpies of the solid compounds compared with experiments, particularly for those systems containing Mn and Ni. On the other hand, the differences between calculations and experiments for gas phase species, CO_2, H_2O, are relatively small, but they are still too large to be considered to be within "chemical accuracy", which is about 4 kJ/mol. The mean relative errors in the formation enthalpies for gas phase H_2O and CO_2 are -5.23%, -6.20%, -5.22%, -9.57%, -13.94% for the PW91, PBE, PBEsol, TPSS, and revTPSS functionals, respectively. All the GGA level functionals perform with comparable accuracy for the gas phase species, which are slightly better than TPSS and revTPSS functionals, but as can be seen from Figure 3.3 and Table 3.3, the errors for the solids phase species are not uniform. Notably, the relative errors for oxides are larger than those for hydroxides and carbonates. The TPSS and revTPSS functionals are better at predicting the formation enthalpies for oxides and carbonates compared with the GGA functionals, while they are slightly worse for hydroxides and the gas phase species. All the GGA functionals have similar errors in calculating the enthalpies of formation. The PBEsol functional has the smallest errors for oxides, carbonates and gases compared with the other GGA functionals.

Table 3.3. Average percentage errors in the formation enthalpies for the systems in Figure 3.3, grouped by category.

	PW91	PBE	PBEsol	TPSS	revTPSS
Oxides	-32	-38	-33	-30	-31
Hydroxides	-20	-23	-18	-24	-27
Carbonates	-18	-19	-16	-11	-8
All solids	-23	-27	-22	-22	-22
Gases	-5	-6	-5	-10	-14

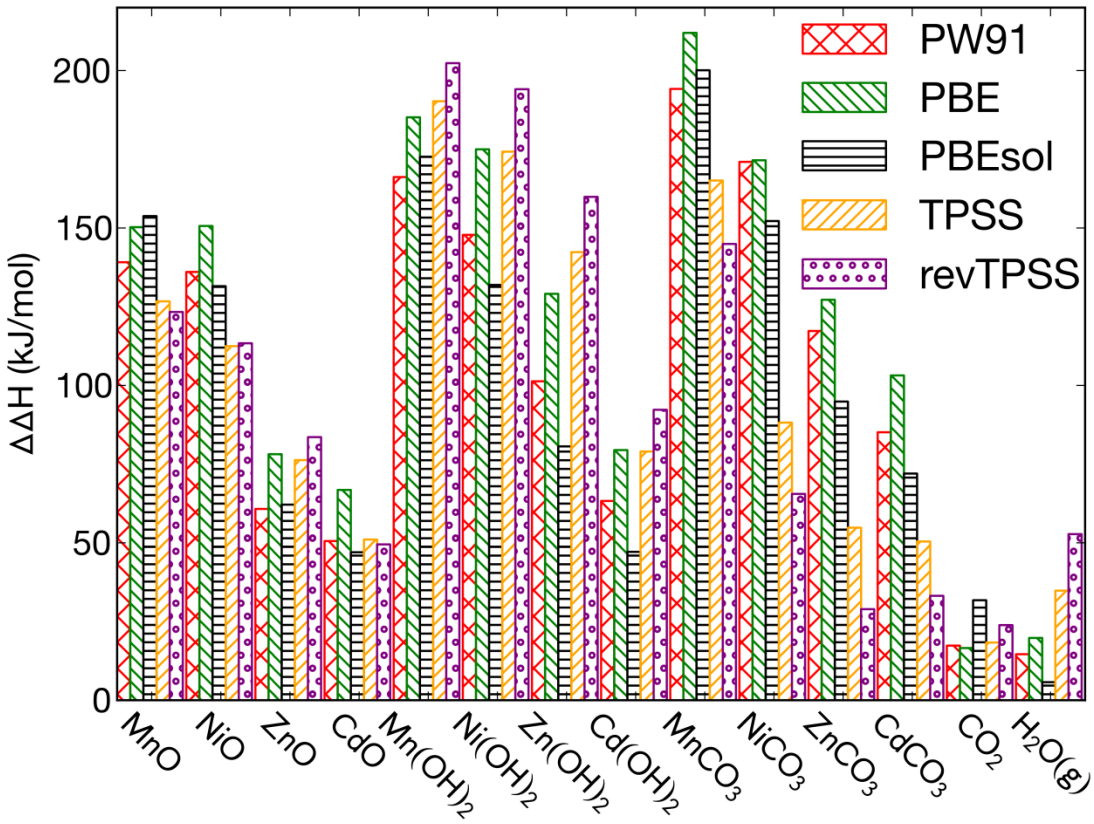

Figure 3.3. Differences between the calculated and experimental enthalpies of formation, defined as $\Delta\Delta H = \Delta H_{\text{DFT}} - \Delta H_{\text{expt}}$.

It has been previously shown that using experimental heat of formation along with the temperature-dependent phonon contribution from DFT calculations will give better agreement with experimental and HSC data than use of the total energies from the PW91 functional.[150] We here take the same approach as a test of the PBEsol functional. We have therefore computed the van't Hoff plots using experimental formation enthalpies in place of the DFT total energies in Eqs. (3.1) and (3.2). We compare these calculations with PBEsol results and HSC data in Figure 3.4(a)-(d) for the carbonate reactions involving MnO, NiO, ZnO, and CdO. We see from Figure 3.4 that the van't Hoff plots computed from PBEsol are about as accurate as those using

experimental heats of formation for these oxides. The agreement between our calculated values and the HSC data is very good for Zn and Cd, not quite as good for Mn, and significantly poorer for Ni.

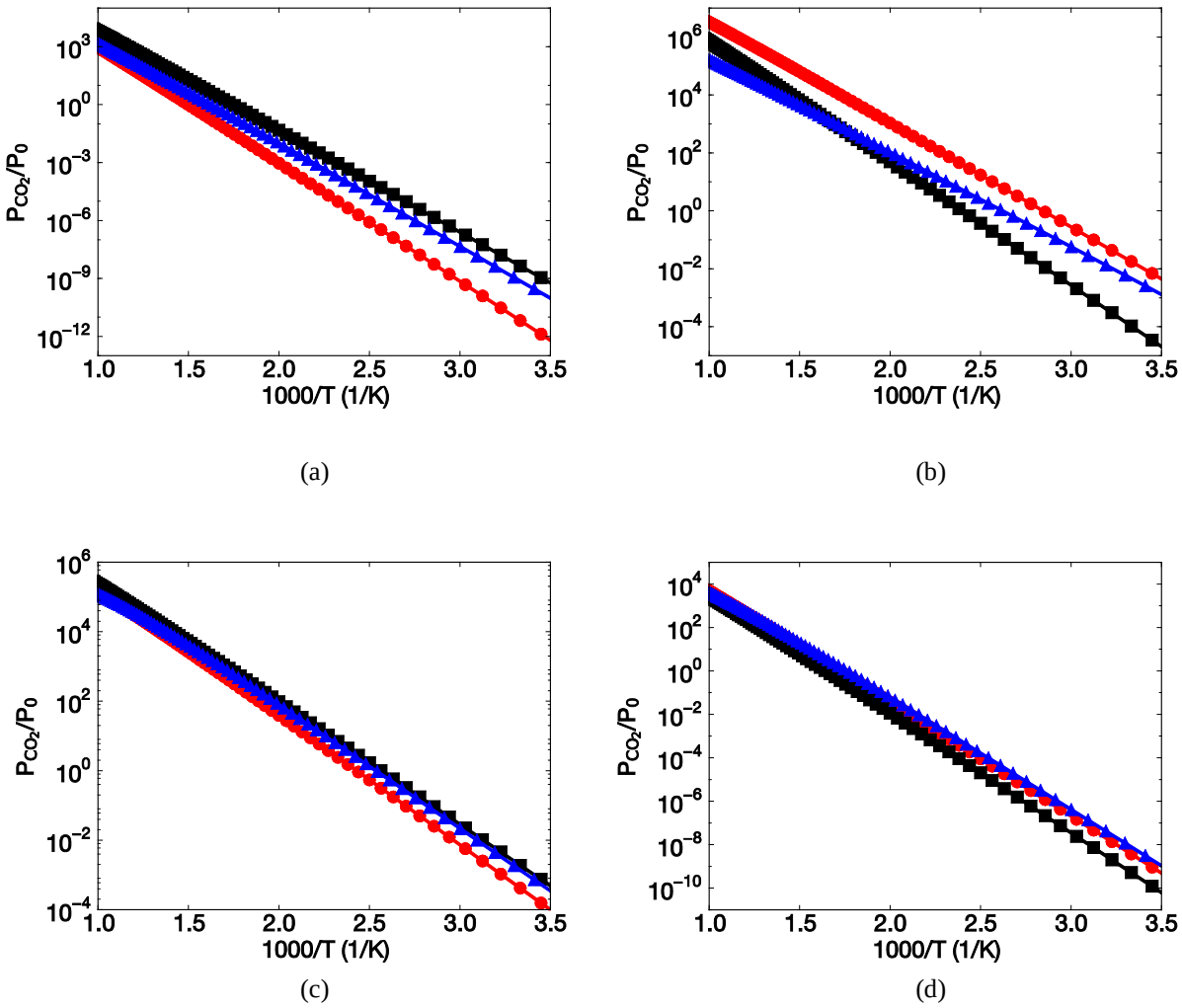

Figure 3.4. Comparison of van't Hoff plots for oxides reacting with CO_2 computed from HSC data (blue triangles), from PBEsol (black squares), and from experimental heats of reaction complemented with DFT (red circles, see text for details). (a) MnO + CO_2 ⇌ $MnCO_3$; (b) NiO + CO_2 ⇌ $NiCO_3$; (c) ZnO + CO_2 ⇌ $ZnCO_3$; (d) CdO + CO_2 ⇌ $CdCO_3$.

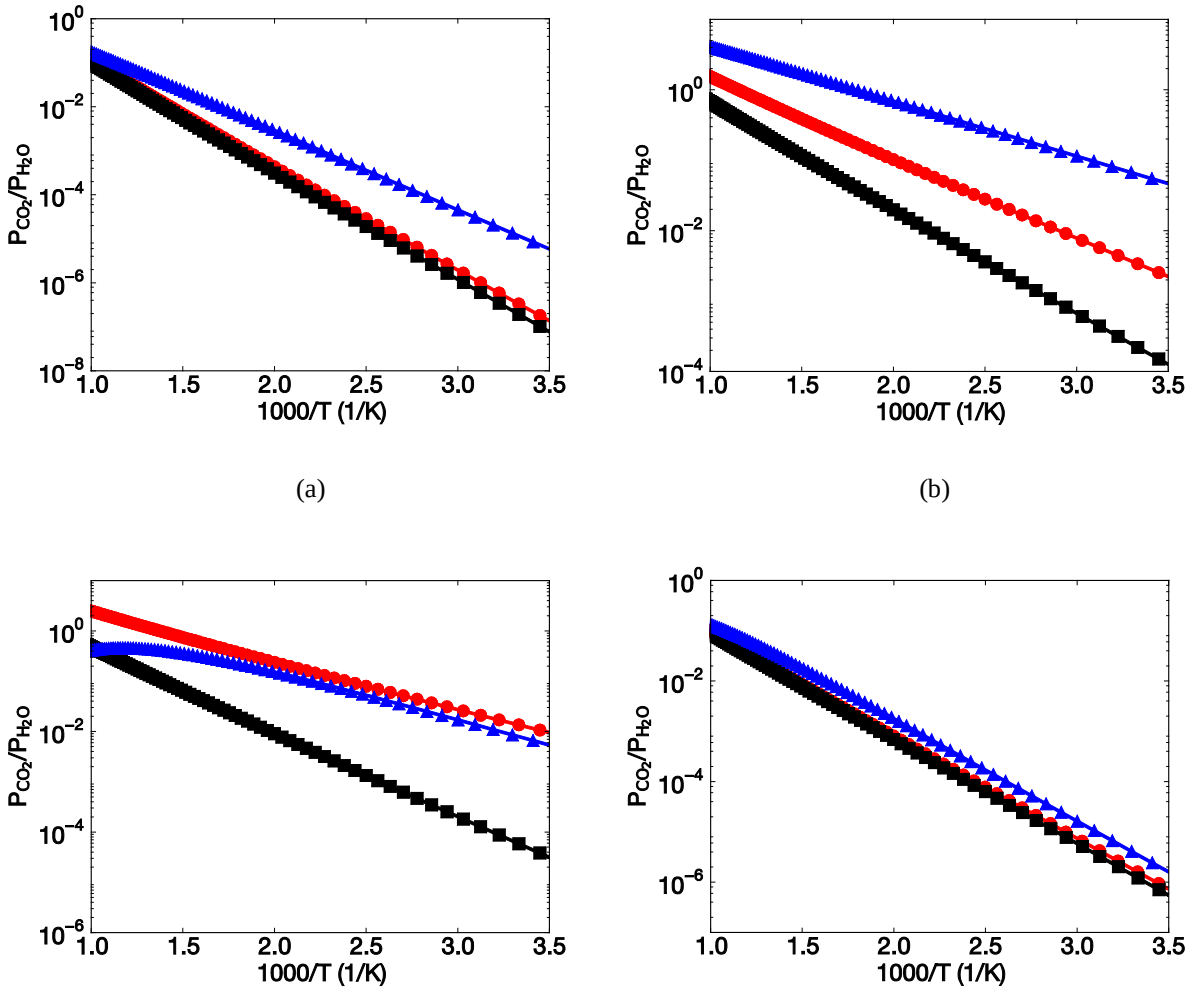

Figure 3.5. Comparison of van't Hoff plots for hydroxides reacting with CO_2 computed from HSC data (blue triangles), from PBEsol (black squares), and from experimental heats of reaction complemented with DFT (red circles, see text for details). (a) $Mn(OH)_2 + CO_2 \rightleftharpoons MnCO_3 + H_2O$; (b) $Ni(OH)_2 + CO_2 \rightleftharpoons NiCO_3 + H_2O$; (c) $Zn(OH)_2 + CO_2 \rightleftharpoons ZnCO_3 + H_2O$; (d) $Cd(OH)_2 + CO_2 \rightleftharpoons CdCO_3 + H_2O$.

The van't Hoff plots computed using the experimental formation enthalpies for the carbonate reactions involving $Mn(OH)_2$, $Ni(OH)_2$, $Zn(OH)_2$, and $Cd(OH)_2$ are plotted in Figure 3.5(a)-(d), along with plots computed from HSC data and the PBEsol functional. In general, our calculations are not in as good agreement with HSC data for the hydroxides as the oxides. For $Mn(OH)_2$ and $Cd(OH)_2$, the curves based on PBEsol energies are comparable to the curves based on experimental enthalpies of formation, but the pressure ratio of CO_2 to H_2O is significantly

underestimated at low temperatures for the Mn system. For $Ni(OH)_2$ and $Zn(OH)_2$ the PBEsol calculations severely underestimate the partial pressure ratio, while the calculations using experimental heats of formation perform significantly better, although there is still a dramatic underestimation of the pressure ratio for the $Ni(OH)_2$ system.

Overall, the van't Hoff plots based on PBEsol energies have comparable accuracy to the plots computed from experimental heats of formation, except for a few cases. We therefore conclude that the PBEsol functional can be used to predict the reaction equilibrium purely from theoretical calculations with reasonable accuracy for most cases, but that one should be aware that there may be significant errors for specific systems.

We now turn to the three systems in Figure 3.5 that are not in good agreement with HSC data when using the PBEsol energies, namely, reactions involving $Mn(OH)_2$, $Ni(OH)_2$, and $Zn(OH)_2$. The discrepancies between our calculations and the HSC data can be traced back to the differences between the reaction enthalpy computed from PBEsol functional and HSC reaction enthalpies noted in Table 3.2 for these same systems. We see from Table 3.2 that the experimental reaction enthalpies for $Mn(OH)_2$ and $Ni(OH)_2$ are in poor agreement with the HSC values. This explains why use of the experimental formation energies in Figure 3.5(a) and (b) does not result in better agreement with the HSC van't Hoff plots. It is likely that either the experimental data or the HSC data are in error for these two systems.

3.3.4 Screening materials for CO_2 capture

We have used the linear programming method to determine the phase diagrams for the TM-C-O-H systems, where TM = Mn, Ni, Zn, and Cd. All the zero-temperature energies used in the calculations were computed from the PBEsol functional and the free energy contributions for the

solids were computed with the PW91 functional, as before. Fig. 6 shows the calculated phase diagrams for all for TM systems at a fixed water partial pressure of 0.1 bar. These phase diagrams can be used to screen the suitability of the TM systems for CO_2 capture, based solely on thermodynamics. We note that favorable thermodynamics is a necessary but not sufficient condition for a suitable CO_2 capture material. Materials must also have acceptable kinetics for capture and regeneration, in addition to low cost, materials safety, cyclability, etc. We examine both pre- and post-combustion capture conditions and assume that capture must take place at conditions where the equilibrium pressure of CO_2 from the carbonate is at least an order of magnitude lower than partial pressure of CO_2 in the gas, and that regeneration of the material will be carried out at a temperature that would generate an equilibrium CO_2 partial pressure of about 10 bar. These are arbitrary targets, but should be a reasonable guess for practical operation. The partial CO_2 pressure for pre-combustion capture conditions is around 20-25 bar and the temperature is between 523 and 723 K to integrate with water gas shift reactor.[16] Post-combustion flue gas has a partial pressure of CO_2 of about 0.1–0.2 bar and the temperature range is from about 300 to 350 K.[2] Based on our predicted phase diagrams, we make the following observations about the suitability of the various materials for reversible CO_2 capture: The hydroxides are irrelevant for CO_2 capture for all the transition metals studied at low partial pressures of H_2O because the temperature and pressure ranges over which the hydroxide materials are stable are too low. For example, even if one started with the hydroxide phase it would likely first convert to the oxide phase before CO_2 capture, and regeneration of the carbonate phase would produce the oxide, not the hydroxide. The MnO system may be suitable for CO_2 capture under both post- and pre-combustion conditions. If we assume $P_{CO_2} = 0.1$ bar for post-combustion capture, then we see from Fig. 6 that even at the highest temperature for

CO_2 capture (350 K) there is a significant driving force for conversion of MnO to $MnCO_3$. The CO_2 could be released at about 650 K, where the partial pressure of CO_2 is about 10 bar. This is a fairly large temperature swing, which may make post-combustion capture with MnO cost prohibitive based on energy consumption. For pre-combustion, MnO will capture CO_2 at a partial pressure of about 10 bar below about 600 K and then could be regenerated by heating above 650 K to produce a stream of pure CO_2. The NiO material could be used for post-combustion capture, but not pre-combustion. Post-combustion absorption will occur below about 350 K and could be regenerated above 460 K. The equilibrium pressure of CO_2 for the NiO system at pre-combustion temperatures is too high for practical consideration. The ZnO system, like the NiO system, might be used for post- but not pre-combustion. The equilibrium temperature required to generate P_{CO_2} = 0.1 bar is around 350 K while P_{CO_2} = 10 bar occurs at about 440 K for $ZiO/ZiCO_3$. Hence, it may be necessary to cool post-combustion gases slightly in order to have a sufficiently large driving force for ZnO to absorb CO_2; this may make this material unsuitable for post-combustion capture. Cadmium oxide could be used for both post- and pre-combustion capture, since there is a large driving force to absorb CO_2 from post-combustion flue gas; the temperature required to generate 10 bar CO_2 in this system is 680 K. Pre-combustion capture could take place at the lower end of the pre-combustion temperature range. However, the toxicity of the Cd system would preclude its wide-spread use.

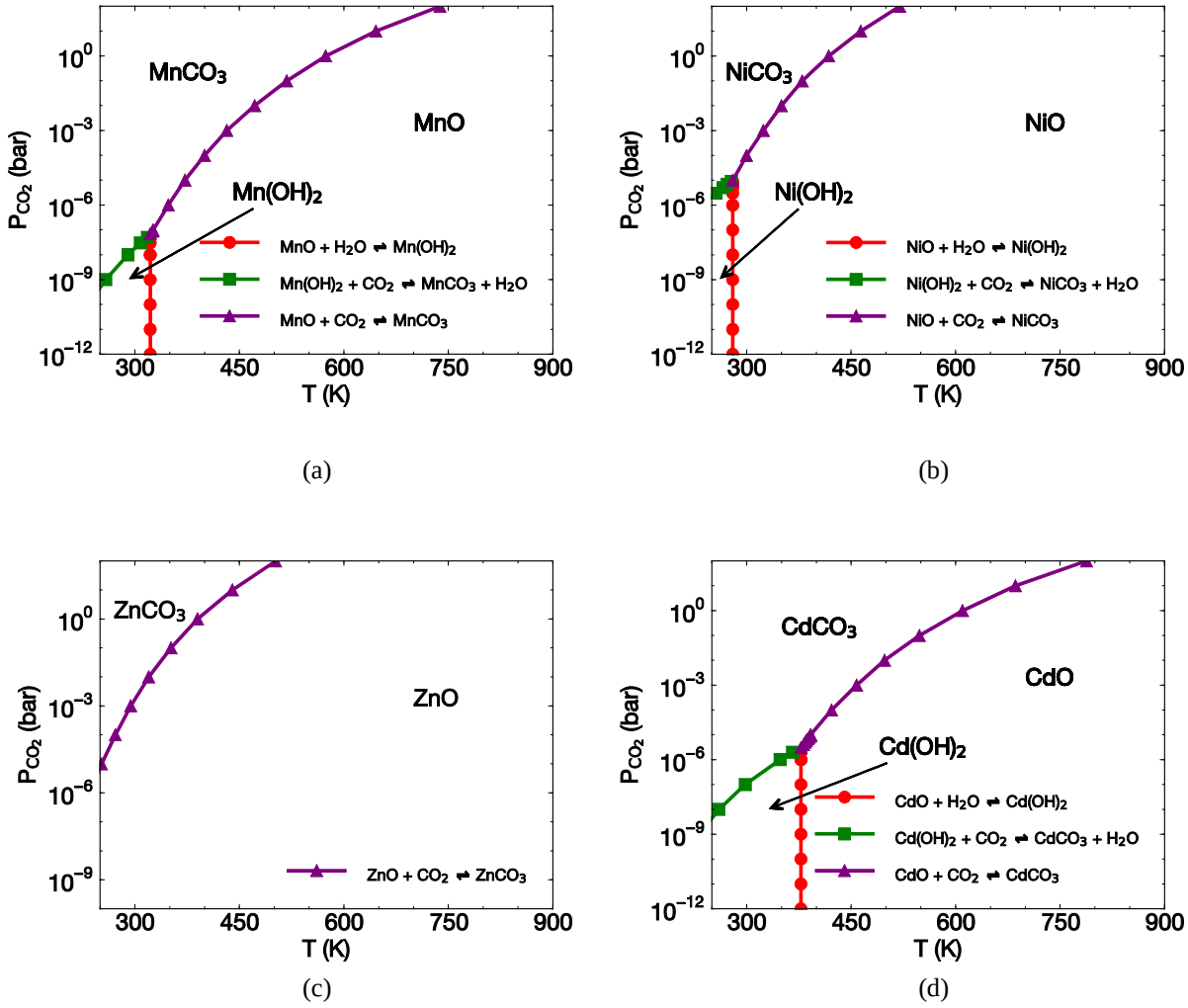

Figure 3.6. Phase diagrams computed from DFT. (a) Mn-C-O-H; (b) Ni-C-O-H; (c) Zn-C-O-H; (d) Cd-C-O-H.

3.3.5 Increasing the accuracy of DFT predictions

We have seen that DFT calculations of both reaction enthalpies and equilibrium van't Hoff plots for the systems considered here are not always in good agreement with experimental data. Ideally, one would like to be able to use DFT to predict the phase diagrams for a wide range of CO2 capture materials with acceptable accuracy to be able to screen new materials. Our calculations indicate that this is not always the case for the functionals we have used. In this

section we discuss the possibility of using higher accuracy computational approaches to predict reaction thermodynamics. It is well known that the local density approximation within DFT usually underestimates lattice constants for solids, whereas GGA frequently overestimates lattice constants.[151] These trends are systematic and consistent for a large number of solids.[151] Lattice constants play an important role in determining a number of properties, for example, unit-cell geometry, volume, cohesive energy, bulk moduli, phonon frequencies, and surface energies.

The TPSS and revTPSS meta-GGA functionals are so-called "third rung" functionals in the "Jacob's ladder" approach to density functional approximations.[24] These are considered "higher level" functionals than GGA because they satisfy more fundamental constraints nonempirically.[24] The TPSS functional is based on the PBE functional while revTPSS is based on the PBEsol functional. The revTPSS functional gives improved lattice constants compared with the TPSS functional.[151, 155] As noted above, the performance of the TPSS and revTPSS functionals is better than GGA level functionals at predicting the enthalpy of formation of carbonates and oxides (see Table 3.3). Unfortunately, the reaction enthalpies and the associated van't Hoff plots computed with these meta-GGA functionals are not as accurate as data computed from the PBEsol functional. We speculate that this may be due to the use of pseudopotentials that are not tuned for meta-GGA functionals.

The next level beyond meta-GGA ("fourth rung") is the (semi-empirical) hybrid functional, which is constructed by introducing a certain amount of exact Fock exchange energy, while retaining part of the local or semi-local density functional exchange energy. These methods are computationally very demanding compared with conventional LDA or GGA functionals. B3LYP[34, 159] is one of the most popular hybrid functionals used. However, B3LYP was designed for molecules, and the empirical parameters were computed from a fit to the

atomization energies, ionization potentials, and proton affinities from Pople's G2 set.[159] Thus, it is not surprising that B3LYP does not perform much better at predicting lattice constants and atomization energies for metals than conventional LDA or GGA functionals, as shown in the work by Kresse *et al.*[160] The PBE0[161, 162] and the associated HSE03[163] functionals are other "fourth rung" functionals available for calculating the properties of solids. In the HSE03 scheme, the Fock exchange term is split into a short- and a long-range part. Only the short range part of the Fock exchange is mixed with the DFT exchange, while the long range part is neglected, but compensated for by the corresponding PBE long range term. Thus, HSE03 is less computationally demanding than PBE0 or B3LYP. HSE03 and PBE0 functionals do improve the predicted lattice constants and bulk moduli of selected solids, but they do not improve the atomization energies for metals.[164, 165] Better agreement with experiments for calculated heats of formation of selected solids have been reported using the HSE03 and PBE0 functionals compared with the conventional PBE functional.[164, 165]

In addition to the different exchange-correlation functionals, there has been some work on accurate calculation of enthalpies of formation through post-Hartree Fock incremental methods[166, 167] or Møller-Plesset second order DFT calculations.[168, 169] However, these methods require enormous computational effects, with computations scaling like $\mathrm{O}\left(N^5\right)$ where N is the number of electrons, and are not widely tested.

Since PBEsol functional just modifies two parameters of the original PBE functional,[151] the computational cost is essentially the same as the conventional PW91 or PBE functionals, but is much less than the meta-GGA and hybrid functionals. For instance, the CPU time needed for HSE03 functional, which is faster than PBE0 and B3LYP functional, is at best 2-4 times larger than PBE functional calculations on the same system.[170] Weighing the computational costs and

accuracy of thermodynamic properties of reactions studied in this chapter, PBEsol appears to be a reasonable compromise. However, we note that the accuracy of PBEsol is due in part to a cancellation of errors. Thus, there is certainly a need to develop more accurate and efficient methods for predicting the thermodynamic properties of solids and phase diagrams.

In addition to the higher level functionals discussed above, we note that the DFT+U method is a successful approach for treating strongly correlated systems.[171, 172] However, it is not a predictive method in general. It is known that the calculated energies and other properties of a material strongly depend on the U_{eff} value used in the DFT+U calculations.[173-175] In some cases a single unique U_{eff} may not give both accurate geometries and energies.[173] Therefore DFT+U may not be appropriate for predicting reaction thermodynamics involving compounds were experimental values are not available. Moreover, the DFT+U approach is not appropriate for the gas phase species for CO_2 capture reactions, since these are not strongly correlated.

3.4 CONCLUSION

We have obtained the thermodynamic properties of transition metal oxides, hydroxides and carbonates containing Mn, Ni, Zn, Cd from first-principles DFT calculations using the PW91, PBE, PBEsol, TPSS, and revTPSS functionals and predicted the chemical equilibria for CO_2 capture reactions involving these materials. Generally speaking, the PBEsol functional performs better at predicting the reaction thermodynamics for oxide carbonate reactions compared with the other four functionals. Although the TPSS and revTPSS functionals are better at predicting the

enthalpy of formation for oxides and carbonates, larger errors for other compounds leads to the observed drastic underestimation in the van't Hoff plots compared with HSC data. On the other hand, we believe that better agreement found in computing the van't Hoff plots using the PBEsol functional is due in part to a cancellation of errors. Specifically, errors in the heats of formation for oxides that are partially offset by errors in the heats of formation of carbonates, which then cancel when computing the heats of reaction. The van't Hoff plots constructed using the PBEsol functional are comparable in accuracy to plots using experimental heats of formation when compared with HSC data, except for systems containing $Ni(OH)_2$ and $Zn(OH)_2$. Therefore, we believe that phase diagrams for carbon capture reactions can be predicted with reasonable accuracy within DFT using the PBEsol functional. We have also predicted their CO_2 capture performance through a theoretically rigorous linear programming method. Taking an adsorption temperature having a partial pressure of CO_2 that is at least an order of magnitude lower than the pressure of CO_2 in the gas stream and a regeneration temperature sufficient to generate 10 bar pressure of CO_2, we predict that all the oxides may be useful for post-combustion CO_2 capture. In contrast, only MnO and CdO are possibilities for pre-combustion capture. We predict that none of the hydroxides are suitable for CO_2 capture, since they will decompose at relatively low temperatures and partial pressures of CO_2.

4.0 DEVELOPMENT OF A REAXFF REACTIVE FORCE FIELD FOR TETRABUTYLPHOSPHONIUM GLYCINATE AND APPLICATION TO CO_2 CAPTURE

The Content of this chapter is taken from Bo Zhang, Adri C. T. van Duin and J Karl Johnson, "Development of a ReaxFF reactive force field for tetrabutylphosphonium glycinate and application to CO_2 capture", in preparation.

4.1 INTRODUCTION

The increase of CO_2 concentration in the atmosphere by anthropogenic activity has recently become a major public concern due to its link with global climate change.[1, 3] While renewable energy sources and nuclear power offer the potential to reduce carbon emissions over the long-term, fossil fuel will remain the major source of energy for several decades. Therefore, CO_2 capture and storage is one of the most promising strategies to mitigate CO_2 emissions in the near future. Chemisorption (scrubbing) of CO_2 with aqueous monoethanolamine (MEA)[2, 114] is one of commercially available technique that is able to capture 90% of the CO_2 from flue gas. However, this approach suffers from thermal and chemical degradation of MEA,[115, 116] and high energy costs[117] to regenerate the solvent. Therefore, there is much effort devoted to the development of

new sorbents, either in solid form, such as oxides,[15, 21, 83, 127, 150, 176] hydroxides,[83, 136, 141, 150, 176] carbonates,[17, 18, 150] and metal organic frameworks,[120-122] or in liquid form, such as amine-based solvents[117, 177, 178] or ionic liquids (ILs).[37, 42, 43] As demonstrated by many studies from experiments and theoretical calculations, the interaction strength between CO_2 and ILs can be tailored by different combinations of cations and anions. The interaction can be tuned to range from physical interactions (~10-20 kJ/mol),[179] to complexation interactions (~30-40 kJ/mol),[180] to chemical interactions (~60-80 kJ/mol).[44] This ability to tune the interaction strength between CO_2 and the sorbent makes ILs promising candidates for CO_2 sorbents suitable for specific capture conditions. However, there are a tremendous number of different cations and anions can be chosen to make an IL. It is impractical to synthesize all the possible ILs and test their CO_2 capture capability. This process can be accelerated by screening ILs through calculations of thermodynamic and transport properties from molecular simulations. Currently, most classical force fields employ harmonic potentials or similar simple models of bonds length, angles and torsions, along with van der Waals (vdW) and Coulomb interactions to describe physical interactions for a variety of systems from condensed phase to liquid and gas phases. This methodology of representing of bond lengths, angles, torsions with such simple functional forms makes the molecular simulations with classical force fields fast for non-chemically interacting systems. There are already a number of different classical force fields for different ILs physically interacting with CO_2.[36, 37] However, considering the complicated interaction/reaction between ILs and CO_2, *i.e.*, physical, complexation or chemical interactions, classical force fields will not capture all the important interactions between ILs and CO_2, especially those involving strong chemical interactions. Although simulations of reactive ILs with CO_2 have been performed by *ad hoc* mixing of different fractions of unreacted ILs and reacted ILs,[181, 182] this approach lacks

information on how reactions between ILs and CO_2 take place and how the fraction of reacted CO_2 changes with process condition. Thus, in order to cover all the interactions found between ILs and CO_2, we need a force field that is not only good at describing the physical interactions, but is also accurate for chemical interactions/reactions. ReaxFF proposed by van Duin *et al.*[14, 49] is one of the force fields that can provide such functionality. ReaxFF is bond-order dependent thus naturally it allows for bond breaking/forming during simulation. ReaxFF has been successfully applied to many different chemical systems, such as crystal and surfaces,[183] glycine tautomerization[184] and hydrocarbon oxidations.[49]

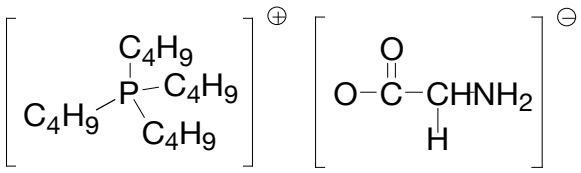

Figure 4.1. The molecular structure of tetrabutylphosphonium glycinate.

In this chapter, tetrabutylphosphonium glycinate ($[P(C_4)_4][Gly]$) has been chosen as a model IL since it has both $-CO_2^-$ and $-NH_2$ functional groups which are typical functional groups that interacts with CO_2 by complex formation and reactive interactions, respectively. Thus, the physical, complexation and chemical interactions will be expected occur simultaneously in this IL/CO_2 system. Shiflett *et al*. measured the phase equilibrium between CO_2 and 1-butyl-3-methylimidazolium acetate ([bmim][Ac]), and suggests that complex formation rather than chemical reaction dominates the interaction between CO_2 and [bmim][Ac].[185] This complex formation interaction is confirmed by other studies.[180, 186, 187] Carvalho *et al*. compared the solubility data measured for two ILs, [bmim][Ac], 1-butyl-3-methylimidazolium trifluoroacetate ([bmim][TFA]).[187] A two stage absorption mechanism was used to explain how CO_2 interacts

with these ILs. At lower CO_2 pressure, chemisorption (complex formation) between CO_2 and acetate dominates, after the chemisorption site is saturated, physisorption dominates.[187] *Ab initio* calculations show that acetate is a stronger Lewis base than trifluoroacetate, and CO_2 acts as the Lewis acid when interacting with this IL.[187] The possibility that the reaction takes place to form acetic acid is excluded,[187] thus, CO_2 must be quickly changing among neighbor carboxylates, like a complex, rather than binding to carboxylate group. These two types of interaction between acetate anions and CO_2, complexation and physical type interactions, have been verified through *ab initio* molecular dynamic (MD) simulations by Shi *et al.*[188] They observed that CO_2 was primarily in a bent configuration during the simulation, because of the stronger complexation interaction and that leads to high CO_2 solubility.[188] They also conclude that the cation (1-ethyl-3-methylimidazolium) can compete with acetate anion for CO_2 adsorption since the complexation interaction is not strong and comparable to the physical interaction between CO_2 and cation.[188] Another popular functional group used in ILs for CO_2 capture is the amine group. Bates *et al.*[42] was one of the first groups to propose the idea of incorporating amine functional groups into ILs for CO_2 capture. The CO_2 solubility in 1-(3-aminopropyl)-3-n-butylimidazolium tetrafluoroborate ([abmim][BF_4]) is much higher than in [hmim][PF_6].[42] A one-step mechanism is proposed to explain the reaction with the evidence from FT-IR and ^{13}C NMR as shown in Figure 4.2. Basically, only one half of [abmim] reacted with CO_2 to form carbamate and the other becomes a quaternary ammonium-appended species. Although the experimental data show [abmim][BF_4] is a promising sorbent for CO_2 capture, but its high viscosity makes it impractical to use.[42] This high viscosity is also observed by other experiments for amine based ILs.[189, 190] Sanchez *et al.* also concluded that primary amine functionalized ILs have greater CO_2 solubility than tertiary amine functionalized ILs.[189] Zhang *et al.* have prepared several new ILs based on

tetrabutylphosphonium amino acid $[P(C_4)_4][AA]$, where AA = glycine, L-alanine, L-β-alanine, L-serine, L-lysine.[43] Due to high viscosity, these ILs were impregnated into silica gel supports. The supported ILs show faster CO_2 absorption than the bulk ILs.[43] They proposed that a CO_2 molecule attacks the nitrogen site of the amine group and forms a $-NHCO_2^-$ group, as measured by IR and ^{13}C NMR, and the leaving proton will attach to the formed $-NHCO_2^-$ or original $-CO_2^-$ in the anion to form a new CO_2H group, which will form a hydrogen bond O–H···N with the electron pair of NH_2 in another ILs as shown in Figure 4.3.[43] The mechanism differs from that proposed by Bates *et al.* in the position of the leaving proton. These authors suggest that the leaving proton still attaches to the ILs to which CO_2 is absorbed to rather than transfers to another ILs.[43] But when there is water present, the mechanism is different; the $[P(C_4)_4][AA]$ will react with CO_2 to form bicarbonates, which leads to a 1:1 ratio of CO_2 and ILs as shown in Figure 4.4.[43] Contrary to the previous mechanism where the ratio of IL with CO_2 is 2:1, Gurkan *et al*. proposed a 1:1 stoichiometry mechanism based on FTIR measurements and theoretical calculations shown in Figure 4.5.[44] The studied ILs are trihexyl(tetradecyl)phosphonium prolinate ($[P(C_6)_3C_{14}][Pro]$) and methioninate ($[P(C_6)_3C_{14}][Met]$). The calculated heat of reaction to form complexes from *ab initio* calculations of gas phase anions are in good agreement with experiments.[44] Yu *et al*. suggested that hydrogen bond networks formed between amine groups from the cations and the anions in pure amine functionalized ILs and these networks are responsible for the observed high viscosity.[191]

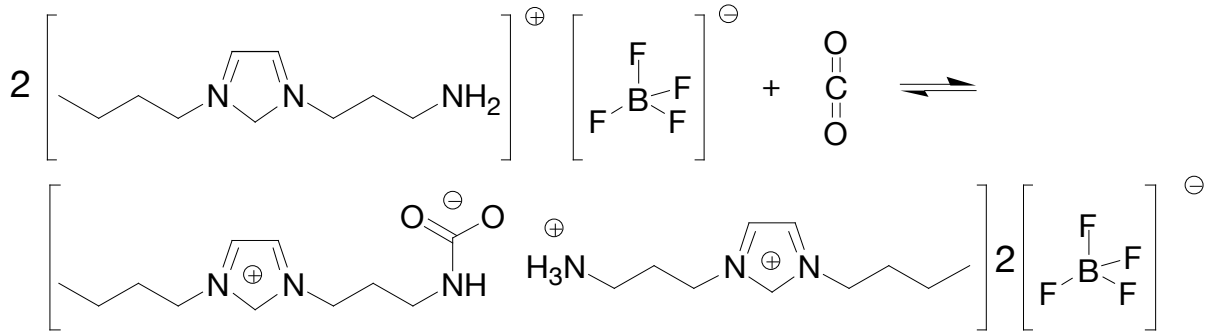

Figure 4.2. Proposed mechanism of [abmim][BF_4] reaction with CO_2.[42]

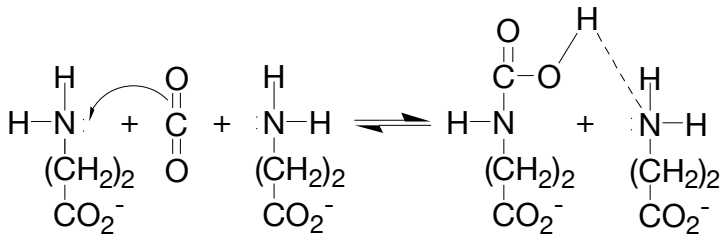

Figure 4.3. Proposed reaction mechanism for [$P(C_4)_4$][β-Ala] with CO_2, where H attaches to the formed $-NHCO_2^-$ group.[43]

$$[H_2N\text{-}CH_2\text{-}COO]^- + CO_2 + H_2O \rightleftharpoons {}^+H_3N\text{-}CH_2\text{-}COO^- + [HCO_3]^-$$

Figure 4.4. Proposed reaction mechanism of [$P(C_4)_4$][Gly] with CO_2 when water is present.[43]

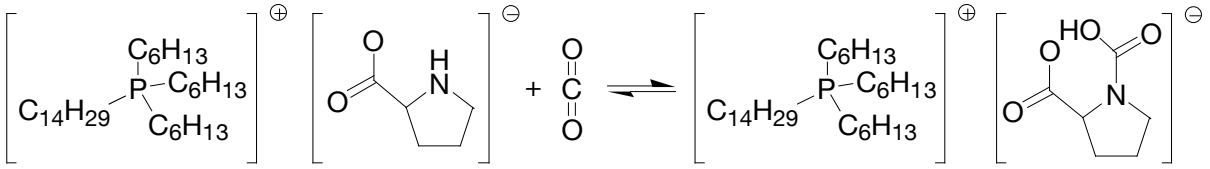

Figure 4.5. Proposed reaction mechanism for [$P(C_6)_3C_{14}$][Pro] with CO_2 at 1:1 ratio.[44]

Zhou *et al.* have developed an AMBER force field for $[P(C_4)_4][Gly]$ and validated it by comparing with experimental density and heat capacities.[192] Kowsari *et al*. used the same force field to compute the transport properties of $[P(C_4)_4][Gly]$.[193] Gutowski *et al*. further used MD combined with *ab initio* calculations to explain possible mechanism for drastic increase of the viscosity when amine functionalized ILs interacting with CO_2.[181] When CO_2 is absrobed, a strong, pervasive hydrogen-bonded network is formed to slow the translational and rotational dynamics of the ILs, which are manifest in the high viscosity.[181] Wu *et al*. studied a mixture of unreacted tetrabutylphosphonium 2-cyanopyrrolide and reacted IL with CO_2 at different composition and found no significant increase of the viscosity of the reacted ILs from MD simulation due to few hydrogen bonds formed during the reaction, as compared with other task-specific ILs.[182]

We will present the development and validation of ReaxFF force field for $[P(C_4)_4][Gly]$ and CO_2 in this chapter. The reaction mechanism and its energetics will be discussed in the first section. The next section will be devoted to force field optimization. Finally, the optimized force field will be used to probe the interactions/reactions between CO_2 and $[P(C_4)_4][Gly]$.

4.2 COMPUTATIONAL DETAILS AND METHODOLOGY

4.2.1 ReaxFF reactive force field formalism

ReaxFF is a reactive force field that can describe bond breaking and bond formation events relying on interatomic distances.[14, 49] Unlike traditional force fields, one element can be described by merely one single atom type, even within different chemical environments, in the

ReaxFF formulism. Reaction site or connectivity information is not needed beforehand. Instead they are derived from bond orders calculated from interatomic distances at every MD step. Similarly to the traditional force field, the vdW and Coulomb interactions are also accounted for by pair interactions from all atoms irrespective of connectivity. A shielding term is also included to avoid excessively close range non-bonded interactions. Polarization effects are considered through a geometry dependent charge equilibration scheme.[194, 195] A detailed description of the ReaxFF potential function can be found elsewhere.[14, 49]

The force field parameters in this chapter were determined by starting from a previous glycine force field[184] with new training sets relevant to $[P(C_4)_4][Gly]$, CO_2 and their reactions. In order to obtain a reasonable set of parameters, single-parameter search optimization method[196] is used to minimize the following sum of squares

$$\text{Error} = \sum_{i=1}^{n} \left(\frac{x_{i,\text{DFT}} - x_{i,\text{ReaxFF}}}{\sigma} \right), \tag{4.1}$$

where $x_{i,\text{DFT}}$ is the value calculated from DFT, $x_{i,\text{ReaxFF}}$ is the value computed from ReaxFF, σ is the weighting factor to control accuracy.

4.2.2 Training set generation

An extensive set of DFT calculations was performed in order to obtain accurate transition state and reaction energies. Vienna *ab-initio* simulation package (VASP),[90-93] a periodic plane-wave DFT code, was used to obtain the reaction transition state and reaction energies. Core-electron interactions were described by projector augmented-wave (PAW) potentials.[94, 95] Generalized gradient approximation (GGA) exchange-correlation functionals, particularly, PBE of Perdew, Burke and Ernzerhof were employed.[28, 29] A plane-wave cutoff energy of 520 eV was used for all

calculations. The k-point meshes were 1 by 1 by 1. Geometry relaxation of atomic positions with stopping criteria of energy less than 0.1 meV and force less than 0.01 eV/Å were used to obtain the ground state of $[P(C_4)_4][Gly]$ and CO_2. The conjugate gradient algorithm was used in conjunction with the PBE functional. It is well known that current implementation of DFT cannot properly describe the long-range electron correlation that represents the dispersion (vdW) interactions due to its local or semi-local character.[8] Various methods have been proposed to overcome this shortcoming of DFT.[60-66] DFT-D2 is one of the simplest methods that introduce an additional dispersion energy term to the Kohn-Sham energy to empirically account for the dispersion interactions.[61] This dispersion energy term can be calculated as[61]

$$E_{\text{disp}} = -s_6 \sum_{i=1}^{N_{\text{at}}-1} \sum_{j=i+1}^{N_{\text{at}}} \frac{C_6^{ij}}{R_{ij}^6} f_{\text{dmp}}\left(R_{ij}\right), \tag{4.2}$$

where N_{at} is the number of atoms in the system, C_6^{ij} is the dispersion coefficient for atom pair *ij*, s_6 is the global scaling factor that only depends on the functional used, R_{ij} is the interatomic distance, and f_{dmp} is the damping function which can be written as $f_{\text{dmp}} = \frac{1}{1+e^{-d\left(R_{ij}/R_r-1\right)}}$, where R_r is the sum of atomic vdW radii.

The minimum energy path of reaction between $[P(C_4)_4][Gly]$ and CO_2 and reaction barriers were obtained from the climbing-image nudged elastic band (NEB) method.[197-201] The stopping criterion of NEB calculation was that forces must be less than 0.01 eV/Å. The obtained transition state were all verified by frequency analysis, where only one significant imaginary frequency was found.

In order to accurately describe $[P(C_4)_4]^+$, another training set was obtained by Gaussian 09 program.[5] The calculations were carried out at PBE/aug-cc-pvtz level to ensure that the

functional form was the same as used in VASP. The DFT-D2 energy was added *post hoc* with Grimme's code.[62] P-C bond dissociation energies, C-P-C angle distortion energies, and C-C-P-C rotational barriers were calculated by fixing the bond/angle of interest at a specified value and optimizing all other coordinates. We compared P-C bond dissociation energy of $[P(C_4)_4]^+$ with VASP and $[P(C_2)_4]^+$ with Gaussian and found no significant difference. Therefore the C-P-C angle distortion, and C-C-P-C rotational barriers from $[P(C_2)_4]^+$ cation can be used safely to speed up to data generation. The C-O bond dissociation and O-C-O angle distortion in CO_2 molecule as well as the N-C bond dissociation of CO_2 molecule with gas phase $[Gly]^-$ anion were also calculated with Gaussian and included in the training sets.

In order to predict the correct density of pure $[P(C_4)_4][Gly]$, a pseudo equation of state (EoS) was also added to the training sets. This pseudo EoS is calculated with only one IL pair by changing the center of mass of the cation and anion according to the volume change, while keeping the relative positions of atoms within ions fixed. The structures obtained from this procedure were not relaxed to ground states and only single point energies were calculated and compiled into the pseudo EoS.

In the parameterization process, the structures in training set were relaxed with the ReaxFF force field while the key geometry parameters are constrained according to the specified reaction coordinates. For example, for P-C bond dissociation energy, the key geometry parameter was the distance between P atom and C atom. Thus, this distance was constrained while other geometry variables were relaxed to reach the ground state in ReaxFF.

4.2.3 Molecule dynamics simulation details

Molecular dynamics simulations were performed with Large-scale Atomic/Molecular Massively Parallel Simulator (LAMMPS) molecular dynamics package.[202] The isothermal-isobaric (*NpT*) and canonical (*NVT*) ensembles were employed with a timestep of 0.5 fs. Temperature was maintained at 300 K using a Nosé-Hoover thermostat with a damping factor of 50 fs. Pressure was maintained at 1 atm for all *NpT* simulations using by Nosé-Hoover barostat with a damping factor of 500 fs.

4.3 RESULTS AND DISCUSSION

4.3.1 Reaction pathway analysis of $[P(C_4)_4][Gly]$ with CO_2

Figure 4.6(a) and (b) shows the initial configurations used to generate the NEB pathway. In the reactant state (see Figure 4.6(a)), the distance between the carbon atom in CO_2 to the nitrogen atom in $[Gly]^-$ is 1.62Å, while the CO_2 angle O-C-O is about 137.4°. This implies CO_2 already interacts with $[Gly]^-$ very strongly. But this structure still has an energy 10 kcal/mol higher than the product state (see Figure 4.6(b)). In the product state the distance between the carbon atom in CO_2 to the nitrogen atom in $[Gly]^-$ is 1.38Å, while the CO_2 angle O-C-O is about 123.3°. In addition, the proton previous attached to nitrogen in the anion is now shared between the oxygen from CO_2 and carboxylic group from $[Gly]^-$ and with preference for CO_2 as indicated by the shorter bond length between the O in CO_2 and the H (about 1.11Å). These all suggest stronger interaction between CO_2 and $[Gly]^-$ in the product state than the reactant state; the ring structure

appears to further stabilize the structure. Based on the reactant and product structures, a linear interpolating scheme was used to construct the pathway used in NEB calculations. The final minimum energy pathway from NEB calculations is shown in Figure 4.7. There are two energy barriers that were found from the minimum energy pathway. We denote the structure corresponding the first barrier (from left to right) as transition state 1 (shown in Figure 4.6(c)), and denote the structure corresponding the second barrier (from left to right) as transition state 2 (shown in Figure 4.6(d)). We can see that as the CO_2 approaches the amine group in $[Gly]^-$, the proton bonded to the nitrogen atom gradually leaves it and approaches one of the oxygens in the carboxylic group. This results in the formation of transition state 1, where the proton is about mid-way between the nitrogen atom and the oxygen atom in the anion. There is only one significant imaginary frequency (three other modes are very close to zero, and these are assumed to be translational motion) from frequency analysis of transition state 1, and the associated vibrational mode vector is also indicated in Figure 4.6(c), which is the vibrational mode of the proton pointing to the nitrogen atom or the oxygen atom. The barrier height is about 0.7 kcal/mol. After the proton is transferred to the oxygen atom from carboxylic group in anion, the next step in the reaction involves the proton approaching the oxygen atom in CO_2. The second barrier can be observed during this process in the minimum energy pathway; with the barrier height is about 2 kcal/mol, as shown in Figure 4.7. The corresponding structure of transition state 2 can be found in Figure 4.6(d) which shows that the proton is probably librating between the oxygen atom from the carboxylic group and the oxygen atom from CO_2 based on frequency analysis. The transition state is also verified by frequency analysis and only one significant imaginary frequency was found. That mode corresponded to the librational mode. A ReaxFF

training set was constructed from all the VASP and Gaussian 09 calculations, along with some of configurations from the previous training set for glycine.[184]

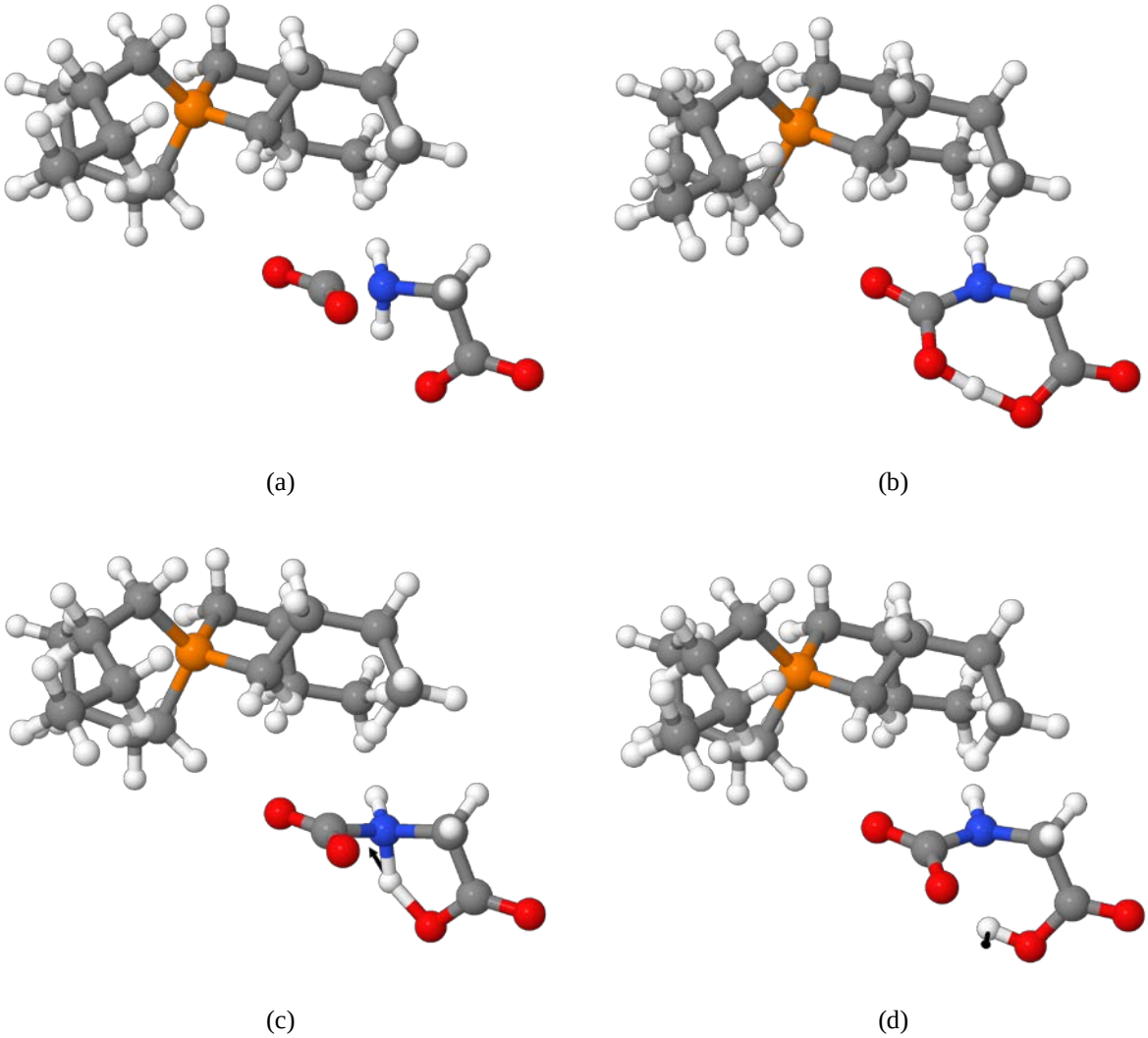

(a) (b)

(c) (d)

Figure 4.6. The structures of $[P(C_4)_4][Gly]$ with CO_2 at various stage of reactions. (a): initial reactant ground state structure of $[P(C_4)_4][Gly]$ and CO_2 from minimization; (b): final product structure of $[P(C_4)_4][Gly]$ and CO_2 from minimization; (c): transition state 1 of reaction between $[P(C_4)_4][Gly]$ and CO_2 obtained from NEB calculation; (d): transition state 2 of reaction between $[P(C_4)_4][Gly]$ and CO_2 obtained from NEB calculation. (a) and (b) have been linearly interpolated to generate initial starting configurations of NEB pathway. (c) and (d) are the configurations obtained as the barriers of NEB pathway. The vibrational mode of the only significant imaginary frequency has been depicted by black arrows in (c) and (d) respectively.

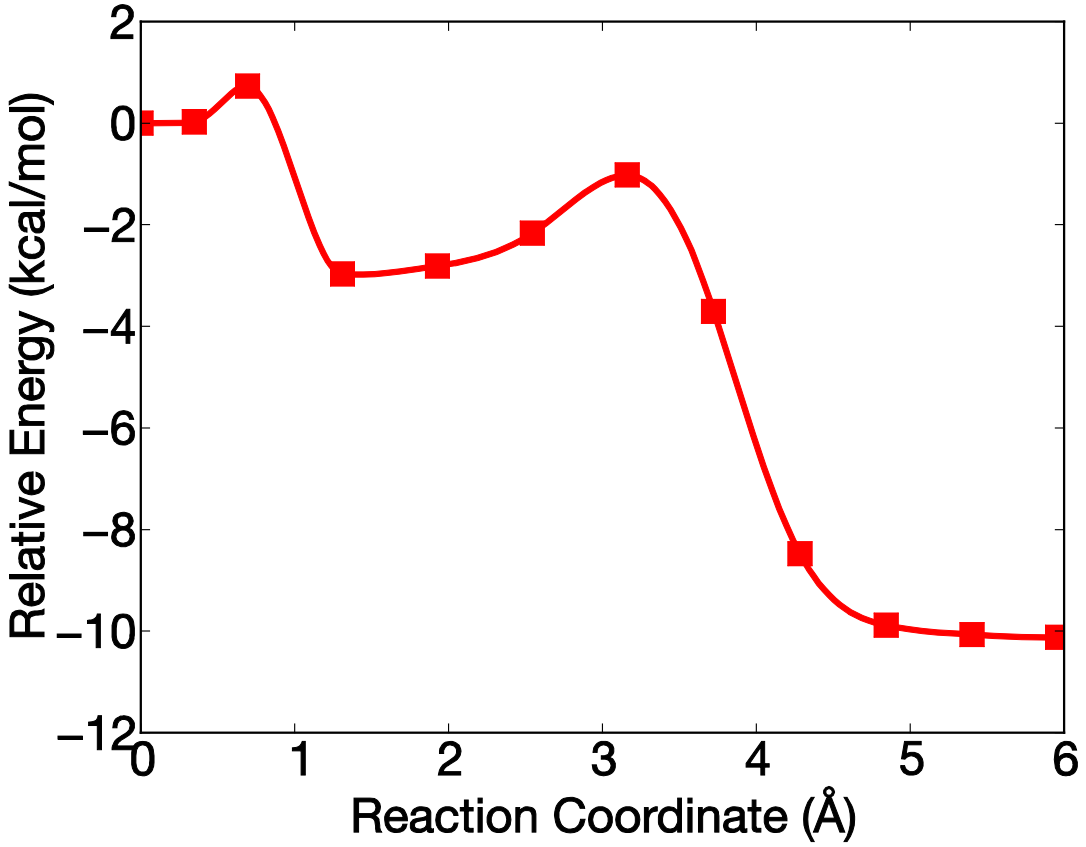

Figure 4.7. The minimum energy pathway obtained from NEB calculation. Some corresponding structures are illustrated in Figure 4.6. From left to right, the structure corresponding to the first point (reaction coordinate = 0) is shown in Figure 4.6(a); the structure corresponding to the third point is shown in Figure 4.6(c); the structure corresponding to the seventh point is shown in Figure 4.6(d); the structure corresponding to the last point is shown in Figure 4.6(b).

4.3.2 ReaxFF force field parameterization

The ReaxFF force field was parameterized against this training set. Figure 4.8 shows the relative energies calculated from DFT and ReaxFF force field for the structures taken from the reaction pathway. Generally, the trend from the ReaxFF energies agrees with the DFT energies although

small discrepancies do exist. For example, the first barrier is overestimated by ReaxFF by about 2 kcal/mol while the second barrier is slightly overestimated by 1 kcal/mol.

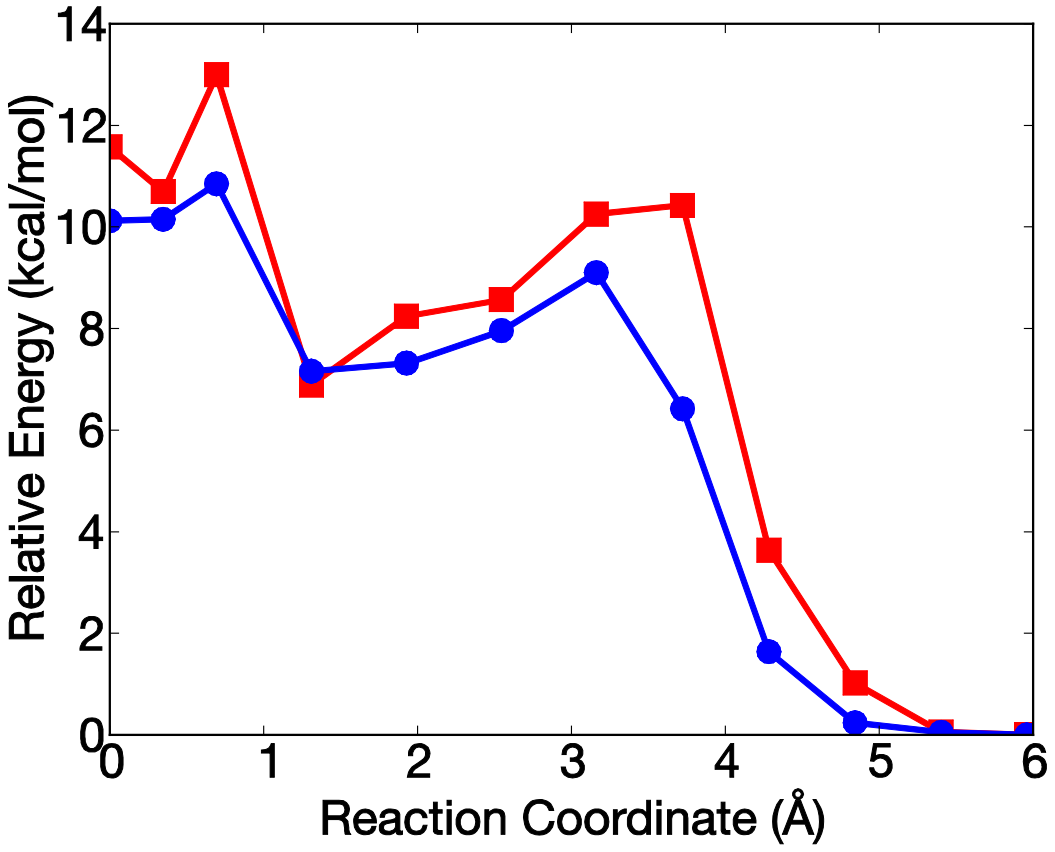

Figure 4.8. Comparison of the DFT and ReaxFF relative energies of the structures from reaction pathway obtained from NEB calculation. Blue circles: DFT energy from VASP NEB calculation; Red squares: ReaxFF energy. The DFT calculations were performed with VASP.

We also parameterized the ReaxFF force field to better describe the $[P(C_4)_4]^+$ cation. To reduce the computational cost for calculating the P-C bond dissociation, C-P-C angle distortion and C-P-C-C dihedral angle distortion energies for $[P(C_4)_4]^+$ cation, the $[P(C_2)_4]^+$ cation is used in Gaussian calculations instead of $[P(C_4)_4]^+$ cation. We tested the P-C bond dissociation relative energies using $[P(C_4)_4][Gly]$ under periodic boundary conditions in VASP as well as cation $[P(C_2)_4]^+$ in Gaussian, and found there is nearly no difference between these two methods as can

be seen from Figure 4.9. The P-C bond stretching energies from ReaxFF agrees fairly well with DFT energies from 1.4Å to 2.7Å. Beyond that the relative energies from ReaxFF are much less than those computed with DFT methods. Since there is no bond breaking for $[P(C_4)_4][Gly]$ reacting with CO_2, this underestimation will not be a big concern as long as the energetics around the P-C bond equilibrium distance are well reproduced by ReaxFF.

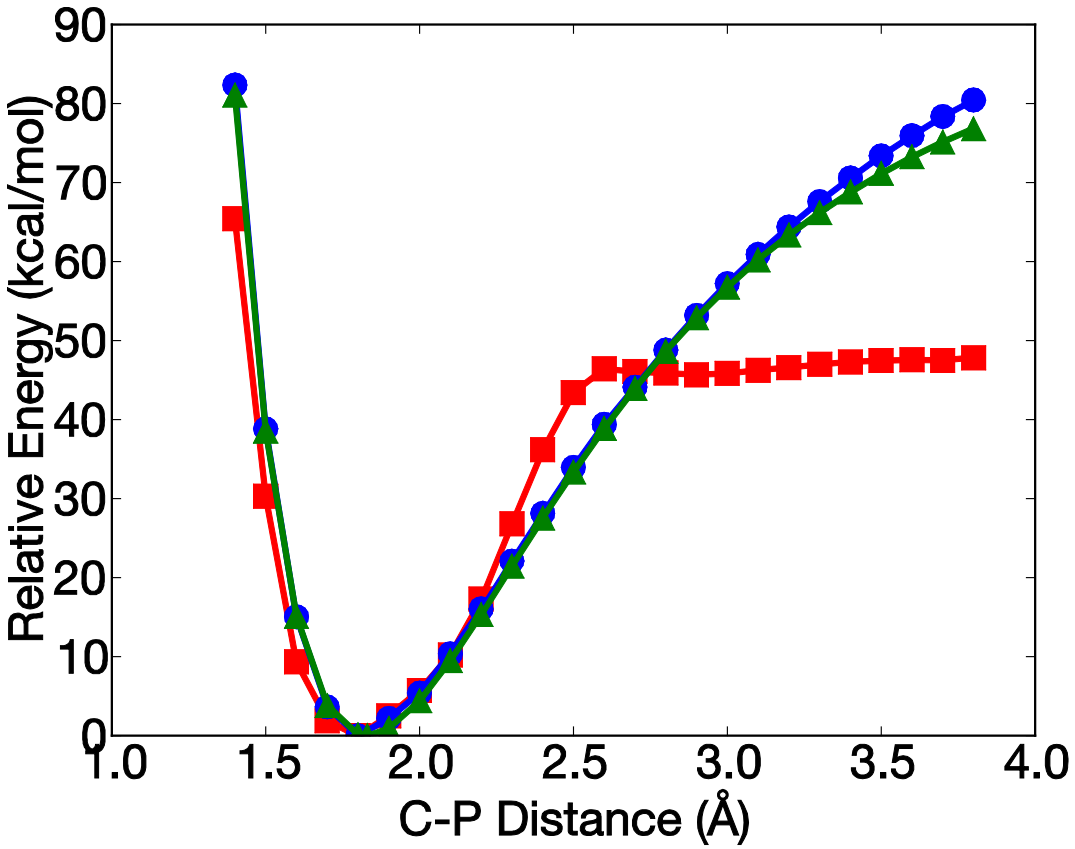

Figure 4.9. Comparison of the DFT and ReaxFF relative energies of P-C bond dissociation in cation $[P(C_4)_4]^+$. Blue circles: DFT energy from VASP for $[P(C_4)_4][Gly]$; Red squares: ReaxFF energy for $[P(C_4)_4][Gly]$; Green triangles: DFT energy from Gaussian for cation $[P(C_2)_4]^+$.

The C-P-C angle distortion and C-P-C-C torsion angle distortion relative energies were calculated using the isolated cation $[P(C_2)_4]^+$ in Gaussian. Figure 4.10 shows the comparison of those relative energies calculated from Gaussian and ReaxFF. Overall, general good agreement

can be found for the C-P-C angle distortion and C-P-C-C rotational barrier between DFT and ReaxFF calculations. The equilibrium angle of C-P-C and C-P-C-C can be predicted by ReaxFF with parameterized force field, although there are some differences when those angles are far away from their equilibrium values.

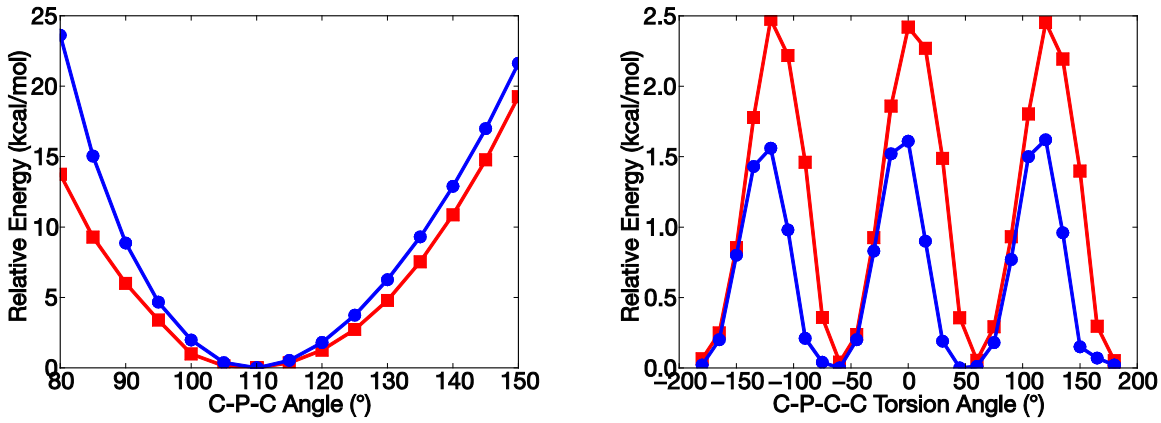

(a) (b)

Figure 4.10. Comparison of the DFT and ReaxFF relative energies of C-P-C angle distortion. (a) and C-P-C-C torsion angle distortion (b) in cation $[P(C_2)_2]^+$. Blue circles: DFT energy; Red squares: ReaxFF energy.

As we noted above, the O-C-O angle for a CO_2 molecule changes depending on its chemical interactions with the anion. For instance, when there is no reaction between CO_2 and the IL, the O-C-O angle should be around 180°. As the reaction goes on, this angle will gradually close to about 120°. Therefore, it is necessary to include the C-O bond dissociation and O-C-O angle bending energies of CO_2 in the training set and optimize the force field to reproduce those energetics from DFT calculations. The optimized ReaxFF force field can reproduce the relative energies of C-O bond stretching calculated from Gaussian up to 2.0 Å as illustrated in Figure 4.11(a) while it will underestimate the energies by about 50 kcal/mol for larger values of C-O distance. The curve of C-O bond dissociation energies from Gaussian calculation is a combination of singlet states and triplet states of CO_2. The singlet CO_2 has a lower energy up to

2.0 Å while the energy of triplet CO_2 is lower beyond that O-C distance. Because we do not anticipate any CO_2 bond breaking as a result of interacting with ILs, this underestimation might be acceptable when the O-C distance in CO_2 is far away from its equilibrium bond length. The general trend of energy change as the O-C-O angle bends obtained with ReaxFF agrees with the trend predicted by DFT as indicated by Figure 4.11(b). ReaxFF will overestimate the energy of the O-C-O angle distortion from 130° to 170° by 10 kcal/mol at most while it will underestimate the energy by the same amount when the angle is less than 130°.

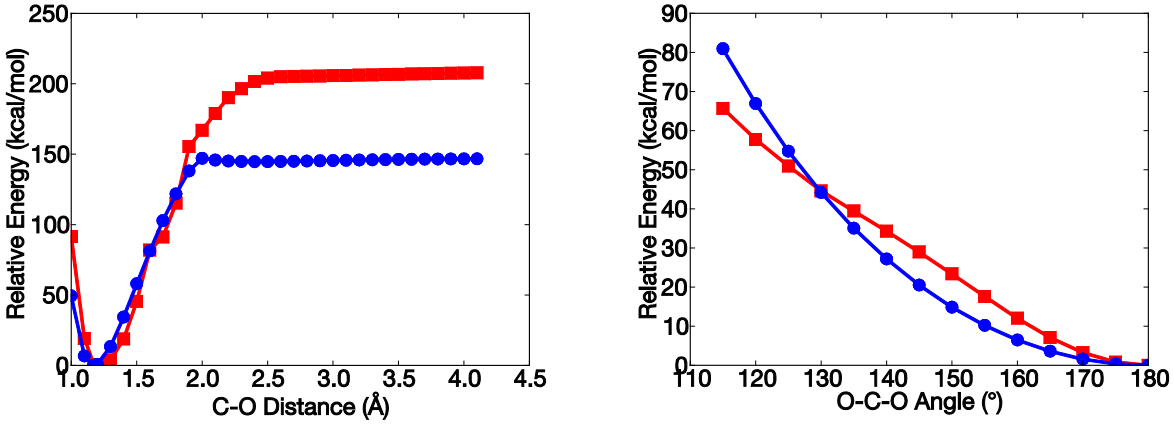

(a) (b)

Figure 4.11. Comparison of the DFT and ReaxFF relative energies of C-O bond dissociation (a) and O-C-O angle distortion (b) in CO_2 molecule. Blue circles: DFT energy; Red squares: ReaxFF energy. The DFT calculations were performed with one CO_2 molecule in Gaussian.

The energy profile of CO_2 approaching the N atom of the isolated anion has been calculated with DFT-D2 in Gaussian and ReaxFF as shown in Figure 4.12. The DFT-D2 result shows no barrier for CO_2 approaching the N atoms in anion until the C-N distance about 1.6 Å. However, even with this information built into the training set, the ReaxFF energies for the same sets of structures exhibits a barrier at about 2.3 Å. This may result in some problems in later simulations, since the reaction kinetics would be significantly slower for ReaxFF than one would expect from DFT data.

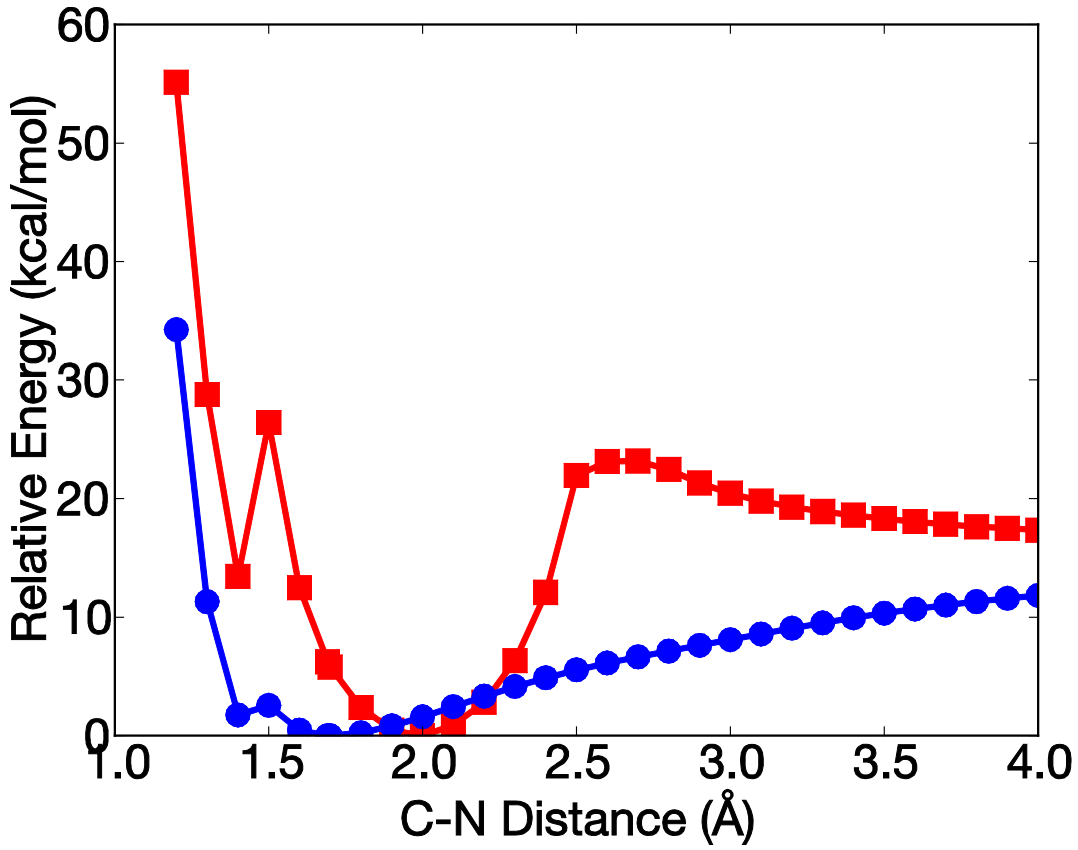

Figure 4.12. Comparison of the DFT and ReaxFF relative energies of C-N bond dissociation as CO_2 molecule leaving $[Gly]^-$ in gas phase. Blue circles: DFT energy; Red squares: ReaxFF energy. The DFT calculations were performed with Gaussian.

The pseudo EoS calculated with DFT-D2 in VASP for only 1 pair of pure $[P(C_4)_4][Gly]$ has also been added to the training set in the hope to improve the equilibrium volume calculation of $[P(C_4)_4][Gly]$. The comparison of pseudo EoS from DFT-D2 and ReaxFF is shown in Figure 4.13. The DFT-D2 predicts the equilibrium density should be around 1.0 g/cm^3 while the ReaxFF gives a density about 1.02 g/cm^3. Both values are deviate from experimental measured density at 300K, about 0.963 g/cm^3.[43] This may due to the finite size effects since we only used one pair of IL to accelerate the expensive DFT calculations.

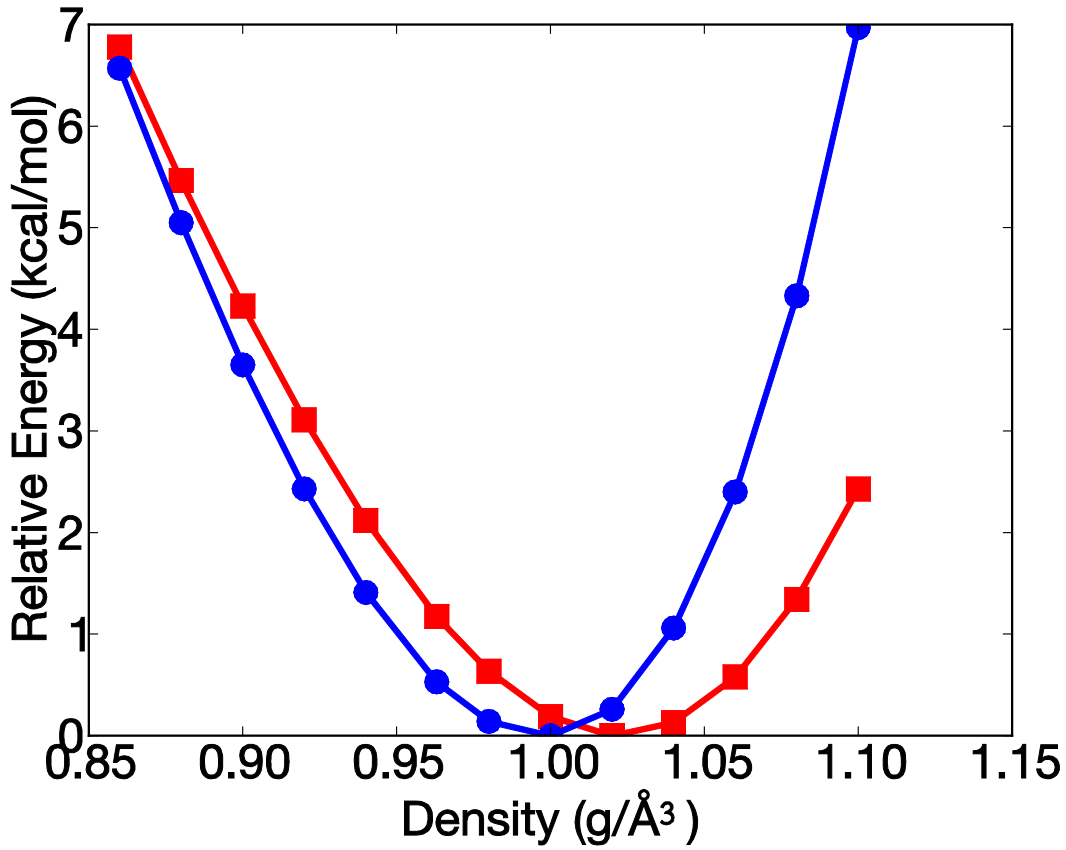

Figure 4.13. Comparison of the DFT and ReaxFF relative energies of pseudo EoS of pure $[P(C_4)_4][Gly]$. Blue circles: DFT energy; Red squares: ReaxFF energy. The DFT calculations were performed with VASP.

4.3.3 Molecular dynamic simulation of $[P(C_4)_4][Gly]$ and CO_2 system with ReaxFF

The average density calculated from *NpT* simulation with current force field of 50 pairs of ILs is about 1.20 g/cm^3. This number is higher than the experimental value (0.963 g/cm^3) and also the value (1.02 g/cm^3) obtained from pseudo EoS. This probably is due to the finite size effect since we only used one pair IL in the training set. We use the experimental density in all later simulations since the obtained density from *NpT* simulation is overestimated.

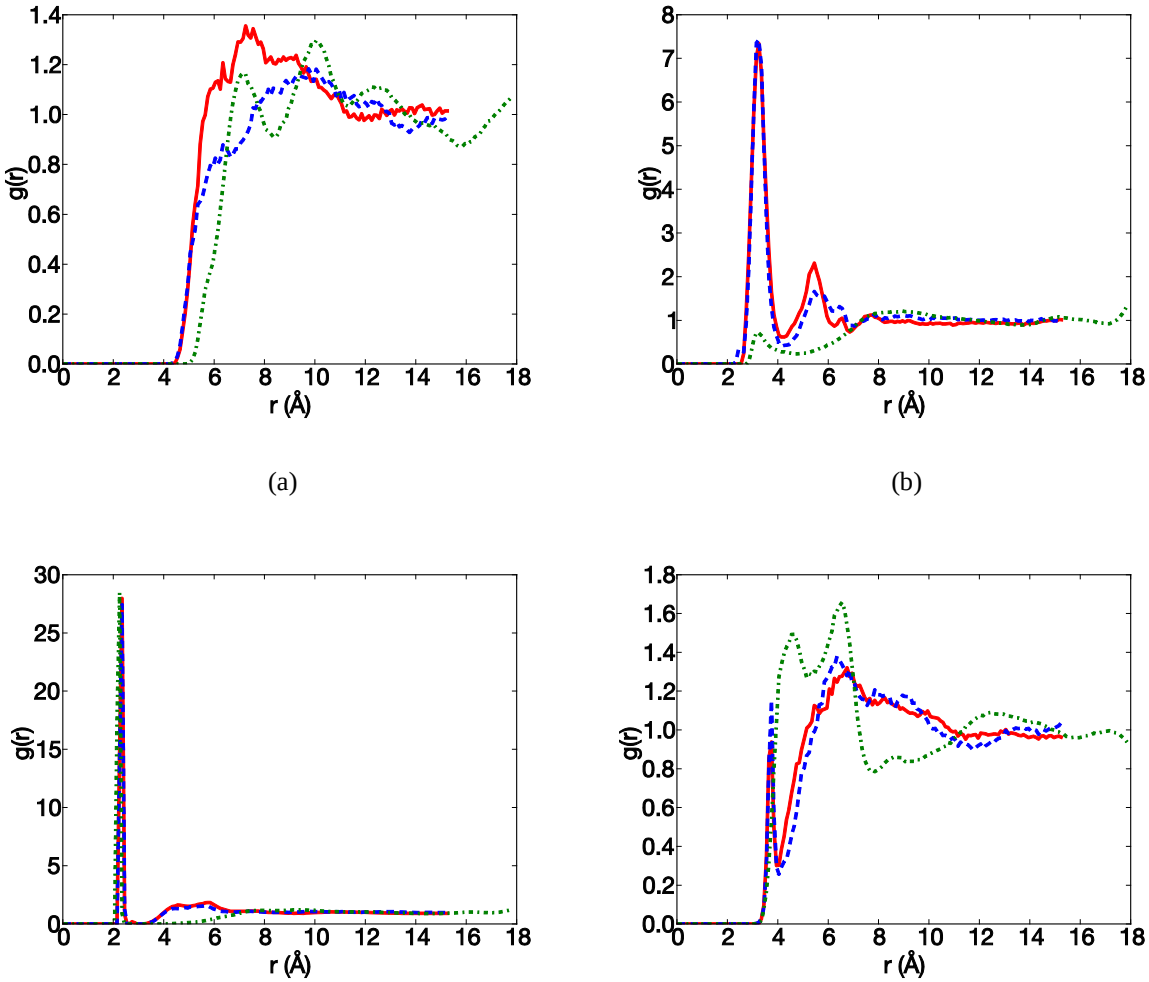

Figure 4.14. Site-site radial distribution function *g*(*r*) versus distance at 300 K. (a) cation-cation (P-P); (b) anion-anion (N-N); (c) anion-anion (O-O); (d) cation-anion (P-N); (e) cation-anion (P-O); For (a), (b), (c), (d) and (e), red solid line: $[P(C_4)_4][Gly]$ system with ReaxFF force field; blue dashed line: $[P(C_4)_4][Gly]$ and CO_2 system with ReaxFF force field; green dotted line: $[P(C_4)_4][Gly]$ system with classical force field. (f) CO_2-CO_2 (C-C, red solid line), CO_2-cation (C-P, blue dashed line), CO_2-anion (C-N, green dotted line), CO_2-anion (C-O, black dashed-dotted line) for IL with CO_2 systems.

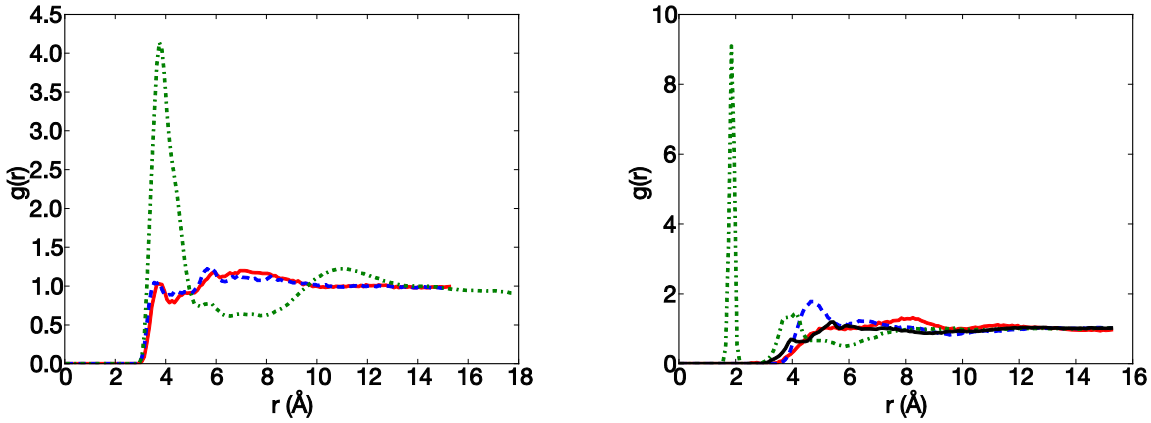

(e) (f)

Figure 4.14. Continued.

To better understand the microstructure of IL and CO_2 with IL, the radial distribution functions (RDF) of cation-cation, cation-anion, anion-anion, CO_2-CO_2, CO_2-cation, CO_2-anion of pure IL with ReaxFF force field or classical force field and IL with CO_2 system by ReaxFF force field are plotted in Figure 4.14. The cation-cation RDFs are represented by P-P atoms since P has the most of the positive charge in the cation. For the anion, the most negatively charged atoms are N from $–NH_2$ and O from carboxylic groups. Thus the N atom and O atoms from the anion are chosen to represent the anion. C atom is selected to characterize CO_2 molecule since it is the center atom of the CO_2 molecule. For the P-P site RDF, we can see that the pure ILs have a broad peak around 7 Å from ReaxFF force field while after reaction with CO_2, the peak shifted to larger separation around 9 Å. The shape of the P-P RDFs from ReaxFF is different from the RDF computed from classical potentials adapted from Ref. 192 where there are two peaks around 7 Å and 9.5 Å. The P-P site RDF from classical potential is in agreement with Refs. 192 and 193. As for the first peak, the ReaxFF MD results show a much smaller cation-cation minimum separation of about 4.3 Å than the result from classical potential which is around 5 Å.

The anion-anion RDFs of N-N sites and O-O sites show similarity in the shape of the curves from both ReaxFF and classical potentials. The first peak of N-N site RDF is slightly over 2 Å, while the peak heights from ReaxFF MD are much higher than the classical potential. There is another peak around 5.5 Å from ReaxFF MD, which does not appear in the RDF from classical potentials. The first peak in the O-O site RDF is mainly due to the carboxylic group hence the peak shape and height are nearly identical no matter which potential used. A secondary broad peak center around 3 Å can be found in the RDFs computed with the ReaxFF force field. There is a rather small difference between the RDFs of IL systems with or without CO_2. This implies that CO_2 does not significantly change the configuration of the anions. The cation-anion RDFs, as measured by the P-N and P-O site RDFs, have very different shapes computed from different force fields. There are two peaks centered around 3.9 Å and 6.5 Å in P-N site RDF from ReaxFF MD, while the two peaks are centered about 4.2 Å and 6.5 Å from the classical force field. The first peak is smaller and sharper as computed from ReaxFF compared with that calculated from classical potentials, but the second peak is much broader. There is one sharp and strong peak in the P-O site RDF around 4 Å, while a broad peak centered at about 11 Å can also be observed from MD with classical potentials. However, there are only two subtle peaks centered about 3.8 Å and 7 Å in the P-O site RDF computed from ReaxFF. The much closer first and second peaks of the P-N site RDF and strong and sharp peak around 4 Å of the P-O site RDF both by classical potentials indicate the anions tends to be ordered around the cations, while the anions seems more disordered as calculated from ReaxFF. The configurations of the cation-anion pair in IL do not seems to be largely influenced by CO_2, as indicated by small difference of both P-N and P-O RDFs for ILs with or without CO_2. Thus, it is interesting to see what the structure looks like when CO_2 dissolves in ILs. The CO_2-CO_2 RDF is represented by C-C atoms, the CO_2-cation

RDF is illustrated by C-P atoms. The CO_2-anion RDF can be represented by C-N and C-O (O from carboxylic group in the anion) RDFs. These are plotted in Figure 4.14(f). The CO_2 is strongly interacting with the anion mainly though the N atom, as indicated by the strong peak around 1.9 Å in the C-N site RDF. This is confirmed by the lack of significant peak in the C-O (O from anion) site RDF and is in accordance with the minimum energy pathway from the NEB calculations. However, there is essentially no CO_2 in the product state, as implied by the minimum in the C-N distance of 1.6 Å from the C-N site RDF, which corresponds to the reactant state. Besides the strong peak around 1.9 Å from C-N site RDF, another smaller bur broad peak appears at about 4 Å. Interestingly, CO_2 can also interact with cations as shown by the 4.5 Å peak in the C-P site RDF. Later hydrogen bond analysis will show a clearer picture of how CO_2 interacts with the cation.

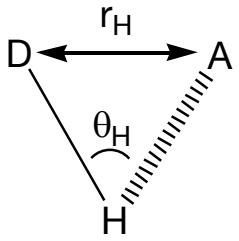

Figure 4.15. Hydrogen bond criteria. D is the donor atom. A is the acceptor atom. r_H is the distance between donor atom and acceptor atom. θ_H is the angle formed between D-H and A···H. To be considered as a hydrogen bond, r_H should be less than 3.3Å and θ_H must be larger than 145°.[181, 182]

The number of hydrogen bonds has been calculated for pure IL and IL interacting with CO_2 using the same criteria as used by Gutowski and Maggin[181] and Wu *et al.*[182] This definition is illustrated in Figure 4.15. The donor atoms can be any atoms with hydrogen attached while the acceptor atoms are limited to N atoms in anions, O atoms in anions, and O atoms from CO_2, if there are CO_2 species. The percentage of hydrogen bonds occupied is computed based on the assumption that one acceptor atom can only form one hydrogen bond. The percentage occupied

shown in Table 4.1. Compared with classical force field, more the hydrogen bonds are occupied for pure ILs with ReaxFF, especially for C-H···O (cation-anion) and N-H···O (anion-anion). One of the reasons that there are more hydrogen bonds formed is that at equilibrium the ILs with ReaxFF force field tend to be closer to each other compared to with classical force field. After reacted with CO_2, there are fewer C-H···N (cation-anion) and N-H···O (anion-anion), but more C-H···O (cation-anion) bonds forming. However, more cation-CO_2 hydrogen bonds formed compared with anion-CO_2 hydrogen bonds shows the competition of CO_2 among cations and anions favors the cations.

Table 4.1. Occupation percentages for different types of hydrogen bond.

Hydrogen Bond	Classical	ReaxFF	
	IL	IL	IL+CO_2
C-H···N(cation-anion)	2.5	14.3	11.5
C-H···O(cation-anion)	27.3	67.6	75.1
N-H···N(anion-anion)	1.5	4.4	4.1
N-H···O(anion-anion)	2.6	47.2	39.6
C-H···O(anion-CO_2)	0.0	0.0	1.1
C-H···O(cation-CO_2)	0.0	0.0	29.3
N-H···O(anion-CO_2)	0.0	0.0	12.1

Cation, anion, CO_2 in the parentheses indicates where the donor or acceptor atom is from.

As stated above, if there is no strong (chemical) interaction between CO_2 and IL, the CO_2 angle should be around its equilibrium of 180°. Based on the information from a previous minimum energy pathway calculation, if the IL with CO_2 is near its reactant state, the CO_2 angle is around 137° while the angle is about 123° when CO_2 already reacts with the IL to form products. Thus, we can use different CO_2 angles to tentatively characterize the different reaction stages of CO_2 with IL from MD simulations, as well as different interaction strengths. The interaction between CO_2 and IL should be stronger when CO_2 is in product state, like Figure

4.6(b), than that when CO_2 is in the reactant state, as shown in Figure 4.6(a). Therefore, we plotted the CO_2 angle distribution (O-C-O angle) of $[P(C_4)_4][Gly]$ interacting with CO_2 using the ReaxFF force field in Figure 4.16. Another two distributions of CO_2 angle with different initial configurations from DFT-D2 MD simulations are added for comparison. Since the MD simulations with DFT-D2 is really expensive, we only used two pairs of ILs with two CO_2 and the total simulation time is merely 20 ps. One DFT-D2 result show that CO_2 mainly kept unreacted since the only peak of its angle distribution is around 175° (see Figure 4.16 blue curve) whereas there are three peaks around the 170°, 138°, 125° for the other DFT-D2 MD (see Figure 4.16 green curve), clearly showing that they are in non-interacting, reactants, products stage. The different shapes of these CO_2 angle distributions from DFT-D2 vary dependent on the different initial configurations because of the limited number of molecules studied and limited simulation time. We can see that for the former DFT-D2 simulation, the smallest CO_2 angle is around 140° where CO_2 is just about to react with the IL but it does not have enough time to overcome the reaction barrier to product stage. The CO_2 angle distribution from ReaxFF MD simulations (see Figure 4.16 red curve) does have similar shape as the DFT-D2 results but with different weights of different reaction stages. There is a stronger peak around 178° than the DFT-D2 MD results which indicates lots of non-interacting CO_2 present. The smaller peak near 140° is the signal of CO_2 in the reactant stage weakly interacting with IL and has similar shape as one of DFT-D2 MD results (see Figure 4.16 green curve). There is only very small amount of strongly interacting CO_2 in product stage as the CO_2 angle distribution curve from ReaxFF MD only expand to around 128°. This is in accordance with RDF of CO_2-anion which shows the minimum distance between C atom in CO_2 with N atom in [Gly]- is around 1.6 Å as illustrated in Figure 4.14(f). However, this is unexpected since there are much more molecules (50 pairs of IL with

50 CO_2) and longer simulation time (0.5 ns) in the ReaxFF MD simulation than the DFT-D2 MD. Thus there should have more CO_2 to overcome the barrier to reach product stage. This probably can be attributed to the overestimation of the first barrier shown in Figure 4.8 and unexpected barrier around 2.3 Å in Figure 4.12.

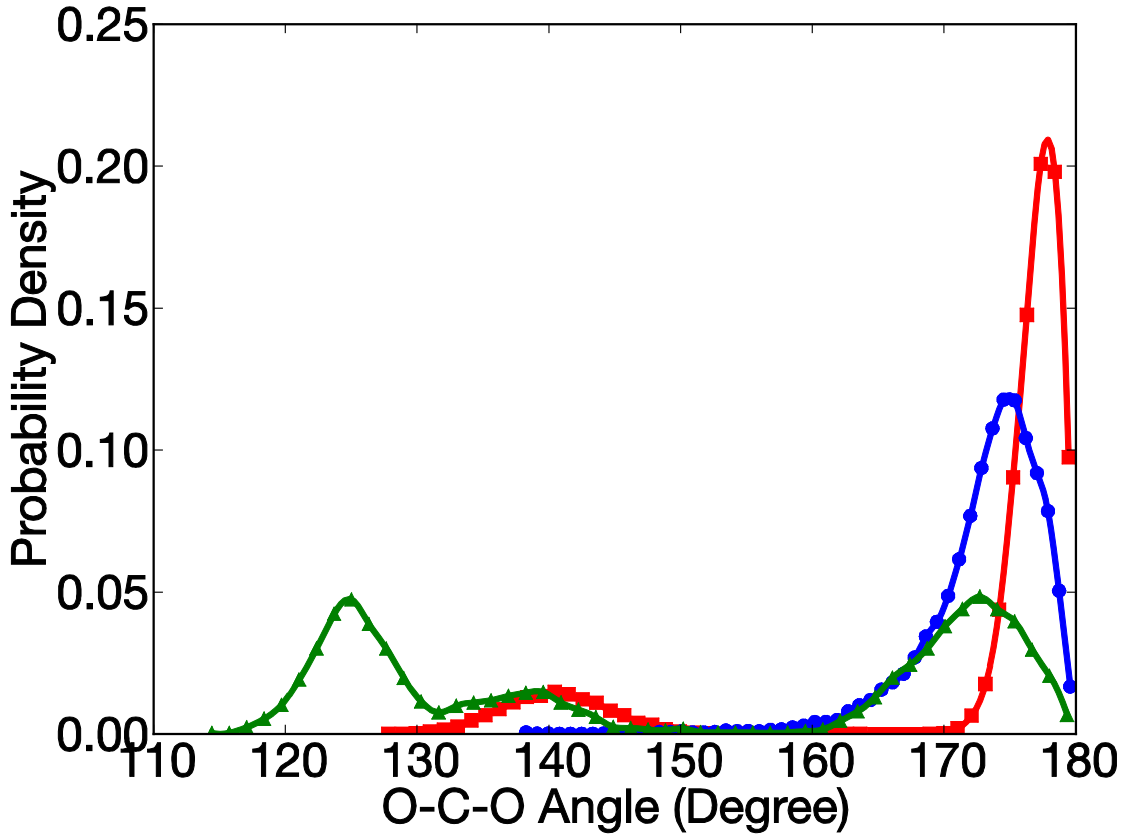

Figure 4.16. CO_2 angle distribution calculated with ReaxFF force field (red squares) and DFT-D2 at PBE level (blue circles and green triangles).

4.4 CONCLUSION

We have obtained a minimum energy pathway for tetrabutylphosphonium glycinate ($[P(C_4)_4][Gly]$) reaction with CO_2 at the PBE/DFT-D2 level of theory with the NEB method, as

implemented in VASP. There are two energy barriers of 0.7 kcal/mol and 2 kcal/mol respectively, to reach the final products. The first step involves proton transfer from the N atom in $[Gly]^-$ to one of the O atoms in the carboxylic group in $[Gly]^-$. The next step involves movement of the proton to a position where it is shared by the O atom from CO_2 and the O atom from the carboxylic group in the anion. A ReaxFF force field was developed based on the minimum energy pathway and other configurational energetics, as well as a pseudo EoS data for $[P(C_4)_4][Gly]$. The force field has been validated and generally good agreement can be found between the energies calculated from DFT with vdW correction and the energies computed by ReaxFF with nearly same structures. Finally, the optimized force field has been used for in large-scale molecular dynamics simulation to study the reactions between $[P(C_4)_4][Gly]$ and CO_2. RDF of cation-cation, caion-anion show that the configurations of ILs are hardly influence by CO_2. RDF of CO_2-anion shows CO_2 mainly interacting with anion through $–NH_2$ group. Hydrogen bond analysis and RDFs indicate competition between cation and anion for CO_2 through hydrogen bonds. CO_2 angle distribution from ReaxFF MD shows most CO_2 are not interacting with IL or are weakly interacting with IL. But only very small amount of strongly interacting CO_2 can be found which is in contrast to DFT MD simulations.

5.0 DENSITY FUNCTIONAL THEORY STUDY OF THE WEAKLY BOUND ADSORBED MOLECULAR OXYGEN SPECIES ON TiO_2(110) SURFACE

The Content of this chapter is taken from Bo Zhang, and J Karl Johnson, "Density functional theory study of the weakly bound adsorbed molecular oxygen species on TiO_2(110) surface", in preparation.

5.1 INTRODUCTION

TiO_2 has long been used as catalysts[50, 51] and supports for many other oxides, such as Au,[52, 53] and Pd[203, 204] in photo-oxidation reactions. Rutile TiO_2(110) surface is most studied surface because it is most stable and it is readily available in the form of high quality single crystal.[54] There have been many studies of O_2 adsorption on TiO_2(110) surfaces through experiments and theoretical simulations. The adsorption of O_2 can be classified as two types: dissociative adsorption and molecular adsorption. Many studies show that oxygen will heal the bridging oxygen vacancy by dissociation down to 120K while the other oxygen adatom will be on top of the adjacent five-fold Ti atom.[205, 206] This is also supported by a number of theoretical studies.[59, 207] Yates *et al*. found two molecular chemisorption states for O_2 on the TiO_2(110) surface which were denoted α and β states.[55-57] They are characterized by distinct photoactivity. The α-O_2 can

be photoactivated to oxidize the CO and slowly photodesorb while the β-O2 only undergoes fast photodesorption.[55-57] The α-O_2 can be converted to β-O_2 by heating above 200K.[55-57] Molecular oxygen can also adsorb on the TiO_2(110) surface with the support of the OH group dissociated from pre-adsorbed water.[208]

Henderson *et al*. explored the interaction of molecular oxygen with the TiO_2(110) surface.[209] They found that the number of O_2 molecules adsorbed on the surface is up to three times of the number of bridging oxygen vacancies.[209] This suggests that some extra oxygens will likely be adsorbed on the five-fold Ti atom adjacent to the filled bridging oxygen vacancy.[209] Wendt *et al*. also pointed out that some other sites than the bridging oxygen vacancy are responsible for the adsorption of molecular oxygen which will desorb at 410 K observed by Henderson and co-workers[209] because of the dissociative adsorption of O_2 can heal the vacancy.[206] Schaub *et al*. studied the diffusion of oxygen vacancies on the TiO_2(110) surface, and found that O_2 molecule can adsorb above the five-fold Ti atoms on the surface where is relatively far from a vacancy.[210] These findings imply that the five-fold Ti atom, which is in an environment more like the stoichiometric surfaces, will also be attractive to molecular oxygen species though the adsorption would be really weak and more physical in nature. Dohnalek *et al*. measured the desorption energy of physically adsorbed molecular O_2 on the fully oxidized TiO_2(110) surface as a function of O_2 coverage at temperatures as low as 32 K and found the O_2 binding energy varying from -9.8 to -18 kJ/mol with respect to coverage from 1.5 monolayer (ML) extrapolated to 0 ML.[211] On the TiO_2(110) with a low concentration of oxygen vacancy, Cui *et al*. found that the O_2 molecule can physically adsorbed down to 80 K after exposure to large amount of O_2 at room temperature.[212] The physical adsorption site of O_2 molecule is found to be on top of the five-fold Ti atom on the surface through directly imaging by high-resolution

scanning tunneling microscope.[212] A recent study shows that weakly adsorbed O_2 molecule on the TiO_2 surfaces are probably the precursors to photo-active O_2 molecules and the transformation process will likely be the first step of the elementary reactions.[67] The infrared (IR) inactive O_2 molecule becomes weakly IR active during its adsorption to the TiO_2 surface while maintaining its "molecular" nature.[67] This may be caused by the small distortion of its dipole moment by the adjacent TiO_2 surface. The measured enthalpy of adsorption is in the range of -16 to -21 kJ/mol[67] from high coverage to low coverage. This is in good agreement with measurements by Dohnalek *et al*.[211] These binding energies are much smaller than that of chemical adsorption on the bridging oxygen vacancy (typically of hundreds of kJ/mol[59, 207]).

In this chapter, the geometry and adsorption energy of O_2 on the TiO_2(110) surface will be thoroughly studied by DFT methods with vdW corrections. The IR frequency and intensity of the weakly adsorbed O_2 of rutile TiO_2(110) surface will be also studied. Finally, a tentative explanation will be given through electric field created by the TiO_2(110) surfaces and induced charge density differences.

5.2 COMPUTATIONAL DETAILS

All calculations in this work were performed with the Vienna *ab-initio* simulation package (VASP),[90-93] which is a periodic plane-wave DFT code. Core-electron interactions were described by projector augmented-wave (PAW) potentials.[94, 95] We used generalized gradient approximation (GGA) exchange-correlation functionals, particularly, PBE of Perdew, Burke and Ernzerhof.[28, 29] A plane-wave basis cutoff energy of 520 eV was used for all calculations. We performed geometry relaxation of chosen atomic positions, cell shape, and cell volume using a

stopping criterion of energy less than 0.1 meV and force less than 0.03 eV/Å. The conjugate gradient algorithm was used in conjunction with the PBE functional. Spin polarized calculations were performed for systems containing O_2. The spin state of O_2 was found to be triplet in all calculations. It is well known that standard implementations of DFT cannot properly describe the long-range electron correlations that represent the dispersion (van der Waals) interaction due to its local or semi-local character.[8] Various methods have been proposed to overcome this shortcoming of DFT.[60-66] DFT-D2 is one of the simplest and empirical methods which introduces an additional dispersion energy term to the Kohn-Sham energy to recover most of the dispersion interaction.[61] This dispersion energy term can be calculated as[61]

$$E_{\text{disp}} = -s_6 \sum_{i=1}^{N_{\text{at}}-1} \sum_{j=i+1}^{N_{\text{at}}} \frac{C_6^{ij}}{R_{ij}^6} f_{\text{dmp}}\left(R_{ij}\right), \tag{5.1}$$

where N_{at} is the number of atoms in the system, C_6^{ij} is the dispersion coefficient for atom pair *ij*, s_6 is the global scaling factor that only depends on the functional used, and R_{ij} is the interatomic distance. f_{dmp} is the damping function which can be written as $f_{\text{dmp}} = \frac{1}{1+e^{-d\left(R_{ij}/R_r-1\right)}}$ where R_r is the sum of atomic vdW radii.

The initial TiO_2 crystal structures (rutile form) are taken from inorganic crystal structure database.[88] They are then fully relaxed to the ground state. In this stage, only one unitcell are considered. The k-point meshes were generated using the Monkhorst-Pack method[98] with a spacing of around 0.027 $Å^{-1}$ between two k-points along the axes of the reciprocal unit cells. Based on fully relaxed TiO_2 rutile structure, (100), (110), (001) surfaces are built to satisfy that the surface is charge neutral and no net dipole moment.[54, 213] Each surface is built with a (2×2) supercell and only bottom three atomic layers are fixed (see Figure 5.1). The vacuum gap is 15Å. The k-point meshes is kept the same as the bulk calculations for cell dimensions that are periodic

while the k-point is set to be 1 for the cell dimension along which vacuum space is added. The surfaces were fully relaxed to the ground state and the (110) surface has lowest energy. Thus it is considered as the most stable surface and used in our all calculations. The ground state of O_2 adsorption on TiO_2(110) surface is calculated by fully relaxing the structure except that the bottom three atomic layers are fixed. The coverage of O_2 molecule is 0.25 ML. The adsorption energies of O_2 on TiO_2(110) surface with respect to different angle θ and φ are calculated by optimizing the O_2 atomic positions only in z direction and also fully relaxing top six atomic layers of the surface. θ and φ are running through from 0° to 90° and other angles data can be obtained by symmetry. The adsorption energy is calculated as

$$\Delta E_{\text{adsorption}} = E_{O_2+TiO_2} - E_{O_2} - E_{TiO_2}. \tag{5.2}$$

The infrared frequency and intensity calculations are calculated with lattice dynamics via finite difference approach. Since O_2 molecules are physically adsorbed on the TiO_2 surfaces as indicated by experiments and our calculations, we only displace O_2 molecule itself instead of displacing the whole O_2-TiO_2(110) system to avoid expensive calculations. Due to the periodicity of crystal, the classic definition of dipole moment (which is the product of magnitude of charge and the distances of separation between the charges) is problematic. Therefore the berry phase approach[214-216] is used to calculate the ionic dipole moment and also the electronic dipole moment. The total dipole moment of the periodic system is the sum of the ionic and electronic dipole moment, which is equivalent to the classic dipole moment. The frequency of the infrared spectrum can be computed within harmonic approximation by solving the eigenvalues of following equation,[217]

$$Hu_i = \lambda_i u_i, \tag{5.3}$$

where the mass weighted Hessian matrix H is constructed by finite difference method of only displaced atoms as

$$H = \begin{Bmatrix} \frac{\partial^2 E}{m_1 \partial x_1^2} & \frac{\partial^2 E}{m_1 \partial x_1 \partial y_1} & \cdots & \frac{\partial^2 E}{\sqrt{m_1 m_N}\partial x_1 \partial z_N} \\ \frac{\partial^2 E}{m_1 \partial y_1 \partial x_1} & \frac{\partial^2 E}{m_1 \partial y_1^2} & \cdots & \frac{\partial^2 E}{\sqrt{m_1 m_N}\partial y_1 \partial z_N} \\ \vdots & \vdots & \ddots & \vdots \\ \frac{\partial^2 E}{\sqrt{m_N m_1}\partial z_N \partial x_1} & \frac{\partial^2 E}{\sqrt{m_N m_1}\partial z_N \partial y_1} & \cdots & \frac{\partial^2 E}{m_N \partial z_N^2} \end{Bmatrix}. \quad (5.4)$$

In Eq.(5.4), N is the number of displaced atoms, u_i is the *i*th eigenvector, m_n is the mass of the *n*th atom. By solving the Eq.(5.3), we can obtain λ_i which can be related with vibrational frequency as $\lambda_i = (2\pi\nu_i)^2$ where ν_i is the frequency of the *i*th vibrational mode.

The intensity of the infrared spectrum can be calculated with following expression[217]

$$I_i^{IR} = \frac{\mathcal{N}\pi}{3c}\left|\frac{d\mu}{dQ_i}\right|^2, \quad (5.5)$$

where $\mathcal{N}$ is the particle density, c is the velocity of light, μ is the total dipole moment from berry phase calculation, Q_i is the normal-mode coordinate that can be related with eigenvector u_i from Eq.(5.3) by

$$d_i = Q_i u_i \quad (5.6)$$

where d_i is the displacement.

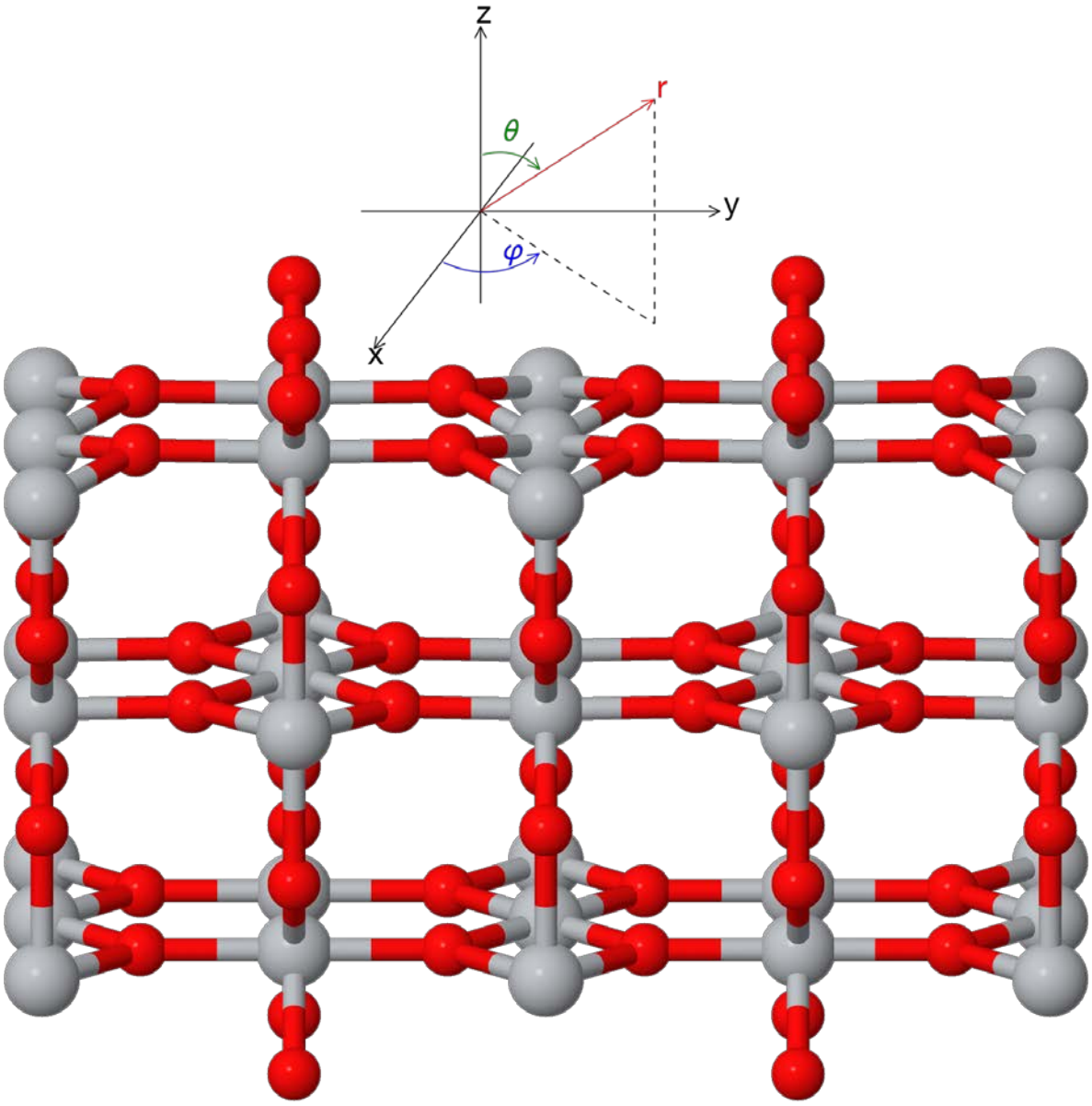

Figure 5.1. TiO_2(110) surface after relaxation with DFT and an illustration of the spherical coordinates on the surface used later.

5.3 RESULTS AND DISCUSSION

5.3.1 Ground state energetic and geometry of O_2 weak adsorption on TiO_2(110) surfaces

We relaxed several structures of O_2 adsorbed on TiO_2 and found the one in Figure 5.2 has the lowest adsorption energy. The energy and relevant geometry are listed in Table 5.1. The geometries after relaxation with DFT or DFT-D2 methods are very similar. The O-Ti distance obtained from DFT-D2 relaxation is only 0.2 Å (0.8%) closer to the surface than the one calculated from DFT method. While the angle θ is only 0.6 degree off that is negligible. Though the geometry is similar from two different methods, the adsorption energy computed with DFT-D2 method is much lower than DFT energy by about 12 kJ/mol. The adsorption energy from DFT-D2, -21.77 kJ/mol, agrees well with the experiment measured -16 to -21 kJ/mol from high coverage to low coverage.[67] This value is slightly higher than the -16.3 kJ/mol binding energy for physically adsorbed O_2 extrapolated to coverage of 0.25ML from the data in reference.[211] The error of about 5 kJ/mol is acceptable. The adsorption should be considered as physical adsorption in nature since the adsorption energy is much smaller than the adsorption energy of chemically adsorbed O_2 and most of the adsorption energy are contributed by vdW interaction. DFT with vdW correction recovered most long-range dispersion contribution to adsorption energy which is important for O_2 being weakly adsorbed on the TiO_2(110) surfaces.

Table 5.1. Energy and relevant geometry after relaxation with DFT or DFT-D2.

DFT			DFT-D2		
Adsorption Energy (kJ/mol)	O-Ti Distance (Å)	O-O-Ti Angle	Adsorption Energy (kJ/mol)	O-Ti Distance (Å)	O-O-Ti Angle
-8.04	2.866	50.4	-21.77	2.642	55.1

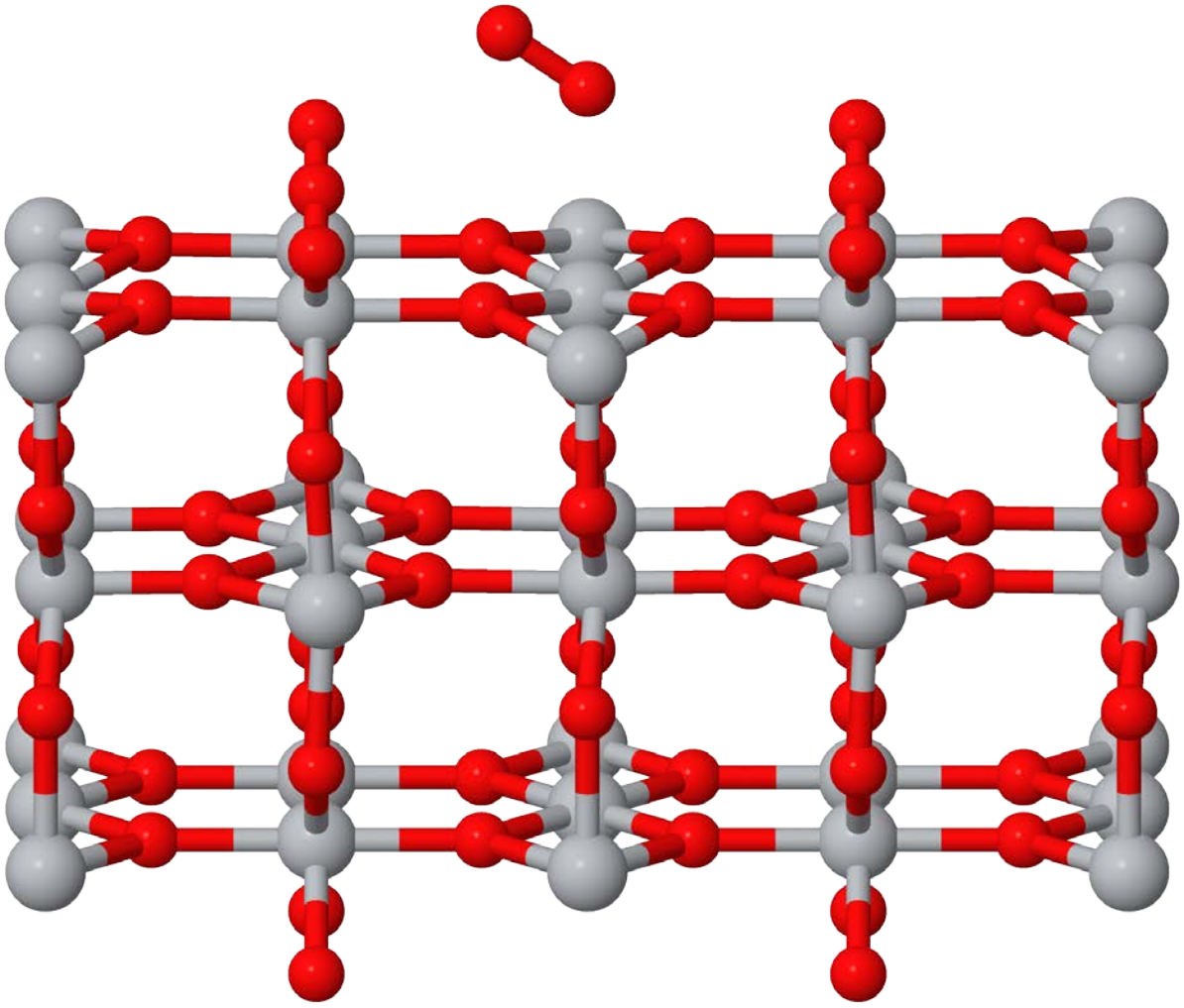

Figure 5.2. O_2 adsorbed on the TiO_2(110) surface.

5.3.2 Adsorption energy surface of O_2 weakly adsorbed on the TiO_2(110) surfaces

The adsorption energy with vdW correction at different orientation/angle of O_2 molecule on TiO_2(110) surface are investigated by fix θ and φ in spherical coordinates illustrated in Figure 5.1. Figure 5.3 shows the adsorption energy with vdW correction as a function of θ and φ. The adsorption energy of O_2 molecule on TiO_2(110) surface differs only in terms of θ, but rather not too much difference with respect to φ when θ is fixed. The lowest adsorption energy of -17.4 kJ/mol can be observed when $\theta \approx 60°$. There are also two peaks when $\theta \approx 0°$ or $\theta \approx 90°$. Figure 5.4 clearly shows that without vdW correction, the positive adsorption energies at almost all angles θ and φ indicates that the adsorption of O_2 is unfavorable from thermodynamic perspective. However, with vdW correction, the adsorption energies of O_2 on TiO_2(110) surfaces becomes negative at all angles θ and φ that result in the O_2 physical adsorption on the surface. When angle θ is fixed, the adsorption energy with vdW correction is almost isotropic with respect to φ with a few exceptions also illustrated in Figure 5.4. That differences of adsorption energies with vdW correction increase when the angle θ goes from 0° to 90° or -90°. When $\theta \approx$ 90° or $\theta \approx$ -90°, a largest about 2 kJ/mol difference can be observed between φ = 0° and φ = 45° or φ = 90°. Nevertheless, the difference around the biggest negative adsorption energy with vdW correction are quite small, only 0.2 kJ/mol when $\theta \approx 60°$ or $\theta \approx -60°$. From thermodynamic point of view, the O_2 molecule would be likely to reside around Ti center with an angle $\theta \approx 60°$ or equivalent $\theta \approx -60°$ as depicted in Figure 5.2. We can also roughly estimate the rotational barrier from Figure 5.4. A bigger barrier about 10 kJ/mol can be observed to when θ goes from 60° to about 90° and a smaller one about 7 kJ/mol can be found to go from $\theta \approx -60°$ to $\theta \approx 0°$.

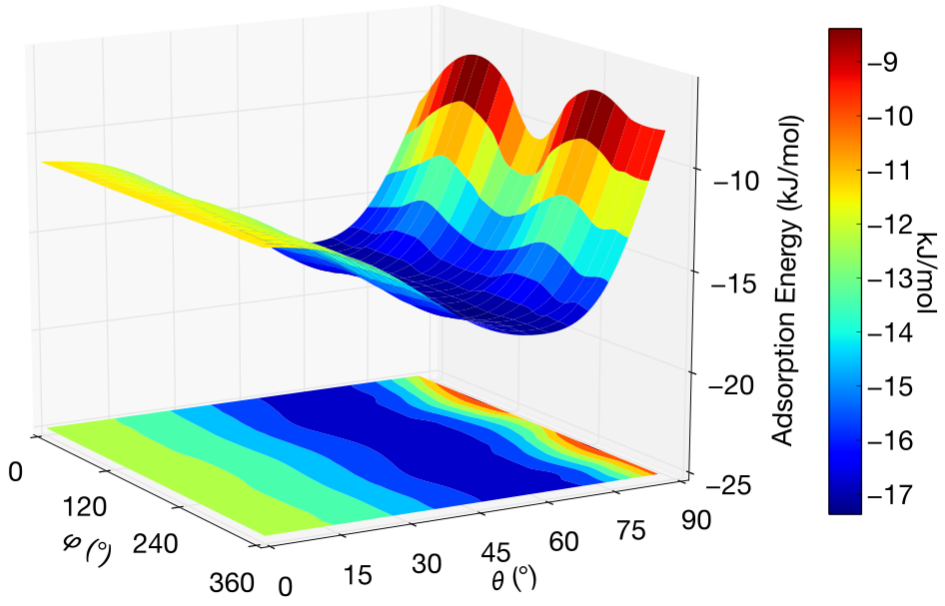

Figure 5.3. The adsorption energy as a function of angle θ and φ.

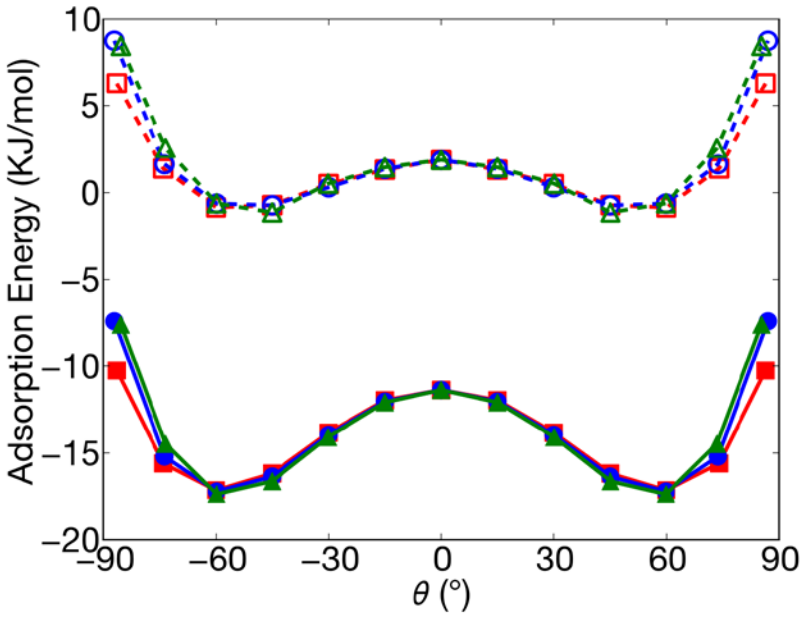

Figure 5.4. The adsorption energy profile as a function of angle θ. Solid lines with filled symbol are calculated with DFT-D2; Dashed lines with empty symbol are calculated with DFT; Red: φ = 0°; Blue: φ = 45°; Green: φ = 90°.

Figure 5.5 shows an interesting correlation between the adsorption energy of O_2 on TiO_2(110) surface with the distance from the lowest oxygen atom to its nearest Ti atom (O-Ti distance). The O-Ti distance is also not sensitive to the angle φ but dependent on the angle θ as the adsorption energy of O_2 on TiO_2(110) surfaces. The curves of optimized O-Ti distances has maximum where adsorption energy with vdW correction curve has maximum, though their minimum locations are not the same but very close. Thus, the O-Ti distances can likely be correlated with the adsorption energy of O_2 on TiO_2(110) surfaces at any θ angle albeit some discrepancy. The adsorption energy is largest about $\theta \approx$ -60° or 60° while the O-Ti distances is shortest around $\theta \approx$ -45° or 45°. Figure 5.6 shows adsorption energy of O_2 on TiO_2(110) surfaces and the O_2 bond length as function of θ and φ. Similarly to adsorption energy of O_2 on TiO_2(110) surfaces as well as the O-Ti distances shown previously, the bond length of O_2 molecule adsorbed on TiO_2(110) surface is independent to angle φ but largely influenced by angle θ. Although the adsorption energy will have a secondary maximum around $\theta \approx$ 0°, the O_2 bond lengths are rather no difference at the same angles. While θ goes from roughly 45° to 90° or -45° to -90°, the O_2 bond lengths increase as well as the O_2 adsorption energy in the similar trends. Eichler *et al*. also observed similar trends of O_2 bond length increases as the adsorption energy increases for O_2 molecule adsorbed on Pt(111) surfaces.[218] This implies that the adsorption energy will largely depend on the O-Ti distances especially when θ from -45° to 45°, whereas O-Ti distance and O_2 bond length both contributes to the adsorption energy when θ from -45° to -90° or from 45° to 90°.

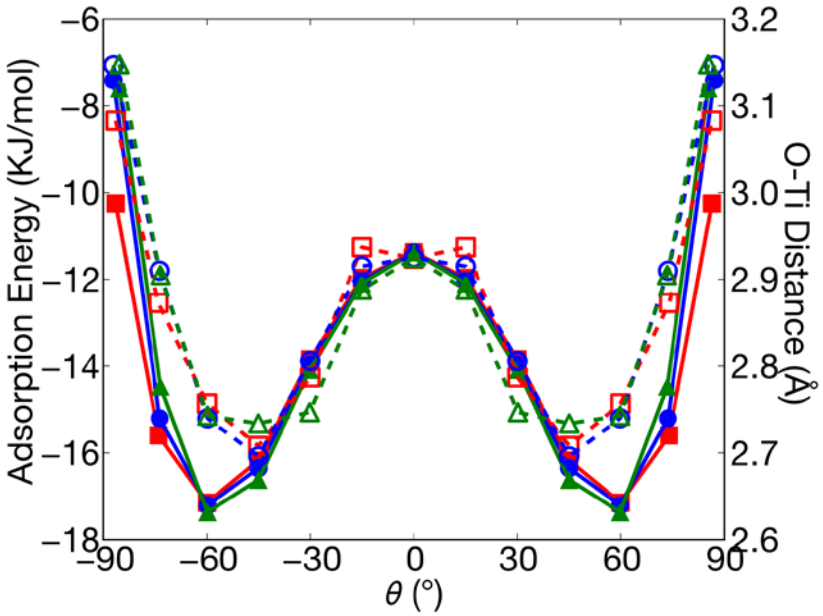

Figure 5.5. Correlation between adsorption energy with vdW correction and O-Ti distances at different φ angle. Solid line filled symbol: adsorption energy with vdW correction; Dashed line open symbol: distance between lowest O atom in O_2 and nearest Ti atom to that O atom on the surface; Red: φ = 0°; Blue: φ = 45°; Green: φ = 90°.

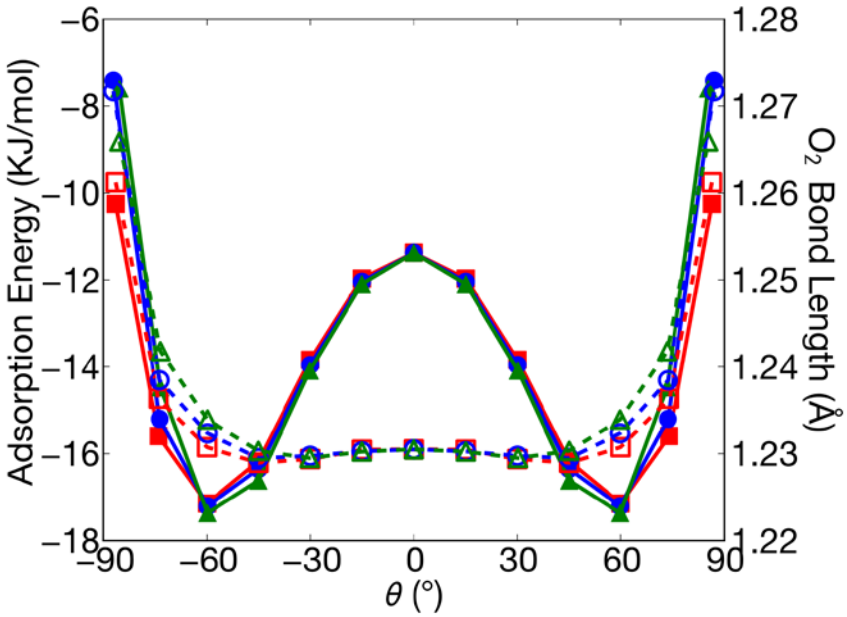

Figure 5.6. Correlation between adsorption energy with vdW correction and O_2 bond length at different φ angle. Solid line filled symbol: adsorption energy with vdW correction; Dashed line open symbol: O_2 bond length; Red: φ = 0°; Blue: φ = 45°; Green: φ = 90°.

5.3.3 Infrared spectra calculation

Based on previous described procedure, we can calculate the infrared frequency and the intensity of the peak within harmonic approximation which may be little off from real observed frequency due to anharmonic effect (as large as 20 cm^{-1} difference[219]). The calculated frequency, intensity and pertinent geometry parameter as listed in Table 5.2. For the pure gas phase O_2 molecule, the relaxed structure of O_2 (bond length) are the same and the computed vibrational frequencies are also the same with or without vdW correction. The vdW interaction thus will not be as important as in the adsorption energy calculations. Furthermore, the zero intensity from our calculation indicates that peak is IR inactive which is known experimentally. However, compared with experiments, the calculated frequency is about 12 cm^{-1} higher and the bond length is about 0.026 Å longer. We know that the infrared frequency calculation is sensitive to the pertinent geometry parameter (normal coordinates), in our case, the O_2 bond length as indicated in Eq.(5.6). For the O_2 adsorbed on the TiO_2(110) surfaces, we have done infrared calculations withy several slightly different stable surface structures (the adsorption energies with vdW correction are in the experimental ranges). However, the O_2 bond lengths are not the same and then some of the calculated frequencies are slightly away from pure O_2 gas phase while some is similar to. For example, the structure (Table 5.2 #4) depicted in Figure 5.2 has a frequency of 1549.4 cm^{-1} through DFT-D2 calculation, which is luckily close to 1550 cm^{-1} from experiments.[67] But this value is almost 16 cm^{-1} lower than the one calculated for pure O_2 gas phase. This may be exceeding the errors. Nevertheless, the infrared calculation of stable O_2 adsorbed on TiO_2(110) surfaces give positive intensity at the peak around 1550 cm^{-1}, although the values are varying quite a lot. That indicates the infrared inactive peak becomes active after O_2 adsorbed on

TiO_2(110) surfaces. This agrees well with experimental observations that O_2 vibrational peak becoming infrared active when O_2 are weakly bound to the TiO_2(110) surfaces.[67]

Table 5.2. Infrared frequency and intensity of O_2 molecule adsorbed on TiO_2(110) surface and pertinent geometry parameters. O_2 (gas) denotes the O_2 in the gas phase; O_2 (surf.) denotes the O_2 weakly adsorded on the TiO_2(110) surface. O-Ti distance is the distance between lowest O atom in O_2 molecule and its nearest Ti atom on the surface.

No.	Structure	Method	Frequency (cm^{-1})	Intensity (km/mol)	O=O Bond Length (Å)	O-Ti Distance (Å)	θ (°)
1	O_2 (gas)	expt.	1554.7[a]	0	1.207[b]		
2	O_2 (gas)	DFT-D2	1566.1	0	1.233		
3	O_2 (surf.)	expt.	1550[c]	slight	n.a.		
4	O_2 (surf.)	DFT-D2	1549.4	5.15	1.232	2.642	55.1
5	O_2 (surf.)	DFT-D2	1554.4	0.04	1.235	3.887	62.4
6	O_2 (surf.)	DFT-D2	1563.8	0.04	1.233	3.887	62.4

[a]: obtained from Ref. 219.
[b]: obtained from Ref. 107.
[c]: obtained from Ref. 67.

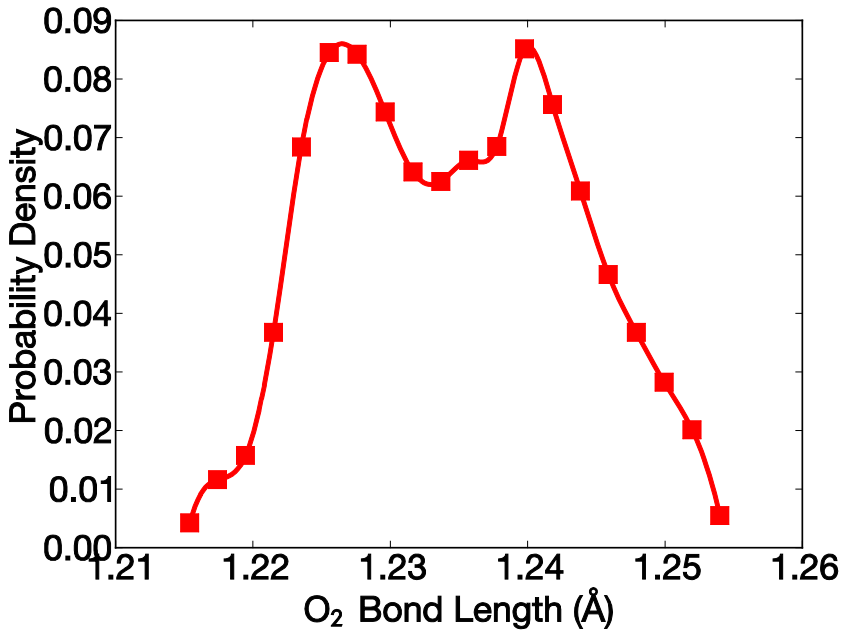

Figure 5.7. O_2 bond length profile from MD simulation.

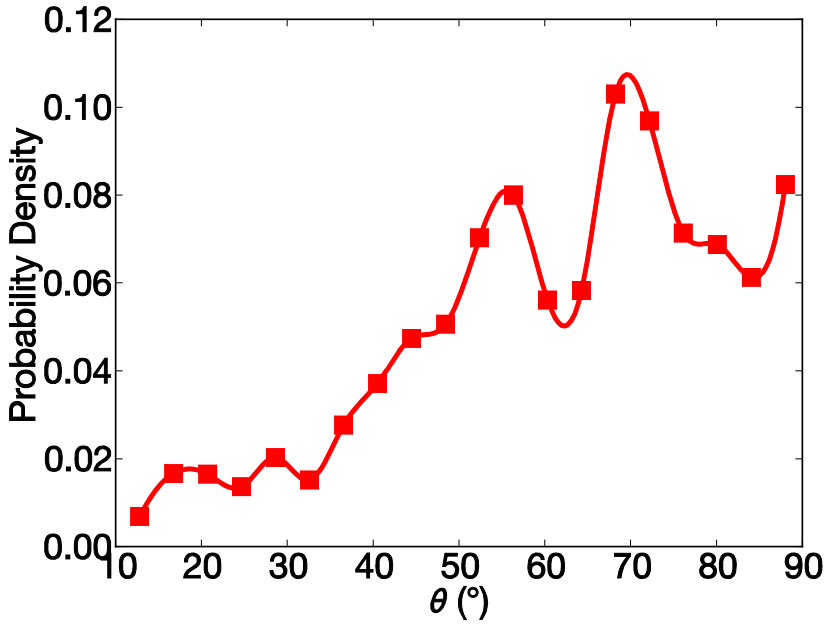

Figure 5.8. Angle θ profile from MD simulation.

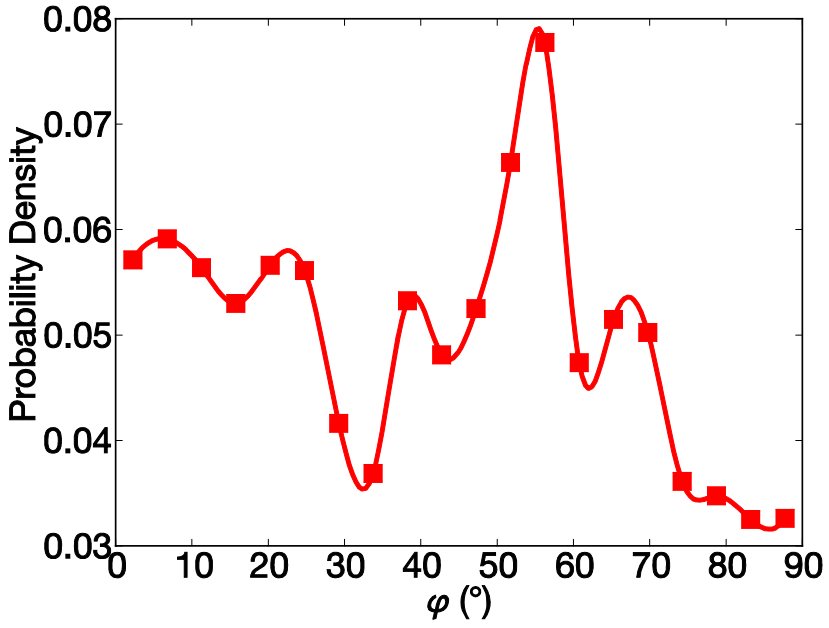

Figure 5.9. Angle φ profile from MD simulation.

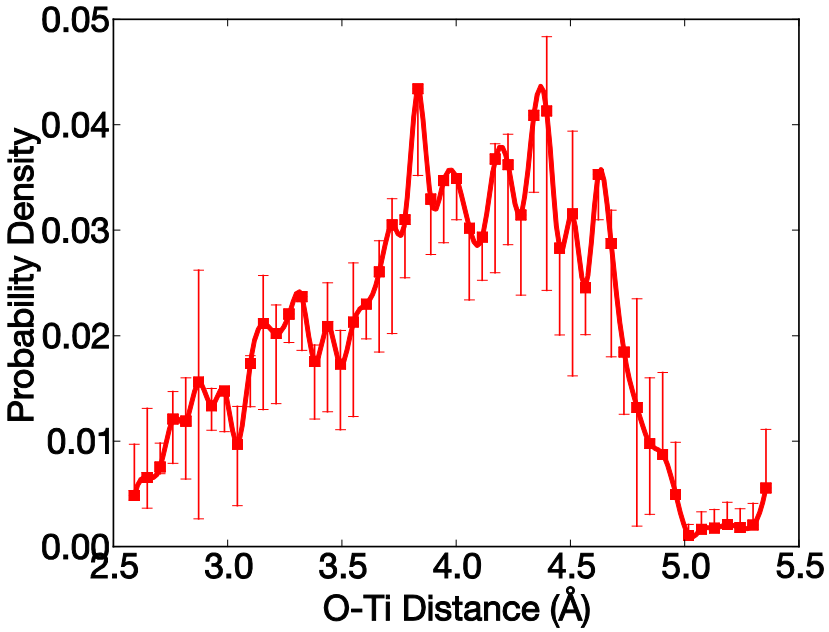

Figure 5.10. Average O-Ti distance profile from MD simulation. The curve is calculated by averaging the O-Ti of two O atoms from O_2 molecule, the error bars are then the standard deviations.

To achieve a better understanding of this observation, we did a molecular dynamics (MD) calculation with canonical ensemble (NVT) of O_2 on the TiO_2(110) surface. Figure 5.7-10 shows the profiles of O_2 bond length, angle θ, angle φ and O-Ti distances from MD simulation respectively. As can be seen from Figure 5.7, the O_2 bond length is ranging from 1.215 Å to 1.253 Å. There are two peaks around 1.228 Å and 1.239 Å indicating that the most probable O_2 bond length. Interestingly, there are also two peaks can be found in Figure 5.8 which depicts the distribution of angle θ during MD simulation. Those are one peak around 70° and the other peak about 55°. As indicated in Figure 5.4, the maximum of the adsorption energy of O_2 on TiO_2(110) surface is around 60°. Thus it is not surprise that the two most probable angle θ in the MD simulation are close to 60° where the adsorption energy is largest. Those observations prompt us that the bimodal behavior of O_2 bond length and angle θ probably can be related. We can read from Figure 5.6 that when θ is around 70°, the O_2 bond length can be ranging from 1.234 Å to

1.238 Å. The O_2 bond length will be 1.229 Å to 1.233 Å when θ is around 55°. This agrees with the two most probable that O_2 bond length seen from Figure 5.7. Thus, we can assign the two most probable configurations of O_2 bond length and angle θ combination. One is that the O_2 bond length will be 1.239 Å when $\theta \approx 70°$ and the other is that the O_2 bond length will be 1.228 Å when $\theta \approx 55°$. Figure 5.9 shows that O_2 can take near any φ though there is a maximum around 55° and minimum around 30° and 85°. We should note that the adsorption energy is not strongly influenced by angle φ when θ is fixed as indicated by Figure 5.3 thus we expect the angle φ distribution should be uniform. This is not the case here because the simulation time is short (8 pico-second) due to the limitation of computational resource. The distance between O atom of O_2 molecule nearest to the surface and its nearest Ti atom (O-Ti distances) will be from 2.6 Å to 5 Å as shown in Figure 5.10. The most probable O-Ti will be around 4 Å. From the MD simulation, we found the average O_2 bond length is about 1.235 Å, the average θ is 62.4°, the average O-Ti distance is about 3.913 Å. We can use these obtained average geometry parameters to construct representative structures of O_2 adsorbed on TiO_2(110) surfaces and perform the infrared calculations. The calculated infrared frequency (Table 5.2 #5) is about 1554.4 cm^{-1} that is still about 12 cm^{-1} lower than the pure gas result. The intensity is small but positive indicating IR active peak. As noted the O_2 bond length would have big impact on the calculation of infrared spectrum, we also use calculated gas phase O_2 bond length 1.233 Å to construct the representative structures of O_2 adsorbed on TiO_2(110) surfaces. The calculations show that the infrared frequency (Table 5.2 #6) is 1563.8 cm^{-1}. This is very close to the calculated gas phase frequencies of 1566 cm^{-1}, and the intensity is small but still indicating the peak is infrared active. Therefore, we can safely argue that after O_2 physically adsorbed on the TiO_2(110) surfaces, the infrared inactive peak will become active and appear at almost the same frequency as the Raman

spectrum. The reason that there is little shift in the vibrational frequency in experiments is that the O_2 molecule is very weakly bound to the surface, rotating almost freely, and hence, the bond length, should be very close to the gas phase value. In contrast, at low temperatures (DFT calculation is done at 0 K) that one should expect to observe a much larger shift in the infrared frequency, accompanied by a significantly larger intensity (one to two orders of magnitude) as a result of a substantial O_2 bond length change.

5.3.4 Origin of oxygen infrared active vibrational mode

The charge density difference shown in Figure 5.11 is calculated as

$$\Delta\rho = \rho_{O_2+TiO_2} - \rho_{O_2} - \rho_{TiO_2} \tag{5.7}$$

where $\rho_{O_2+TiO_2}$ denotes the charge density of weakly adsorbed O_2 on the TiO_2(110) system, ρ_{O_2} and ρ_{TiO_2} represents the unperturbed O_2 and TiO_2(110) surface respectively whose atomic positions are the same as those in weakly adsorbed system. The calculations for the unperturbed O_2 and TiO_2(110) surfaces were performed in the supercells with exactly the same dimensions and under identical conditions to those used for the adsorbed state to further elucidate the effect on charge density by the interaction between O_2 and TiO_2(110) surfaces in the weakly adsorbed state. we can clearly see that the O atom in O_2 near the Ti atom in top layer of surface is gaining electrons while the O atom in O_2 slightly far away from the Ti atom is losing electron, which will lead to a small net dipole moment along O=O axis. Therefore the infrared inactive vibrational mode becomes activated. There is only very slight electron transfer between the surface and O_2 molecule primarily through the nearest Ti atom as can be seen from Figure 5.11(a) which implies the charge transfer is happening mostly within O_2 molecule itself. The noticeable charge transfer

between lowest O atom of O_2 molecule and the surface is due to the interaction between O-2p band with Ti-3d band as can be visualized from the site projected density of states plot in Figure 5.12 which shows overlap of O-2p band with Ti-3d band around -1.9 eV and -6 eV. The charge unbalance could be induced by the electric field created by TiO_2(110) surface as shown in Figure 5.13. Here we also want to point out that before and after O_2 physically adsorption, the TiO_2(110) surface have very little change in terms of atomic positions, the only exception is the Ti atom just below the O_2 molecule whose atomic positions are slightly lower in *z* direction after O_2 adsorption on its top likely due to the interaction between O_2 and the Ti atom. The electric field is calculated by taking the negative gradient of the local electric potential of the TiO_2(110) surface whose atomic positions are taken from the weakly adsorbed O_2 on the TiO_2(110) system unmodified. Apparently, the two O atoms in O_2 molecule are sensing different magnitude of electric field created by the pure TiO_2(110) surface. This will result in charge transfer which is in agreement with different change density of O atom as observed from Figure 5.11. The measurable IR active vibrational mode may not be the only product of the charge inequilibrium inside O_2 molecule, but the reaction activity of O_2 molecule may also be consequently increased which is normally considered the activation of O_2 molecule.

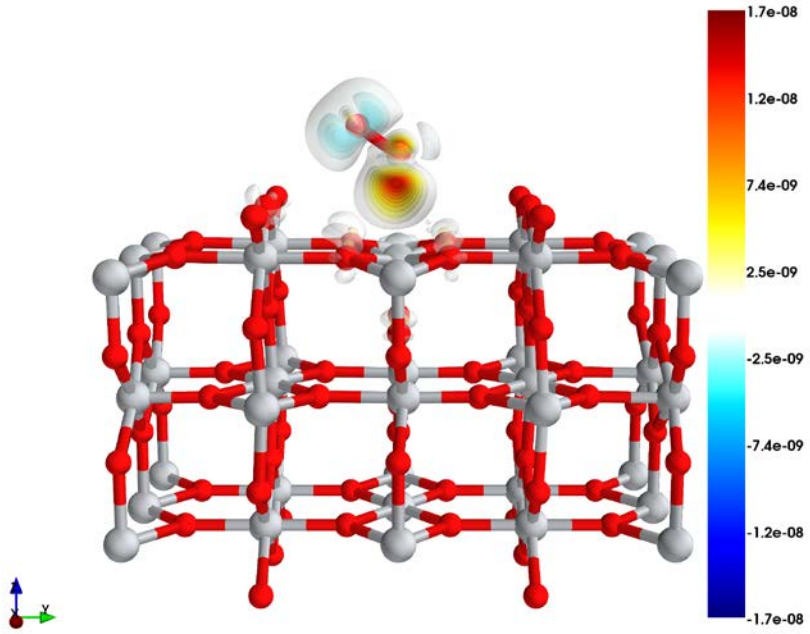

(a)

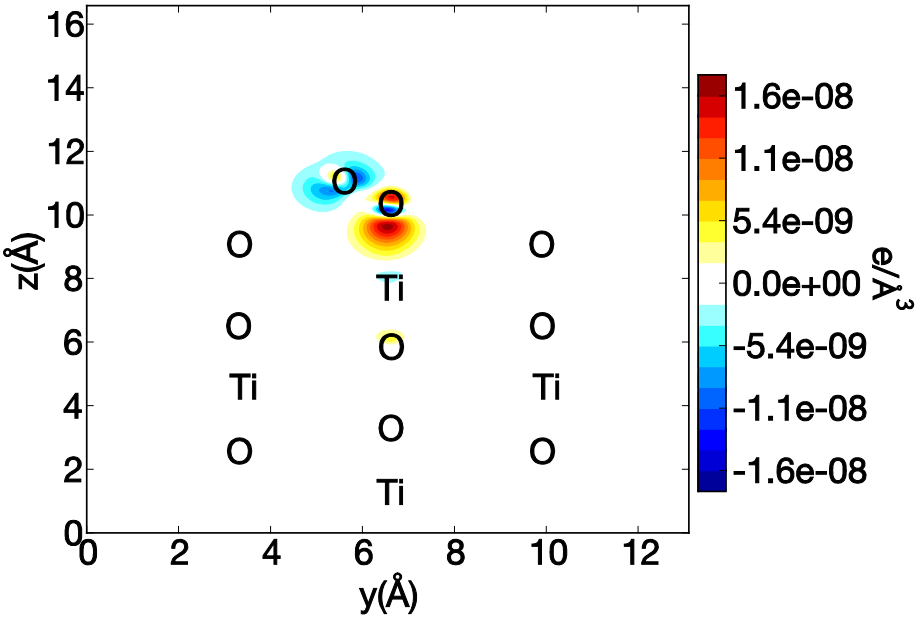

(b)

Figure 5.11. (a) Charge density difference of O_2 weakly bound on top of TiO_2(110) surface; (b) Charge density difference of the plane perpendicular to the (110) surface passing through the center of the adsorbed oxygen atoms. Weakly adsorbed O_2 molecule and TiO_2(110) surface atomic positions are labeled respectively.

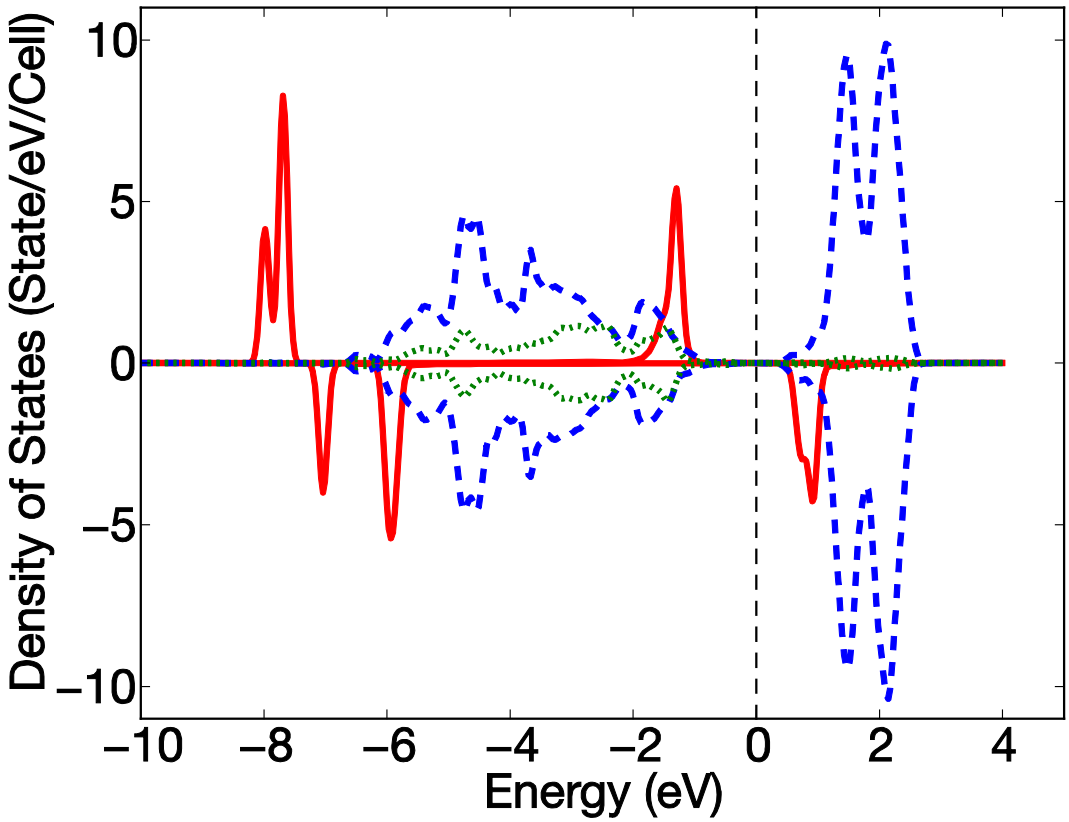

Figure 5.12. Site projected density of states of O_2 weakly bound on top of TiO_2(110) surface. Fermi level is set as 0 eV. Red solid line: weakly bound O_2 2p band; Green dotted line: top layer Ti 2p band; Blue dashed line: top layer Ti 3d band.

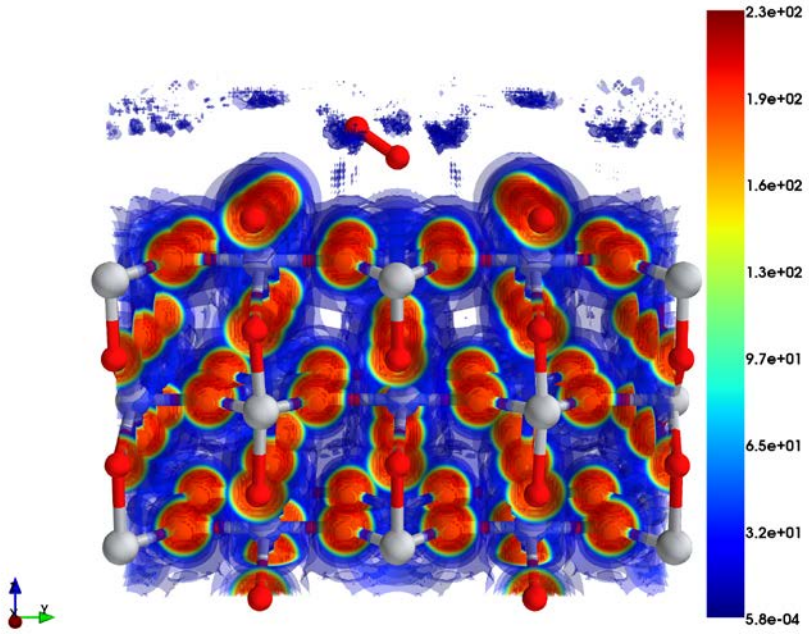

(a)

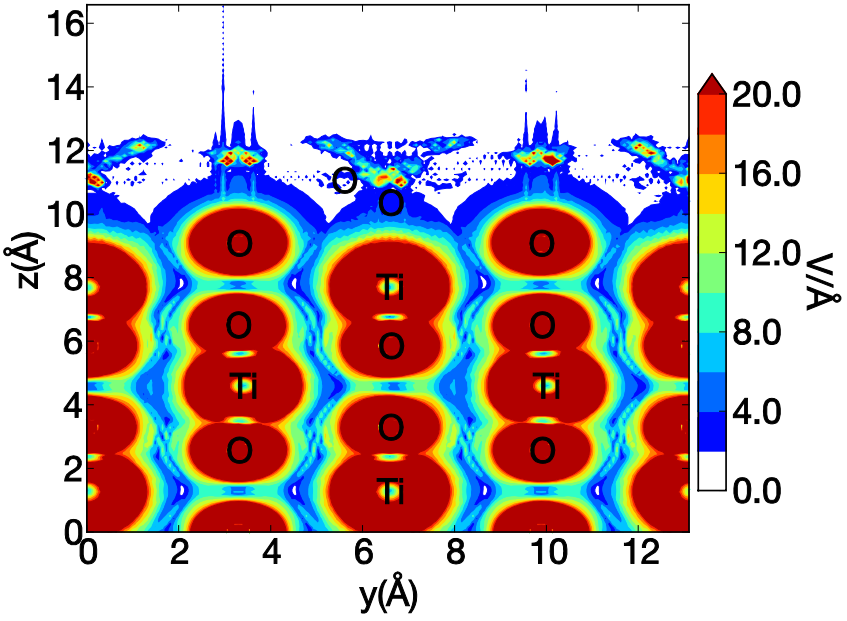

(b)

Figure 5.13. (a) Magnitude of electric field of O_2 weakly bound on top of TiO_2(110) surface; (b) Magnitude of electric field of the plane perpendicular to the (110) surface passing through the center of the adsorbed oxygen atoms. Weakly adsorbed O_2 molecule and TiO_2(110) surface atomic positions are labeled respectively.

5.4 CONCLUSION

In this chapter, we present a systematical study on weakly bound O_2 on top of TiO_2(110) surfaces. Our calculation show that the adsorption energy of O_2 on the TiO_2(110) surfaces is about -21.77 kJ/mol that is close to experimental measurements. Adding vdW correction to the standard DFT calculation is important in computing the adsorption energy. The adsorption of O_2 molecule on the TiO_2(110) surfaces should be considered physical in nature since the adsorption energy is small. The adsorption energy of O_2 on the TiO_2(110) surfaces is largely affected by θ, but nearly the same of any φ when θ is fixed. The adsorption energy of O_2 on the TiO_2(110) surfaces can also be correlated with the distance between lowest O atom and its nearest Ti atom and O_2 bond length when θ goes from roughly 45° to 90° or -45° to -90°. Although the relaxation of O_2 on the TiO_2(110) surfaces will result in different O_2 bond lengths which could possibly lead to different infrared frequencies, the calculated infrared intensity of the peak around 1550 cm^{-1} is non-zero which is in agreement with experiments. Using calculated gas phase O_2 bond length can lead to nearly the same infrared frequency as those calculated from gas phase O_2. We expect a substantial O_2 bond length change at much lower temperature will lead to much different infrared frequency and intensity to those measured at experimental conditions, especially the intensity will be one to two orders of magnitude larger. At last, the origin of infrared active O_2 vibrational mode is also investigated. We concluded that this is due to the charge transfer primarily within O_2 molecule itself which results in small dipole moment. The charge transfer is induced by the electric field created by the TiO_2(110) surface.

6.0 FUTURE WORK

As shown in Chapter 4, our developed ReaxFF force field does have some limitations. The calculated density from isothermal-isobaric (*NpT*) ensemble molecular dynamics (MD) simulation with current ReaxFF force field is higher than experimental measurements and the density calculated with classical force field. The CO_2 angle distributions from canonical (*NVT*) ensemble MD simulation at experimental density does not exactly match the DFT results as the product states found in simulation with ReaxFF force field are much less than those found in *ab initio* MD.

We will continue improve the current ReaxFF force field by fine tuning the parameters and weighting factors shown in Eq.(4.1) to match the available energies from DFT calculations. The goal is first to match the equation of state of $[P(C_4)_4][Gly]$ to reproduce the experimental density via *NpT* MD. Secondly we will continue to improve the description of reaction barrier for CO_2 reaction with $[P(C_4)_4][Gly]$ as well the N-C dissociation energy to tweak the CO_2 angle distribution for better representing the experiments or as least match the DFT MD results.

As discussed in 4.1, there are two different mechanisms of CO_2 reaction with $–NH_2$ functional group proposed by different experimental groups. One is that CO_2 interact with $–NH_2$ functional group to form a new $–CO_2H$ group whose proton is transfer from the original $–NH_2$ group as shown in Figure 4.5.[44] This reaction route is included in our current training set. The other mechanism that CO_2 can interact with two $–NH_2$ group to form carbamate and quaternary

ammonium species (see Figure 4.2)[42] or a CO_2H group whose proton is hydrogen bonded with other $–NH_2$ from another anion (see Figure 4.3)[43] is not covered by current training sets. We plan to also train our current ReaxFF force field based on the reaction pathway of second mechanism. Also we noted the carboxylic group in the anion $[Gly]^-$ may also contribute to the adsorption of CO_2 which seems not to be a strong chemical reaction. We shall continue to study this interaction by DFT methods and may also include this type interaction in the training sets.

Once the force field can reproduce most reaction pathways of $[P(C_4)_4][Gly]$ with CO_2, bond dissociation energy, angle distortion , torsion angle distortion energies as well as equation of state of $[P(C_4)_4][Gly]$, large-scale MD simulation will be carried out. The dynamical properties of pure $[P(C_4)_4][Gly]$ and $[P(C_4)_4][Gly]$ interacting with CO_2, such as radial distribution function, mean square displacements, diffusion coefficients, rotational time constants[181, 182] and viscosity will be calculated with force field and compared with other calculations by classical force field or experiments. The hydrogen bond network of reacted $[P(C_4)_4][Gly]$ with CO_2 will also be investigated to find if this leads to higher viscosity. The vibrational frequency of the pure $[P(C_4)_4][Gly]$ and reacted $[P(C_4)_4][Gly]$ with CO_2 can be calculated by Fourier transform of velocity autocorrelation function and will be compared with experiments. Reaction kinetics of $[P(C_4)_4][Gly]$ with CO_2 can also be studied with the force field and overall reaction rate constant can be estimated by fitting the Arrhenius plot. As for the potential of mean force or the free energy of the $[P(C_4)_4][Gly]$ interacting with CO_2 along the reaction coordinates can be computed by either thermodynamic integration method[10] via constrained MD or umbrella sampling[10] with weighted histogram analysis method via restrained MD. Finally, CO_2 solubility in $[P(C_4)_4][Gly]$ will be calculated with osmotic ensemble Monte Carlo methods which may require extending the capability of current codes.

In the future, water effect may also be studied since some group reports that if there is water present, even small amount, the reaction mechanism will be different (see Figure 4.4).[43] This requires extra sets of DFT data to be included in the training sets. A new ReaxFF force field will be generated to study such problems.

BIBLIOGRAPHY

1. IPCC, *IPCC Fourth Assessment Report (AR4)*. (2007).

2. J. D. Figueroa, T. Fout, S. Plasynski, H. McIlvried and R. D. Srivastava, International Journal of Greenhouse Gas Control **2** (1), 9-20 (2008).

3. N. Stern, *The Economics of Climate Change: The Stern Review*. (Cambridge University Press, 2007).

4. J. Hafner, Journal of Computational Chemistry **29** (13), 2044-2078 (2008).

5. M. J. Frisch, G. W. Trucks, H. B. Schlegel, G. E. Scuseria, M. A. Robb, J. R. Cheeseman, G. Scalmani, V. Barone, B. Mennucci, G. A. Petersson, H. Nakatsuji, M. Caricato, X. Li, H. P. Hratchian, A. F. Izmaylov, J. Bloino, G. Zheng, J. L. Sonnenberg, M. Hada, M. Ehara, K. Toyota, R. Fukuda, J. Hasegawa, M. Ishida, T. Nakajima, Y. Honda, O. Kitao, H. Nakai, T. Vreven, J. A. Montgomery, J. E. Peralta, F. Ogliaro, M. Bearpark, J. J. Heyd, E. Brothers, K. N. Kudin, V. N. Staroverov, R. Kobayashi, J. Normand, K. Raghavachari, A. Rendell, J. C. Burant, S. S. Iyengar, J. Tomasi, M. Cossi, N. Rega, J. M. Millam, M. Klene, J. E. Knox, J. B. Cross, V. Bakken, C. Adamo, J. Jaramillo, R. Gomperts, R. E. Stratmann, O. Yazyev, A. J. Austin, R. Cammi, C. Pomelli, J. W. Ochterski, R. L. Martin, K. Morokuma, V. G. Zakrzewski, G. A. Voth, P. Salvador, J. J. Dannenberg, S. Dapprich, A. D. Daniels, Farkas, J. B. Foresman, J. V. Ortiz, J. Cioslowski and D. J. Fox, *Gaussian 09, Revision B.01*. (Wallingford CT, 2009).

6. W. Kohn and L. J. Sham, Physical Review **140** (4A), A1133-A1138 (1965).

7. P. Geerlings, F. De Proft and W. Langenaeker, Chemical Reviews **103** (5), 1793-1874 (2003).

8. S. Kristyán and P. Pulay, Chemical Physics Letters **229** (3), 175-180 (1994).

9. M. Shishkin and G. Kresse, Physical Review B **75** (23), 235102 (2007).

10. D. Frenkel and B. Smit, *Understanding Molecular Simulation: From Algorithms to Applications*. (Elsevier Science, 2001).

11. W. D. Cornell, P. Cieplak, C. I. Bayly, I. R. Gould, K. M. Merz, D. M. Ferguson, D. C. Spellmeyer, T. Fox, J. W. Caldwell and P. A. Kollman, Journal of the American Chemical Society **117** (19), 5179-5197 (1995).

12. D. W. Brenner, Physical Review B **42** (15), 9458-9471 (1990).

13. D. W. Brenner, Physical Review B **46** (3), 1948-1948 (1992).

14. A. C. T. van Duin, S. Dasgupta, F. Lorant and W. A. Goddard, The Journal of Physical Chemistry A **105** (41), 9396-9409 (2001).

15. H. A. Mosqueda, C. Vazquez, P. Bosch and H. Pfeiffer, Chemistry of Materials **18** (9), 2307-2310 (2006).

16. R. V. Siriwardane, C. Robinson, M. Shen and T. Simonyi, Energy & Fuels **21** (4), 2088-2097 (2007).

17. Y. Liang, D. P. Harrison, R. P. Gupta, D. A. Green and W. J. McMichael, Energy & Fuels **18** (2), 569-575 (2004).

18. S. C. Lee, B. Y. Choi, T. J. Lee, C. K. Ryu, Y. S. Ahn and J. C. Kim, Catalysis Today **111** (3–4), 385-390 (2006).

19. S. C. Lee, H. J. Chae, S. J. Lee, B. Y. Choi, C. K. Yi, J. B. Lee, C. K. Ryu and J. C. Kim, Environmental Science & Technology **42** (8), 2736-2741 (2008).

20. S. C. Lee, H. J. Chae, S. J. Lee, Y. H. Park, C. K. Ryu, C. K. Yi and J. C. Kim, Journal of Molecular Catalysis B: Enzymatic **56** (2–3), 179-184 (2009).

21. Y. Duan and D. C. Sorescu, Physical Review B **79** (1), 014301 (2009).

22. A. R. Akbarzadeh, V. Ozoliņš and C. Wolverton, Advanced Materials **19** (20), 3233-3239 (2007).

23. S. V. Alapati, J. K. Johnson and D. S. Sholl, The Journal of Physical Chemistry C **112** (14), 5258-5262 (2008).

24. J. P. Perdew, A. Ruzsinszky, J. Tao, V. N. Staroverov, G. E. Scuseria and G. I. Csonka, The Journal of Chemical Physics **123** (6), 062201-062209 (2005).

25. D. C. Langreth and M. J. Mehl, Physical Review B **28** (4), 1809-1834 (1983).

26. D. C. Langreth and M. J. Mehl, Physical Review B **29** (4), 2310-2310 (1984).

27. A. D. Becke, Physical Review A **38** (6), 3098-3100 (1988).

28. J. P. Perdew, K. Burke and M. Ernzerhof, Physical Review Letters **77** (18), 3865-3868 (1996).

29. J. P. Perdew, K. Burke and M. Ernzerhof, Physical Review Letters **78** (7), 1396-1396 (1997).

30. J. P. Perdew, Physical Review Letters **55** (16), 1665-1668 (1985).

31. J. P. Perdew, Physical Review Letters **55** (21), 2370-2370 (1985).

32. A. D. Becke and M. R. Roussel, Physical Review A **39** (8), 3761-3767 (1989).

33. A. D. Becke, The Journal of Chemical Physics **98** (2), 1372-1377 (1993).

34. P. J. Stephens, F. J. Devlin, C. F. Chabalowski and M. J. Frisch, The Journal of Physical Chemistry **98** (45), 11623-11627 (1994).

35. P. Nozières and D. Pines, Physical Review **111** (2), 442-454 (1958).

36. P. A. Hunt, Molecular Simulation **32** (1), 1-10 (2006).

37. E. J. Maginn, Accounts of Chemical Research **40** (11), 1200-1207 (2007).

38. J. E. Bara, D. E. Camper, D. L. Gin and R. D. Noble, Accounts of Chemical Research **43** (1), 152-159 (2009).

39. M. Freemantle, T. Welton and R. D. Rogers, *An Introduction to Ionic Liquids*. (Royal Society of Chemistry, 2009).

40. L. A. Blanchard, Z. Gu and J. F. Brennecke, The Journal of Physical Chemistry B **105** (12), 2437-2444 (2001).

41. X. Huang, C. J. Margulis, Y. Li and B. J. Berne, Journal of the American Chemical Society **127** (50), 17842-17851 (2005).

42. E. D. Bates, R. D. Mayton, I. Ntai and J. H. Davis, Journal of the American Chemical Society **124** (6), 926-927 (2002).

43. J. Zhang, S. Zhang, K. Dong, Y. Zhang, Y. Shen and X. Lv, Chemistry – A European Journal **12** (15), 4021-4026 (2006).

44. B. E. Gurkan, J. C. de la Fuente, E. M. Mindrup, L. E. Ficke, B. F. Goodrich, E. A. Price, W. F. Schneider and J. F. Brennecke, Journal of the American Chemical Society **132** (7), 2116-2117 (2010).

45. J. Tang, H. Tang, W. Sun, H. Plancher, M. Radosz and Y. Shen, Chemical Communications (26), 3325-3327 (2005).

46. J. Tang, H. Tang, W. Sun, M. Radosz and Y. Shen, Journal of Polymer Science Part A: Polymer Chemistry **43** (22), 5477-5489 (2005).

47. J. Tang, Y. Shen, M. Radosz and W. Sun, Industrial & Engineering Chemistry Research **48** (20), 9113-9118 (2009).

48. W. Shi and D. C. Sorescu, The Journal of Physical Chemistry B **114** (46), 15029-15041 (2010).

49. K. Chenoweth, A. C. T. van Duin and W. A. Goddard, The Journal of Physical Chemistry A **112** (5), 1040-1053 (2008).

50. A. Fujishima and K. Honda, Nature **238** (5358), 37-38 (1972).

51. A. Fujishima, T. N. Rao and D. A. Tryk, Journal of Photochemistry and Photobiology C: Photochemistry Reviews **1** (1), 1-21 (2000).

52. M. Haruta, T. Kobayashi, H. Sano and N. Yamada, Chemistry Letters **16** (2), 405-408 (1987).

53. M. Haruta, S. Tsubota, T. Kobayashi, H. Kageyama, M. J. Genet and B. Delmon, Journal of Catalysis **144** (1), 175-192 (1993).

54. U. Diebold, Surface Science Reports **48** (5–8), 53-229 (2003).

55. G. Lu, A. Linsebigler and J. J. T. Yates, The Journal of Chemical Physics **102** (7), 3005-3008 (1995).

56. G. Lu, A. Linsebigler and J. J. T. Yates, The Journal of Chemical Physics **102** (11), 4657-4662 (1995).

57. A. Linsebigler, G. Lu and J. T. Yates, The Journal of Physical Chemistry **100** (16), 6631-6636 (1996).

58. L. M. Molina, M. D. Rasmussen and B. Hammer, The Journal of Chemical Physics **120** (16), 7673-7680 (2004).

59. M. D. Rasmussen, L. M. Molina and B. Hammer, The Journal of Chemical Physics **120** (2), 988-997 (2004).

60. X. Wu, M. C. Vargas, S. Nayak, V. Lotrich and G. Scoles, The Journal of Chemical Physics **115** (19), 8748-8757 (2001).

61. S. Grimme, Journal of Computational Chemistry **27** (15), 1787-1799 (2006).

62. S. Grimme, J. Antony, S. Ehrlich and H. Krieg, The Journal of Chemical Physics **132** (15), 154104-154119 (2010).

63. D. C. Langreth, M. Dion, H. Rydberg, E. Schröder, P. Hyldgaard and B. I. Lundqvist, International Journal of Quantum Chemistry **101** (5), 599-610 (2005).

64. O. A. von Lilienfeld, I. Tavernelli, U. Rothlisberger and D. Sebastiani, Physical Review Letters **93** (15), 153004 (2004).

65. B. Jeziorski, R. Moszynski and K. Szalewicz, Chemical Reviews **94** (7), 1887-1930 (1994).

66. A. Heßelmann and G. Jansen, Chemical Physics Letters **362** (3–4), 319-325 (2002).

67. I. X. Green and J. T. Yates, The Journal of Physical Chemistry C **114** (27), 11924-11930 (2010).

68. C. M. White, B. R. Strazisar, E. J. Granite, J. S. Hoffman and H. W. Pennline, Journal of the Air & Waste Management Association **53** (6), 645-715 (2003).

69. D. Aaron and C. Tsouris, Separation Science and Technology **40** (1-3), 321-348 (2005).

70. M. R. Allen, D. J. Frame, C. Huntingford, C. D. Jones, J. A. Lowe, M. Meinshausen and N. Meinshausen, Nature **458** (7242), 1163-1166 (2009).

71. H. Lund and B. V. Mathiesen, Energy **34** (5), 524-531 (2009).

72. E. Ochoa-Fernández, H. K. Rusten, H. A. Jakobsen, M. Rønning, A. Holmen and D. Chen, Catalysis Today **106** (1–4), 41-46 (2005).

73. H. Pfeiffer and P. Bosch, Chemistry of Materials **17** (7), 1704-1710 (2005).

74. R. S. Haszeldine, Science **325** (5948), 1647-1652 (2009).

75. J. C. Abanades, G. Grasa, M. Alonso, N. Rodriguez, E. J. Anthony and L. M. Romeo, Environmental Science & Technology **41** (15), 5523-5527 (2007).

76. S. C. Lee, B. Y. Choi, S. J. Lee, S. Y. Jung, C. K. Ryu and J. C. Kim, in *Studies in Surface Science and Catalysis*, edited by J.-S. C. Sang-Eon Park and L. Kyu-Wan (Elsevier, 2004), Vol. Volume 153, pp. 527-530.

77. V. Manovic and E. J. Anthony, Environmental Science & Technology **41** (4), 1420-1425 (2007).

78. M. Mercedes Maroto-Valer, Z. Lu, Y. Zhang and Z. Tang, Waste Management **28** (11), 2320-2328 (2008).

79. R. Siriwardane, J. Poston, K. Chaudhari, A. Zinn, T. Simonyi and C. Robinson, Energy & Fuels **21** (3), 1582-1591 (2007).

80. H. W. Pennline, D. R. Luebke, K. L. Jones, C. R. Myers, B. I. Morsi, Y. J. Heintz and J. B. Ilconich, Fuel Processing Technology **89** (9), 897-907 (2008).

81. V. Nikulshina, N. Ayesa, M. E. Gálvez and A. Steinfeld, Chemical Engineering Journal **140** (1–3), 62-70 (2008).

82. S. Lee and J. Kim, Catalysis Surveys from Asia **11** (4), 171-185 (2007).

83. Y. Duan and D. C. Sorescu, The Journal of Chemical Physics **133** (7), 074508-074511 (2010).

84. J. C. Abanades, E. J. Anthony, J. Wang and J. E. Oakey, Environmental Science & Technology **39** (8), 2861-2866 (2005).

85. H. Guoxin, H. Hao and L. Yanhong, International Journal of Hydrogen Energy **33** (20), 5422-5429 (2008).

86. B. Feng, H. An and E. Tan, Energy & Fuels **21** (2), 426-434 (2007).

87. M. B. Jensen, L. G. M. Pettersson, O. Swang and U. Olsbye, The Journal of Physical Chemistry B **109** (35), 16774-16781 (2005).

88. *Inorganic Crystal Structure Database*, http://www.fiz-karlsruhe.de/icsd.html.

89. E. H. Majzoub and V. Ozoliņš, Physical Review B **77** (10), 104115 (2008).

90. G. Kresse and J. Hafner, Physical Review B **47** (1), 558-561 (1993).

91. G. Kresse and J. Hafner, Physical Review B **49** (20), 14251-14269 (1994).

92. G. Kresse and J. Furthmüller, Physical Review B **54** (16), 11169-11186 (1996).

93. G. Kresse and J. Furthmüller, Computational Materials Science **6** (1), 15-50 (1996).

94. P. E. Blöchl, Physical Review B **50** (24), 17953-17979 (1994).

95. G. Kresse and D. Joubert, Physical Review B **59** (3), 1758-1775 (1999).

96. J. P. Perdew, J. A. Chevary, S. H. Vosko, K. A. Jackson, M. R. Pederson, D. J. Singh and C. Fiolhais, Physical Review B **46** (11), 6671-6687 (1992).

97. J. P. Perdew, J. A. Chevary, S. H. Vosko, K. A. Jackson, M. R. Pederson, D. J. Singh and C. Fiolhais, Physical Review B **48** (7), 4978-4978 (1993).

98. H. J. Monkhorst and J. D. Pack, Physical Review B **13** (12), 5188-5192 (1976).

99. K. Parlinski, Z. Q. Li and Y. Kawazoe, Physical Review Letters **78** (21), 4063-4066 (1997).

100. M. W. J. Chase, *NIST-JANAF Thermochemical Tables*. (American Inst. of Physics, 1998).

101. F. Birch, Physical Review **71** (11), 809-824 (1947).

102. F. D. Murnaghan, American Journal of Mathematics **59** (2), 235-260 (1937).

103. B. Sharma, Acta Crystallographica **18** (4), 818-819 (1965).

104. J. O. Thomas, R. Tellgren and I. Olovsson, Acta Crystallographica Section B **30** (5), 1155-1166 (1974).

105. M. Machida, Y. Iwata, N. Koyano, S. Fukui and I. Shibuya, Kyoto Daigaku Genshiro Jikkensko Gakujutsu Koenkai Hobunshu **28**, 253-258 (1994).

106. D. R. Allan, W. G. Marshall and C. R. Pulham, American Mineralogist **92** (7), 1018-1025.

107. D. R. Lide, *CRC Handbook of Chemistry and Physics*, 84th ed. (CRC Press, Boca Raton, FL, 2003).

108. *HSC Chemistry software*, 6.1 ed. (Outotec Research, 2006).

109. P. Dhawan, *Inorganic Chemistry*. (McGraw-Hill Education (India) Pvt Limited, 2007).

110. J. S. Hoffman and H. W. Pennline, presented at the International Pittsburgh Coal Conference, Pittsburgh, 2000 (unpublished).

111. H. Jacobs, J. Kockelkorn and T. Tacke, Zeitschrift für anorganische und allgemeine Chemie **531** (12), 119-124 (1985).

112. S. W. Park, D. H. Sung, B. S. Choi, J. W. Lee and H. Kumazawa, J. Ind. Eng. Chem. **12** (4), 522-530 (2006).

113. S. W. Park, D. H. Sung, B. S. Choi, K. J. Oh and K. H. Moon, Separation Science and Technology **41** (12), 2665-2684 (2006).

114. G. Astarita, G. Marrucci and F. Gioia, Chemical Engineering Science **19** (2), 95-103 (1964).

115. T. Supap, R. Idem, P. Tontiwachwuthikul and C. Saiwan, International Journal of Greenhouse Gas Control **3** (2), 133-142 (2009).

116. S. Chi and G. T. Rochelle, Industrial & Engineering Chemistry Research **41** (17), 4178-4186 (2002).

117. M. R. M. Abu-Zahra, J. P. M. Niederer, P. H. M. Feron and G. F. Versteeg, International Journal of Greenhouse Gas Control **1** (2), 135-142 (2007).

118. E. Diaz, E. Munoz, A. Vega and S. Ordonez, Industrial & Engineering Chemistry Research **47** (2), 412-418 (2007).

119. C. Pevida, M. G. Plaza, B. Arias, J. Fermoso, F. Rubiera and J. J. Pis, Applied Surface Science **254** (22), 7165-7172 (2008).

120. J. Liu, S. Keskin, D. S. Sholl and J. K. Johnson, The Journal of Physical Chemistry C **115** (25), 12560-12566 (2011).

121. R. Banerjee, A. Phan, B. Wang, C. Knobler, H. Furukawa, M. O'Keeffe and O. M. Yaghi, Science **319** (5865), 939-943 (2008).

122. R. Banerjee, H. Furukawa, D. Britt, C. Knobler, M. O'Keeffe and O. M. Yaghi, Journal of the American Chemical Society **131** (11), 3875-3877 (2009).

123. F. Brandani and D. M. Ruthven, Industrial & Engineering Chemistry Research **43** (26), 8339-8344 (2004).

124. Y. Wang, Y. Zhou, C. Liu and L. Zhou, Colloids and Surfaces A: Physicochemical and Engineering Aspects **322** (1–3), 14-18 (2008).

125. E. J. Doskocil, S. V. Bordawekar and R. J. Davis, Journal of Catalysis **169** (1), 327-337 (1997).

126. J. Tai, Q. Ge, R. J. Davis and M. Neurock, The Journal of Physical Chemistry B **108** (43), 16798-16805 (2004).

127. N. H. Florin and A. T. Harris, Energy & Fuels **22** (4), 2734-2742 (2008).

128. K. Mudiyanselage, C.-W. Yi and J. n. Szanyi, Langmuir **25** (18), 10820-10828 (2009).

129. M. Tutuianu, O. R. Inderwildi, W. G. Bessler and J. Warnatz, The Journal of Physical Chemistry B **110** (35), 17484-17492 (2006).

130. M. Pohl and A. Otto, Surface Science **406** (1–3), 125-137 (1998).

131. M. Casarin, D. Falcomer, A. Glisenti and A. Vittadini, Inorganic Chemistry **42** (2), 436-445 (2002).

132. M. Casarin, D. Falcomer and A. Vittadini, Surface Science **566–568, Part 2** (0), 890-894 (2004).

133. J. Baltrusaitis, J. H. Jensen and V. H. Grassian, The Journal of Physical Chemistry B **110** (24), 12005-12016 (2006).

134. S. Funk, T. Nurkic, B. Hokkanen and U. Burghaus, Applied Surface Science **253** (17), 7108-7114 (2007).

135. O. Seiferth, K. Wolter, B. Dillmann, G. Klivenyi, H. J. Freund, D. Scarano and A. Zecchina, Surface Science **421** (1–2), 176-190 (1999).

136. J. K. Stolaroff, D. W. Keith and G. V. Lowry, Environmental Science & Technology **42** (8), 2728-2735 (2008).

137. E. Ochoa-Fernández, M. Rønning, T. Grande and D. Chen, Chemistry of Materials **18** (6), 1383-1385 (2006).

138. E. Ochoa-Fernández, M. Rønning, T. Grande and D. Chen, Chemistry of Materials **18** (25), 6037-6046 (2006).

139. Y. Duan, Journal of Renewable and Sustainable Energy **3** (1), 013102-013117 (2011).

140. T. Zhao, E. Ochoa-Fernández, M. Rønning and D. Chen, Chemistry of Materials **19** (13), 3294-3301 (2007).

141. R. V. Siriwardane and R. W. Stevens, Industrial & Engineering Chemistry Research **48** (4), 2135-2141 (2008).

142. C. Zhao, X. Chen and C. Zhao, Energy & Fuels **23** (9), 4683-4687 (2009).

143. Z. Yong and A. r. E. Rodrigues, Energy Conversion and Management **43** (14), 1865-1876 (2002).

144. M. K. Ram Reddy, Z. P. Xu, G. Q. Lu and J. C. Diniz da Costa, Industrial & Engineering Chemistry Research **45** (22), 7504-7509 (2006).

145. P. Cho, T. Mattisson and A. Lyngfelt, Fuel **83** (9), 1215-1225 (2004).

146. R. Siriwardane, H. Tian, G. Richards, T. Simonyi and J. Poston, Energy & Fuels **23** (8), 3885-3892 (2009).

147. B. P. Burton, N. Dupin, S. G. Fries, G. Grimvall, A. F. Guillermet, P. Miodownik, W. A. Oates and V. Vinograd, Z. Metallk. **92** (6), 514-525 (2001).

148. C. Wolverton, X. Y. Yan, R. Vijayaraghavan and V. Ozoliņš, Acta Materialia **50** (9), 2187-2197 (2002).

149. S. V. Alapati, J. K. Johnson and D. S. Sholl, The Journal of Physical Chemistry C **111** (4), 1584-1591 (2007).

150. Y. Duan, B. Zhang, D. C. Sorescu and J. K. Johnson, Journal of Solid State Chemistry **184** (2), 304-311 (2011).

151. J. P. Perdew, A. Ruzsinszky, G. I. Csonka, O. A. Vydrov, G. E. Scuseria, L. A. Constantin, X. Zhou and K. Burke, Physical Review Letters **100** (13), 136406 (2008).

152. J. P. Perdew, A. Ruzsinszky, G. I. Csonka, O. A. Vydrov, G. E. Scuseria, L. A. Constantin, X. Zhou and K. Burke, Physical Review Letters **102** (3), 039902 (2009).

153. J. Enkovaara, C. Rostgaard, J. J. Mortensen, J. Chen, M. Dułak, L. Ferrighi, J. Gavnholt, C. Glinsvad, V. Haikola, H. A. Hansen, H. H. Kristoffersen, M. Kuisma, A. H. Larsen, L. Lehtovaara, M. Ljungberg, O. Lopez-Acevedo, P. G. Moses, J. Ojanen, T. Olsen, V. Petzold, N. A. Romero, J. Stausholm-Møller, M. Strange, G. A. Tritsaris, M. Vanin, M.

Walter, B. Hammer, H. Häkkinen, G. K. H. Madsen, R. M. Nieminen, J. K. Nørskov, M. Puska, T. T. Rantala, J. Schiøtz, K. S. Thygesen and K. W. Jacobsen, Journal of Physics: Condensed Matter **22** (25), 253202 (2010).

154. J. Tao, J. P. Perdew, V. N. Staroverov and G. E. Scuseria, Physical Review Letters **91** (14), 146401 (2003).

155. J. P. Perdew, A. Ruzsinszky, G. I. Csonka, L. A. Constantin and J. Sun, Physical Review Letters **103** (2), 026403 (2009).

156. G. J. Ackland, Journal of Physics: Condensed Matter **14** (11), 2975 (2002).

157. J. A. Dean, *Lange's Handbook of Chemistry*, 15th ed. (McGraw-Hill, New York, 1998).

158. D. G. Archer, Journal of Physical and Chemical Reference Data **28** (5), 1485-1507 (1999).

159. A. D. Becke, The Journal of Chemical Physics **98** (7), 5648-5652 (1993).

160. J. Paier, M. Marsman and G. Kresse, The Journal of Chemical Physics **127** (2), 024103-024110 (2007).

161. M. Ernzerhof and G. E. Scuseria, The Journal of Chemical Physics **110** (11), 5029-5036 (1999).

162. C. Adamo and V. Barone, The Journal of Chemical Physics **110** (13), 6158-6170 (1999).

163. J. Heyd, G. E. Scuseria and M. Ernzerhof, The Journal of Chemical Physics **118** (18), 8207-8215 (2003).

164. J. Paier, M. Marsman, K. Hummer, G. Kresse, I. C. Gerber and J. G. Angyan, The Journal of Chemical Physics **124** (15), 154709-154713 (2006).

165. M. Marsman, J. Paier, A. Stroppa and G. Kresse, Journal of Physics: Condensed Matter **20** (6), 064201 (2008).

166. K. Doll, M. Dolg, P. Fulde and H. Stoll, Physical Review B **55** (16), 10282-10288 (1997).

167. F. R. Manby, D. Alfe and M. J. Gillan, Physical Chemistry Chemical Physics **8** (44), 5178-5180 (2006).

168. S. Casassa, M. Halo, L. Maschio, C. Roetti and C. Pisani, Theoretical Chemistry Accounts: Theory, Computation, and Modeling (Theoretica Chimica Acta) **117** (5), 781-791 (2007).

169. M. Marsman, A. Gruneis, J. Paier and G. Kresse, The Journal of Chemical Physics **130** (18), 184103-184110 (2009).

170. J. Heyd and G. E. Scuseria, The Journal of Chemical Physics **121** (3), 1187-1192 (2004).

171. V. I. Anisimov, J. Zaanen and O. K. Andersen, Physical Review B **44** (3), 943-954 (1991).

172. V. I. Anisimov, F. Aryasetiawan and A. I. Lichtenstein, Journal of Physics: Condensed Matter **9** (4), 767 (1997).

173. J. L. F. Da Silva, M. V. Ganduglia-Pirovano, J. Sauer, V. Bayer and G. Kresse, Physical Review B **75** (4), 045121 (2007).

174. A. Jain, G. Hautier, S. P. Ong, C. J. Moore, C. C. Fischer, K. A. Persson and G. Ceder, Physical Review B **84** (4), 045115 (2011).

175. S. Lutfalla, V. Shapovalov and A. T. Bell, Journal of Chemical Theory and Computation **7** (7), 2218-2223 (2011).

176. B. Zhang, Y. Duan and K. Johnson, The Journal of Chemical Physics **136** (6), 064516-064513 (2012).

177. H.-B. Xie, J. K. Johnson, R. J. Perry, S. Genovese and B. R. Wood, The Journal of Physical Chemistry A **115** (3), 342-350 (2010).

178. H.-B. Xie, Y. Zhou, Y. Zhang and J. K. Johnson, The Journal of Physical Chemistry A **114** (43), 11844-11852 (2010).

179. C. Cadena, J. L. Anthony, J. K. Shah, T. I. Morrow, J. F. Brennecke and E. J. Maginn, Journal of the American Chemical Society **126** (16), 5300-5308 (2004).

180. A. Yokozeki, M. B. Shiflett, C. P. Junk, L. M. Grieco and T. Foo, The Journal of Physical Chemistry B **112** (51), 16654-16663 (2008).

181. K. E. Gutowski and E. J. Maginn, Journal of the American Chemical Society **130** (44), 14690-14704 (2008).

182. H. Wu, J. K. Shah, C. M. Tenney, T. W. Rosch and E. J. Maginn, Industrial & Engineering Chemistry Research **50** (15), 8983-8993 (2011).

183. M. R. LaBrosse, J. K. Johnson and A. C. T. van Duin, The Journal of Physical Chemistry A **114** (18), 5855-5861 (2010).

184. O. Rahaman, A. C. T. van Duin, W. A. Goddard and D. J. Doren, The Journal of Physical Chemistry B **115** (2), 249-261 (2010).

185. M. B. Shiflett, D. J. Kasprzak, C. P. Junk and A. Yokozeki, The Journal of Chemical Thermodynamics **40** (1), 25-31 (2008).

186. M. B. Shiflett and A. Yokozeki, Journal of Chemical & Engineering Data **54** (1), 108-114 (2008).

187. P. J. Carvalho, V. c. H. Álvarez, B. Schröder, A. M. Gil, I. M. Marrucho, M. n. Aznar, L. s. M. N. B. F. Santos and J. o. A. P. Coutinho, The Journal of Physical Chemistry B **113** (19), 6803-6812 (2009).

188. W. Shi, C. R. Myers, D. R. Luebke, J. A. Steckel and D. C. Sorescu, The Journal of Physical Chemistry B **116** (1), 283-295 (2011).

189. L. M. Galán Sánchez, G. W. Meindersma and A. B. de Haan, Chemical Engineering Research and Design **85** (1), 31-39 (2007).

190. M. D. Soutullo, C. I. Odom, B. F. Wicker, C. N. Henderson, A. C. Stenson and J. H. Davis, Chemistry of Materials **19** (15), 3581-3583 (2007).

191. G. Yu, S. Zhang, G. Zhou, X. Liu and X. Chen, AIChE Journal **53** (12), 3210-3221 (2007).

192. G. Zhou, X. Liu, S. Zhang, G. Yu and H. He, The Journal of Physical Chemistry B **111** (25), 7078-7084 (2007).

193. M. H. Kowsari, S. Alavi, B. Najafi, K. Gholizadeh, E. Dehghanpisheh and F. Ranjbar, Physical Chemistry Chemical Physics **13** (19), 8826-8837 (2011).

194. W. J. Mortier, S. K. Ghosh and S. Shankar, Journal of the American Chemical Society **108** (15), 4315-4320 (1986).

195. A. K. Rappe and W. A. Goddard, The Journal of Physical Chemistry **95** (8), 3358-3363 (1991).

196. A. C. T. van Duin, J. M. A. Baas and B. van de Graaf, Journal of the Chemical Society, Faraday Transactions **90** (19), 2881-2895 (1994).

197. G. Mills and H. Jónsson, Physical Review Letters **72** (7), 1124-1127 (1994).

198. G. Mills, H. Jónsson and G. K. Schenter, Surface Science **324** (2–3), 305-337 (1995).

199. H. Jónsson, G. Mills and K. W. Jacobsen, in *Classical and Quantum Dynamics in Condensed Phase Simulations*, edited by B. J. Berne, G. Ciccotti and D. F. Coker (World Scientific, Singapore, 1998), pp. 385-404.

200. G. Henkelman and H. Jonsson, The Journal of Chemical Physics **113** (22), 9978-9985 (2000).

201. G. Henkelman, B. P. Uberuaga and H. Jonsson, The Journal of Chemical Physics **113** (22), 9901-9904 (2000).

202. S. Plimpton, Journal of Computational Physics **117** (1), 1-19 (1995).

203. J. Papp, H. S. Shen, R. Kershaw, K. Dwight and A. Wold, Chemistry of Materials **5** (3), 284-288 (1993).

204. C. M. Wang, A. Heller and H. Gerischer, Journal of the American Chemical Society **114** (13), 5230-5234 (1992).

205. O. Bikondoa, C. L. Pang, R. Ithnin, C. A. Muryn, H. Onishi and G. Thornton, Nat Mater **5** (3), 189-192 (2006).

206. S. Wendt, R. Schaub, J. Matthiesen, E. K. Vestergaard, E. Wahlström, M. D. Rasmussen, P. Thostrup, L. M. Molina, E. Lægsgaard, I. Stensgaard, B. Hammer and F. Besenbacher, Surface Science **598** (1–3), 226-245 (2005).

207. X. Wu, A. Selloni, M. Lazzeri and S. K. Nayak, Physical Review B **68** (24), 241402 (2003).

208. L. M. Liu, B. McAllister, H. Q. Ye and P. Hu, Journal of the American Chemical Society **128** (12), 4017-4022 (2006).

209. M. A. Henderson, W. S. Epling, C. L. Perkins, C. H. F. Peden and U. Diebold, The Journal of Physical Chemistry B **103** (25), 5328-5337 (1999).

210. R. Schaub, E. Wahlström, A. Rønnau, E. Lægsgaard, I. Stensgaard and F. Besenbacher, Science **299** (5605), 377-379 (2003).

211. Z. Dohnálek, J. Kim, O. Bondarchuk, J. M. White and B. D. Kay, The Journal of Physical Chemistry B **110** (12), 6229-6235 (2006).

212. X. Cui, B. Wang, Z. Wang, T. Huang, Y. Zhao, J. Yang and J. G. Hou, The Journal of Chemical Physics **129** (4), 044703-044708 (2008).

213. P. W. Tasker, Journal of Physics C: Solid State Physics **12** (22), 4977 (1979).

214. R. D. King-Smith and D. Vanderbilt, Physical Review B **47** (3), 1651-1654 (1993).

215. D. Vanderbilt and R. D. King-Smith, Physical Review B **48** (7), 4442-4455 (1993).

216. R. Resta, Reviews of Modern Physics **66** (3), 899-915 (1994).

217. D. Porezag and M. R. Pederson, Physical Review B **54** (11), 7830-7836 (1996).

218. A. Eichler and J. Hafner, Physical Review Letters **79** (22), 4481-4484 (1997).

219. G. Herzberg and J. W. T. Spinks, *Molecular Spectra and Molecular Structure: Diatomic molecules*. (Van Nostrand, 1950).